AD NUMBER

AD836951

NEW LIMITATION CHANGE

TO

Approved for public release, distribution unlimited

FROM

Distribution authorized to U.S. Gov't. agencies and their contractors; Critical Technology; JUL 1968. Other requests shall be referred to Air Force Weapons Lab., Attn: WLDC, Kirtland AFB, NM 87117.

AUTHORITY

Air Force Weapons Labs ltr dtd 30 Nov 1971
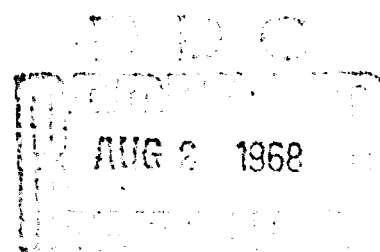
AD836951

FEASIBILITY STUDY OF CONTROL MECHANISM

AND COOLANT PROPERTIES OF A TERRESTRIAL

UNATTENDED REACTOR POWER SYSTEM

R. Magladry   G. F. Zindler

Martin Marietta Corporation

Nuclear Division

Middle River, Maryland 21220

Contract AF 29(601)-7180

AUG 2 1968

TECHNICAL REPORT NO. AFWL-TR-67-114, Vol I

July 1968

AIR FORCE WEAPONS LABORATORY

Air Force Systems Command

Kirtland Air Force Base

New Mexico

WHITE SECTION ☐
BUFF SECTION ☑
...NOUNCED ☐
...I...ATION ....

....

? PUTION/AVAILABILITY CODES

AVAIL. and/or SPECIAL

AIR FORCE WEAPONS LABORATORY
Air Force Systems Command
Kirtland Air Force Base
New Mexico

When U. S. Government drawings, specifications, or other data are used for
any purpose other than a definitely related Government procurement operation,
the Government thereby incurs no responsibility nor any obligation whatsoever,
and the fact that the Government may have formulated, furnished, or in any
way supplied the said drawings, specifications, or other data, is not to be
regarded by implication or otherwise, as in any manner licensing the holder
or any other person or corporation, or conveying any rights or permission to
manufacture, use, or sell any patented invention that may in any way be
related thereto.

This report is made available for study with the understanding that
proprietary interests in and relating thereto will not be impaired. In
case of apparent conflict or any other questions between the Government's
rights and those of others, notify the Judge Advocate, Air Force Systems
Command, Andrews Air Force Base, Washington, D. C. 20331.

DO NOT RETURN THIS COPY. RETAIN OR DESTROY.

FEASIBILITY STUDY OF CONTROL MECHANISM AND COOLANT

PROPERTIES OF A TERRESTRIAL UNATTENDED REACTOR POWER SYSTEM

R. Magladry   G. F. Zindler

Martin Marietta Corporation
Nuclear Division
Middle River, Maryland 21220
Contract AF 29(601)-7180

TECHNICAL REPORT NO. AFWL-TR-67-114, Vol I

FOREWORD

This report was prepared by the Nuclear Division of the Martin Marietta
Corporation, Middle River, Maryland, under Contract AF 29(601)-7180. The
research was performed under Program Element 6.24.05.21.F, Project 2800,
Task 02, recently changed to Project 3145, Task 024.

Inclusive dates of research were 9 March 1966 through 30 September 1967.
The report was submitted 14 June 1968 by the Air Force Weapons Laboratory
Project Officer, Captain Kenneth R. Hooks (WLDC).

This report is presented in two volumes. Volume I reports on the unclassi-
fied areas of the study while Volume II covers the classified areas.

The efforts of R. Lightner, F. Russo, J. Gray, J. Monroe, N. Strazza, and
J. Fitzgerald of Martin Marietta Nuclear Division are acknowledged.

This technical report has been reviewed and is approved.

KENNETH R. HOOKS
Captain, USAF
Project Officer

ROBERT E. CRAWFORD
Lt Colonel, USAF
Chief, Civil Engineering Branch

GEORGE C. DARBY, JR.
Colonel, USAF
Chief, Development Division

ABSTRACT

A detailed program of analytical and experimental investigation into the technical feasibility of the H-Rho nuclear reactor control system and tetra-phosphorous trisulfide (P_4S_3) as a reactor coolant are presented in this study.

The H-Rho control system investigation includes determinations of hydrogen transport (permeability) through porous bodies of zirconium hydride and uranium zirconium hydride as well as the absorption-desorption of hydrogen within the hydride bodies. The effects of temperature, pressure, particle size, inert gas and irradiation are evaluated.

The investigation of the coolant includes determinations of viscosity, surface tension, thermal conductivity, vapor pressure, liquid density and heat of fusion. The effects of irradiation on the P_4S_3 are evaluated.

The results of the investigation demonstrate that both the H-Rho control system and the P_4S_3 coolant are particularly suited for application to the Terrestrial Unattended Reactor Power System (TURPS).

(Distribution Limitation Statement No. 2)

This page intentionally left blank.

CONTENTS

ILLUSTRATIONS

ILLUSTRATIONS (cont'd)

ILLUSTRATIONS (cont'd)

ILLUSTRATIONS (cont'd)

TABLES

TABLES (cont'd)

This page intentionally left blank.

SECTION I

GENERAL INTRODUCTION

The results of an investigation into the technical feasibility of the control
mechanism (H-Rho) and into the properties of the coolant (Theon) selected
for the Terrestrial Unattended Reactor Power System (TURPS) are presented
in this report. Portions of the investigations reported herein were performed at
the Nuclear Engineering Test Facility at Wright-Patterson Air Force Base, Ohio
and at the Battelle Memorial Institute, Columbus, Ohio.

Under the TURPS program there have been two previous studies as reported
in the following documents:

> AFWL-TR-64-168, "Terrestrial Direct Conversion Nuclear Power Plant
> Conceptual Design." March 1965
>
> AFWL-TR-66-16, "Feasibility Study of Terrestrial Thermoelectric
> Nuclear Power Plant." June 1966

Under the first study, TURPS was designed to performance specifications
developed by the Air Force Weapons Laboratory. Under the second study two
major constituents of TURPS, H-Rho control and Theon coolant, were investi-
gated through out-of-core experiment and consequent analysis. The current
study initiated in-core experimental investigation and continued the out-of
core work with both H-Rho and Theon.

The H-Rho tasks include the performance and analysis of a number of tests
designed to investigate the hydrogen mass transport characteristics of porous
zirconium and uranium-zirconium hydride bodies. A neutron irradiation pro-
gram was performed using similar uranium-zirconium bodies to determine
fission product retention. Also performed was a series of thermal diffusivity
and specific heat measurements on similar bodies. From these data the thermal
conductivities of the bodies were determined.

In parallel with the experimental efforts, a major revision was made in the
computer program for the analysis of H-Rho experimental data. The new pro-
gram, HYDRA II, retains the basic mathematical model in which the body is di-
vided into a number of discrete zones normal to the direction of hydrogen trans-
port. In HYDRA I, the analytic procedure was one of stepping sequentially from
zone to zone through the body. HYDRA II solves the equations for all zones simul-
taneously.

Under the Theon tasks a number of measurements were made to determine physical properties such as viscosity, surface tension, vapor pressure and thermal conductivity. A 300-hour, high temperature irradiation of the coolant has been completed. An experimental program to determine the compatibility of Theon with various metals and metal surface preparations was completed. A dynamic corrosion loop has been constructed for performance of a 4500-hour, high temperature study of the Zircaloy-Theon system.

The following sections of this report present the technical approach and results of these investigations. These are divided into the following topics:

Section II   Hydrogen Transport in a Zirconium Hydride Matrix

Section III   Thermal Conductivity of Porous Zirconium Hydride

Section IV   Physical Properties of Theon (P_4S_3)

Section V   Irradiation of Theon (P_4S_3)

Section VI   Chemical Compatibility of Theon with Metals

For reasons of National Security, Volume II presents the results of the irradiation of zirconium and uranium-zirconium hydride.

SECTION II

HYDROGEN TRANSPORT IN A ZIRCONIUM HYDRIDE MATRIX

1. Purpose

This task experimentally determined the hydrogen response character-
istics of the proposed TURPS fuel form. As presently designed, the TURPS
core and hydrogen reservoir regions will consist of porous bodies of uranium
zirconium hydride and zirconium hydride, respectively. Typically, the
bodies are fabricated from mesh-size particles using powder metallurgy tech-
niques. During the present work, a number of sample bodies were fabricated
from spherical zirconium, nonspherical zirconium, and spherical zirconium-10
percent uranium particles. Selected bodies were subjected to the following sets
of tests:

    (1) Permeability measurements.

    (2) Hydrogen absorption transients.

    (3) Thermal-hydrogen cycling.

In the performance of this task, several major activities were required:

    (1) Modify the existing HYDRA code to increase its analytical capability
and improve its operating characteristics for use as a data analysis tool.

    (2) Plan a test program to study the dynamic hydrogen transport process.

    (3) Design, build, and check out an apparatus for investigating the hydrogen
absorption characteristics of porous zirconium hydride and uranium-zirconium
hydride bodies. Prepare the supporting test procedures.

    (4) Perform the various experiments; reduce and analyze the data.

2. HYDRA II Digital Code

HYDRA II is a digital computer code written to simulate the dynamic process
of hydrogen transport from the gas phase into a hydride bed. The basic mathe-
matical formulation is the same as that of the earlier computer code HYDRA I
with the inclusion of the continuity equation to describe the presence of an inert
gas. Further modifications included the use of the Klinkenberg equation in cal-
culating the permeability and the flexibility of the code to divide the bed into as
many as 10 zones. The nomenclature used in the development of the hydrogen
transport analysis and subsequent experimental program is presented in table I.

Table I

NOTATIONS (USED IN HYDROGEN TRANSPORT SECTION)

a	Effective radius of particle
$\bar{c}$	Average hydrogen concentration
c_s	Solid heat capacity
D	Diffusion coefficient
d	Permeability
ΔH	Heat of reaction
K	$n^2 \pi^2 / a^2$
L	Volumetric heat loss rate
P	Total gas pressure
P_H	Hydrogen gas pressure
P_I	Inert gas pressure
S	Volumetric heat generation or absorption rate
T	$\displaystyle\int_0^t D\,dt$
t	Time
V	Superficial gas velocity
x	Length
α_i	Constant used in equilibrium equation
β_i	Constant used in equilibrium equation
ϵ	Void fraction
θ	Temperature
μ	Gas viscosity
ρ_H	Hydrogen density
ρ_I	Inert gas density
ρ_S	Solid density
ψ	Surface concentration
λ	Dummy variable

a. Mathematical Treatment and Solution

The basic mathematical solution is obtained by simultaneously solving the following set of equations.

$$\frac{d\bar{c}}{dt} = \frac{6D(t)}{a^2} \sum_{n=1}^{\infty} \left\{ \psi(T_n) - Ke^{-KT_n} \int_0^{T_n} \psi(\lambda) e^{K\lambda}\,d\lambda \right\} \tag{1}$$

$$\log P_H = \sum_{i=1}^{4} (\alpha_i + \beta_i/\theta)\psi^{i-1} \tag{2}$$

$$\epsilon \frac{\partial \rho_H}{\partial t} + (1 - \epsilon) \frac{d\bar{c}}{dt} + \frac{\partial(\rho_H V)}{\partial x} = 0 \tag{3}$$

$$\epsilon \frac{\partial \rho_I}{\partial t} + \frac{\partial(\rho_I V)}{\partial x} = 0 \tag{4}$$

$$V = -\frac{d}{\mu} \frac{\partial P}{\partial x} \tag{5}$$

$$\frac{d\theta}{dt} = -\frac{\Delta H}{\rho_s c_s} \frac{d\bar{c}}{dt} + \frac{1}{\rho_s c_s (1-\epsilon)} \left\{ S - L \right\} \tag{6}$$

The solution of these equations is performed in the following manner. The integral term in equation (1) is integrated by parts to yield

$$\frac{d\bar{c}}{dt} = \frac{6D}{a^2} \sum_{n=1}^{\infty} \left\{ \psi(T_n) - e^{-KT_n} \left(\psi(\lambda) e^{K\lambda} \right)_0^{T_n} - \int_0^{T_n} \frac{d\psi}{d\lambda} e^{K\lambda} d\lambda \right\}$$

$$= \frac{6D}{a^2} \sum_{n=1}^{\infty} e^{-KT_n} \int_0^{T_n} \frac{d\psi}{d\lambda} e^{K\lambda} d\lambda \tag{7}$$

as $\psi(0) = 0$ for derivation and validity of equation (1).

The assumption is now made that ψ is linear in each time step so that

$$\frac{d\psi}{d\lambda} = \frac{\psi_i - \psi_{i-1}}{\lambda_i - \lambda_{i-1}} \tag{8}$$

in the ith time step, i = 1 at time zero.

Substitution of equation (8) into (7) yields

$$\frac{d\bar{c}}{dt} = \frac{6D}{a^2} \sum_{n=1}^{\infty} e^{-KT_n} \sum_{i=2}^{I} \left(\frac{\psi_i - \psi_{i-1}}{\lambda_i - \lambda_{i-1}} \right) \int_{T_{i-1}}^{T_i} e^{K\lambda} d\lambda$$

$$= \frac{6D}{a^2} \sum_{n=1}^{\infty} \frac{e^{-KT_n}}{K} \sum_{i=2}^{I} \left(\frac{\psi_i - \psi_{i-1}}{\lambda_i - \lambda_{i-1}} \right) \left(e^{KT_i} - e^{KT_{i-1}} \right)$$

which upon reversing summation signs yields

$$\frac{d\bar{c}}{dt} = \frac{6D}{a^2} \sum_{i=2}^{I} \left(\frac{\psi_i - \psi_{i-1}}{\lambda_i - \lambda_{i-1}}\right) \sum_{n=1}^{\infty} \frac{e^{-K(T_n - T_i)} - e^{-K(T_n - T_{i-1})}}{K} \tag{9}$$

As $T_n \geq T_i$ for all time steps, the infinite series

$$S_i = \sum_{n=1}^{\infty} e^{-K(T_n - T_i)}$$

converges for all time steps.

As $K = \frac{n^2 \pi^2}{a^2}$, the series to be evaluated has the form

$$S_i = \sum_{n=1}^{\infty} \frac{e^{-n^2 \alpha^2}}{n^2}$$

where $\alpha^2 \geq 0$.

The method used in evaluating this series is given in Appendix I.
Setting

$$C_i = \sum_{n=1}^{\infty} \frac{e^{-\frac{n^2 \pi^2}{a^2}(T_n - T_i)}}{n^2}$$

and substituting in equation (9) yields

$$\frac{d\bar{c}}{dt} = \frac{6D}{\pi^2} \sum_{i=2}^{I} \left(\frac{\psi_i - \psi_{i-1}}{\lambda_i - \lambda_{i-1}}\right) \left(C_i - C_{i-1}\right) \tag{10}$$

Equation (10) is then substituted into equation (3) and equation (5) into equations (3) and (4) to give

$$\epsilon \frac{\partial \rho_H}{\partial t} + (1 - \epsilon) \frac{6D}{a^2} \sum_{i=2}^{I} \left(\frac{\psi_i - \psi_{i-1}}{\lambda_i - \lambda_{i-1}}\right) \left(C_i - C_{i-1}\right) + \frac{\partial \rho_H V}{\partial x} = 0 \tag{11}$$

$$\epsilon \frac{\partial \rho_I}{\partial t} - \frac{\partial \left(\rho_I \frac{d}{u} \frac{\partial P}{\partial x} \right)}{\partial x} = 0 \qquad (12)$$

Finite difference equations are written for equations (11) and (12) in each of the zones into which the bed has been divided. If there are N zones, then equations (11) and (12) yield 2N equations and equation (2) yields N equations in the 3N unknowns, P_I, P_H, ψ_i, in each zone of the bed. The 3N equations in 3N unknowns are solved by the Newton-Rhapson method which converges rapidly. As u, θ, etc., are functionally related to P_I, P_H, ψ, an outer iterative loop is performed on equation (6) until the complete set of equations (1) to (6) converge. Usually about three or four iterations are required to converge on equations (11), (12), and (2), and four or five iterations to converge on the set of equations (1) to (6). The process is quite stable and allows use of large time increments.

Convergence is more critical initially, however, and smaller time steps must be used. The time step is adjusted automatically in the program to increase accuracy and decrease computer running time.

b. Computer Program

(1) Input

The necessary input data are given in the order in which they are read.

NZONES	Number of zones that the model is to simulate
NTAB	Number of pairs of table entries of time versus total pressure
INPT	Option (1): If INPT=0, the standard output is obtained
	Option (2): If INPT > 0, all intermediate calculations are printed out. This is useful in determining if the initial time increment is too large.
XA	Coefficient A in $Ae^{-B/R\theta}$
XB	Coefficient B in $Ae^{-B/R\theta}$
DP	Average particle diameter
FD	Shape factor for diffusion
DEPTH	Length of bed
EPS	Void fraction
FF	Shape factor for flow
TMAX	Maximum time the transient is to be computed (seconds)
DELTAT	Initial time increment
TAMB	Ambient temperature (°F)
TZERO	Initial bed temperature (°F)

Fi	Fraction of inert gas present
RHOS	ρ_s, density of solid
CESS	c_s, heat capacity of solid
AREA	Cross sectional area of bed
XKL	Heat loss coefficient
ESSN(J), J = 1, NZONES	S_n, volumetric heat generation rate
SIGI	σ_I, collision diameter of inert (Å)
EPSKI	$(\epsilon/K)_I$, Lennard-Jones energy characteristic of inert gas (°K)
XMI	Atomic weight of inert gas
(TP(J), Q(J))J = 1, NTAB	time versus pressure table
PIV1	Initial pressure of inert gas
PIV2	Pressure of inert gas at first time step
QEX	Mixing factor
ROMANV	Exhaust volume
DMAX	Maximum time increment
DMIN	Minimum time increment
BE	Klinkenberg constant

(2) Output

The printed output includes the temperature, hydrogen pressure, partial pressure caused from the inert gas, total pressure and average hydrogen particle concentration in each zone as well as the total amount of absorbed hydrogen.

The FORTRAN listing of HYDRA II is provided in Appendix II.

3. Experiment Planning Overview

a. Purpose

The proposed tests are being performed to determine the hydrogen absorption rates of porous zirconium hydride and uranium zirconium hydride bodies and to determine the effect of thermal and hydrogen cycling on these rates.

Porous bodies were prepared from spherical zirconium hydride, using a number of particle size-void fraction combinations, to illustrate the effect of body configuration on hydrogen response. Additionally, bodies were prepared from nonspherical particles to study the problems associated with use of the less expensive material. Finally, uranium zirconium hydride spheres were used so that any variation in hydrogen absorption characteristics resulting from the presence of the fuel could be observed.

During the previous experimental effort (AFWL-TR-66-16), absorption characteristics of relatively deep beds (three to four inches) of zirconium hydride powders were measured. The rates of absorption were found to be limited by a pressure drop within the beds. In an effort to observe both pressure drop and diffusion limited situations, sintered bodies having a nominal length of one centimeter were chosen for the present studies. Experimental conditions and body characteristics were selected to allow study of a large range of absorption rates.

b. Nature of Tests

The hydrogen absorption test subjected a body to a step-like change in hydrogen pressure. The absorption rate resulting from this change was measured by observing the pressure decay of a known volume of hydrogen gas. Experimental pressures and temperatures were varied parametrically. Selected runs were repeated in the presence of various amounts of inert gas, simulating the effect of possible gaseous fission product release in an operating reactor.

To calculate theoretical absorption rates, the permeability of the body to hydrogen flow at various pressure levels and Reynolds numbers must be known. Therefore, a series of permeability tests were run on each body. Pressure drop, pressure level, and flow rates were measured over a wide range of experimental conditions.

Temperature-hydrogen cycling tests were conducted on a number of selected samples. The temperature cycling induces a hydrogen pressure cycling of the bodies. Cycling limits were set by the range of hydrogen content variation anticipated in the TURPS core during a typical load change transient.

c. Expected Results

The results of the absorption tests were planned to provide the experimental data needed to verify the present analytical model used to describe the hydrogen absorption process. This model is evaluated by using the HYDRA II code. The experimental results provide more realistic body permeabilities for use in the code, and indicate the validity of applying literature values of the diffusion coefficient. The net result is the evolution of an accurate and reliable method of analyzing the hydrogen absorption process, verified by experiments over the range of parameters of interest in the TURPS design.

4. Experimental Program

   a. Experimental Conditions

   The conditions varied in the absorption tests were initial body temperature, pressure step and gas composition. Because a complete parametric study using all of the bodies was outside of the scope of the present program, only two of the bodies were so tested. The others were tested at fewer conditions.

   For convenience in identifying the various sintered bodies refer to table II. The identification numbers are used in later tabulations of the experimental conditions.

Table II

CHARACTERIZATION OF POROUS BODIES

Material	Particles	Type of Test	Number of Bodies	Identification
ZrH_x	Spherical	Absorption	5	S1, S2, S3, S4, S5
ZrH_x	Spherical	Cycling	2	S6, S7
$U_{0.044}ZrH_x$	Spherical	Cycling	3	F1, F2, F3
ZrH_x	Nonspherical	Absorption	2	N1, N2
ZrH_x	Nonspherical	Cycling	1	N3

   Table III shows the range of experimental conditions covered in the tests.

Table III

NOMINAL RANGE OF EXPERIMENTAL CONDITIONS

Type of Test	Condition	Range
Absorption	Initial body temperature (°F)	100 to 1500
	Pressure step (atm)	0.1 to 1.1; 0.5 to 1.5; 1.0 to 2.0
Permeability	Pressure level (psi)	1.0 to 50.0
	Reynolds number	0.0001 to 0.01
Cycling	Temperature cycle amplitude (°F)	200
	Atom ratio cycle amplitude	0.10

   b. Data Output

   The raw data generated during the absorption tests included the initial temperature and hydrogen dissociation pressure of the body. From these conditions, the initial hydrogen content was taken from the equilibrium diagram. The initial pressure of hydrogen and inerts in the reservoir tank was recorded as part of

the pressure-time trace on the recording oscillograph. The reservoir tempera-
ture was obtained. From these reservoir conditons, the total gas leaving the
reservoir as a function of time could be calculated. After correction for the
accumulation of gas in the gas space of the retort, the total hydrogen and inerts
entering the porous body were calculated.

An estimate of the absorption rates to be encountered during these tests was
obtained using the HYDRA code. This was done by assuming the bodies are sub-
jected to step changes in hydrogen pressure at the surface. The time constant
can be defined by

$$\frac{\Delta C}{\Delta C_\infty} = 1 - e^{-t/\tau}$$

where

ΔC = change in average hydrogen content of the body

ΔC_∞ = ultimate change, after an infinite time, of the average hydrogen
content of the body

t = time

τ = time constant

Figure 1 shows the calculated time constant for a body one centimeter in
depth at an initial temperature of 1150° F. The pressure at the face of the body
is stepped from 0.5 to 1.5 atmospheres. No inert gas was considered. The
bodies were assumed to be composed of spherical particles having average diam-
eters of 0.001 to 0.005 inch. Void fractions varied from 0.15 to 0.25.

Figure 2 shows the effect of temperature on the predicted time constant for
the same range of particle diameters and the same pressure step.

The presence of an inert gas tends to decrease the total hydrogen transport.
It may also speed the transient, since less transport will result from the pres-
sure step. Figure 3 shows the relative change in total hydrogen absorption as
a function of the percentage inerts for a typical set of conditions. The curves
were generated for the case where the mole fraction or partial pressure of the
inert gas did not change during the transient, which was the situation in the
present experiments.

Permeability was calculated from the formula

$$d = \frac{V\mu t}{\Delta P}$$

Temperature   = 1150° F
Pressure step = 0.5 to 1.5 atm
Bed thickness = 1.0 cm
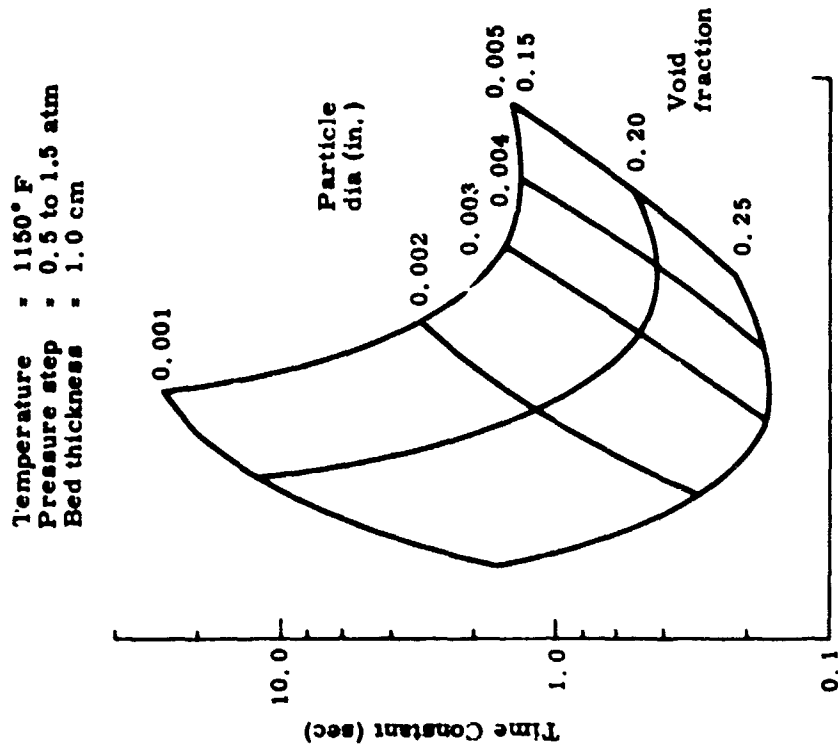
Figure 1. Hydrogen Absorption Time Constants
           in Porous Beds (slab geometry)

Void fraction   = 0.25
Pressure step   = 0.5 to 1.5
Bed thickness   = 1.0 cm
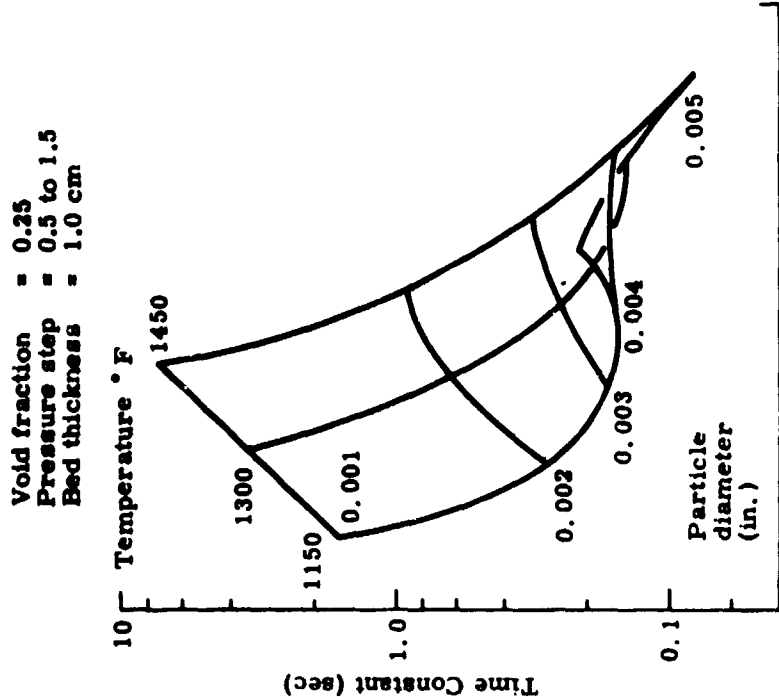
Figure 2. Hydrogen Absorption Time Constants
           in Porous Beds (slab geometry)

12
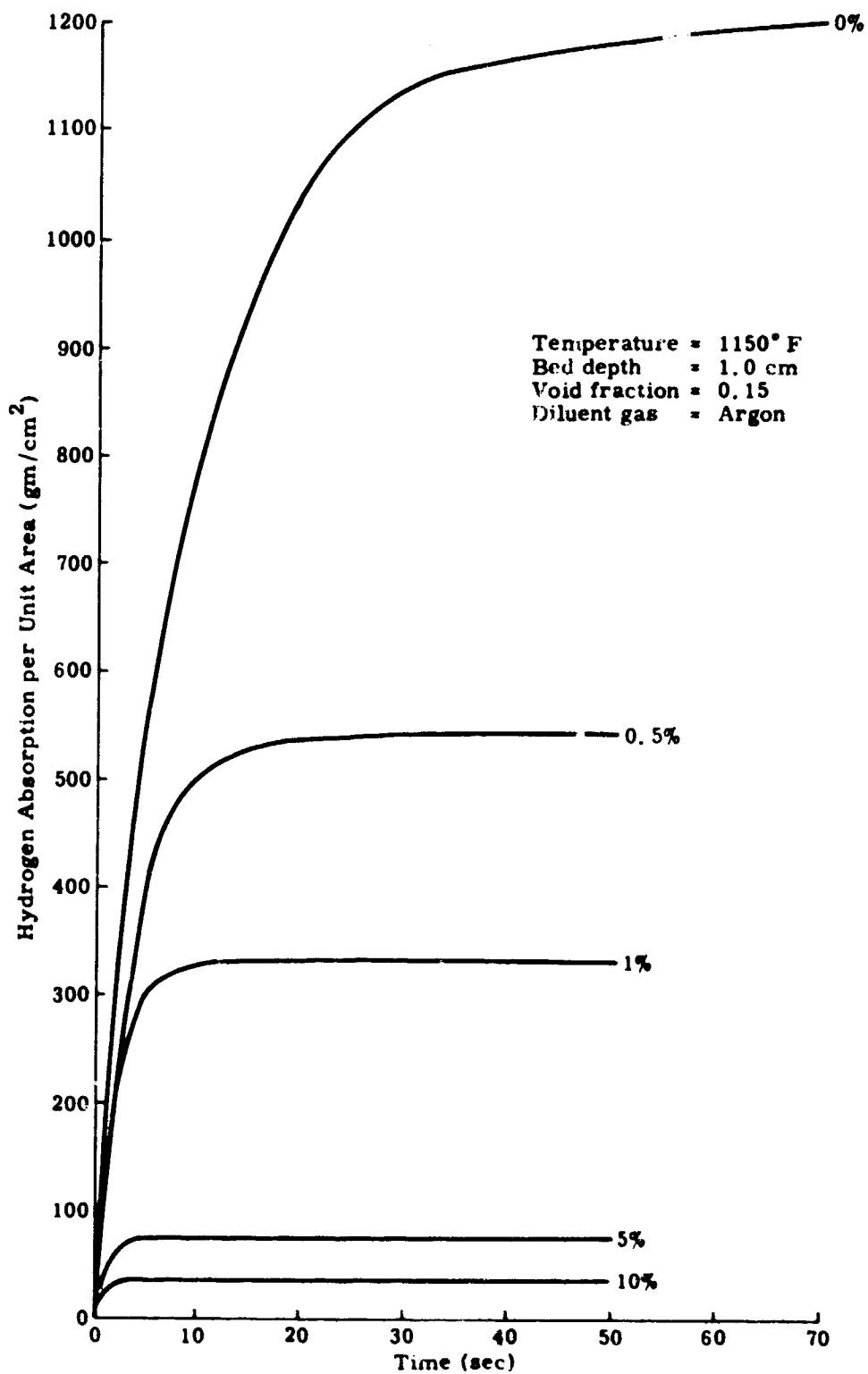
Figure 3. Effect of Inert Gas on Hydrogen Absorption

13

where

d   = permeability (cm^2)

V   = superficial gas velocity (cm/sec)

μ = viscosity of hydrogen (gm/cm-sec)

t   = thickness of body (cm)

ΔP = pressure difference (gm/cm-sec^2)

The velocity is calculated from the measured mass flow rate and the known density

$$V = \frac{w}{\rho A}$$

w   = flow rate (gm/sec)

ρ = hydrogen density (gm/cm^3)

A   = face area of body (cm^2)

The mass flow rate, pressure drop, absolute pressure, temperature and body face area were measured. Literature values of gas density and viscosity were used in the calculation of permeability.

Each of the bodies listed in table II was subjected to a minimum of three different hydrogen flow rates at three pressures in the range 1 to 50 psia. The cycled bodies were permeability tested both before and after the cycling. The flow rates depend upon the practical limitations of the pressure drop and flow rate measuring devices, i.e., pressure drop 0.02 to 20 psi and flow 10^{-4} to 10 gal/min. Figure 4 shows the predicted pressure drop for a range of Reynolds numbers, average particle diameter-shape factor products and pressure levels. These data are replotted in figure 5 to show the corresponding flow rates per unit area of body cross section.

Nominally, the bodies were cycled between 1200° and 1400° F. The void volume associated with the retort was sized so that the body will vary in atom ratio (H/Zr) by about 0.10. The retort pressure will cycle between 0.5 and 1.0 atmosphere.

c. Tabulated Plan of Runs

Table IV gives the complete schedule of absorption runs to be made. The letter prefix A indicates an absorption run while the final digit indicates duplicate runs at these condtions. In the case of cycled bodies, a final 8 indicates a test performed prior to cycling. A final 9 indicates a post-cycling test.
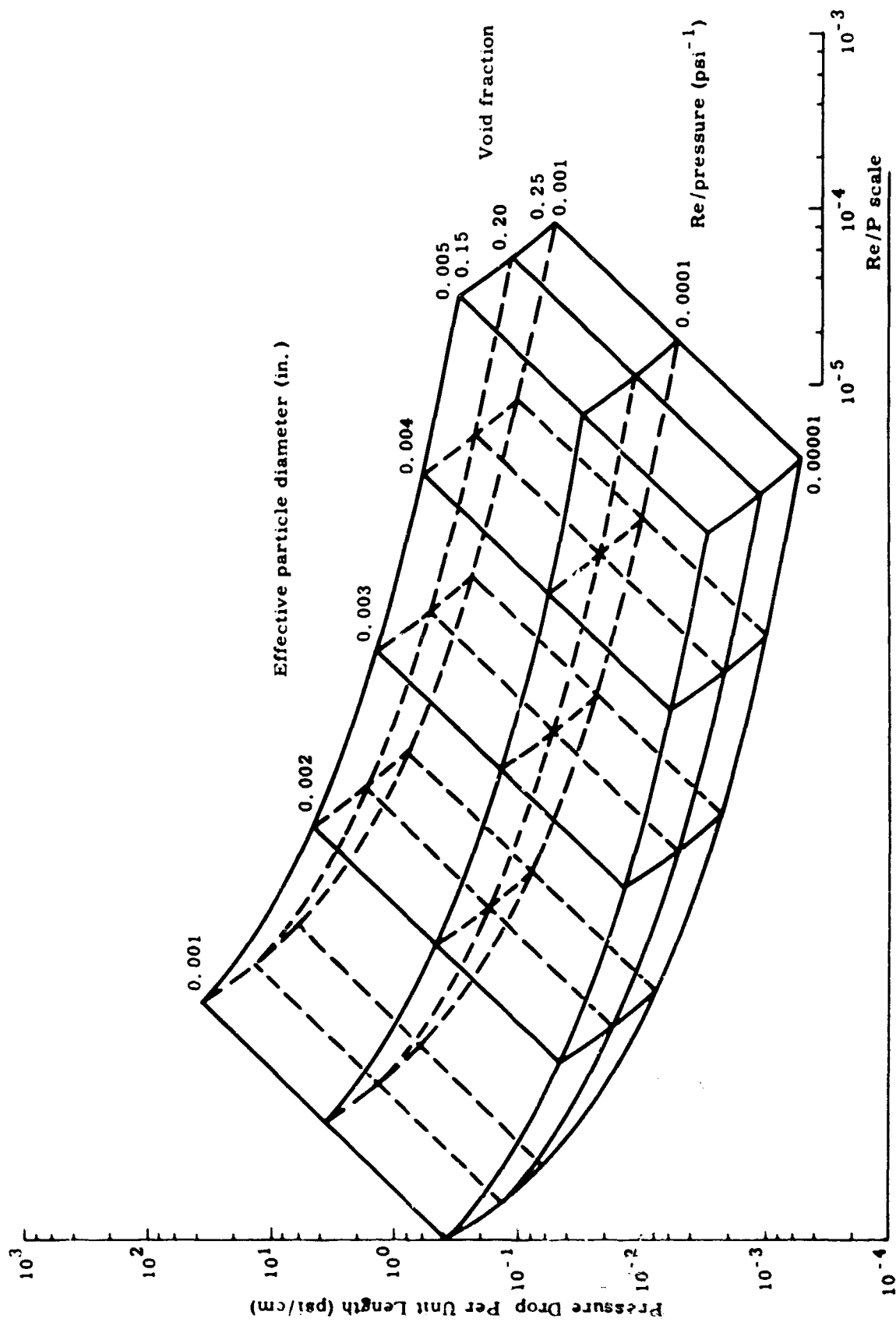
Figure 4. Anticipated Pressure Drops
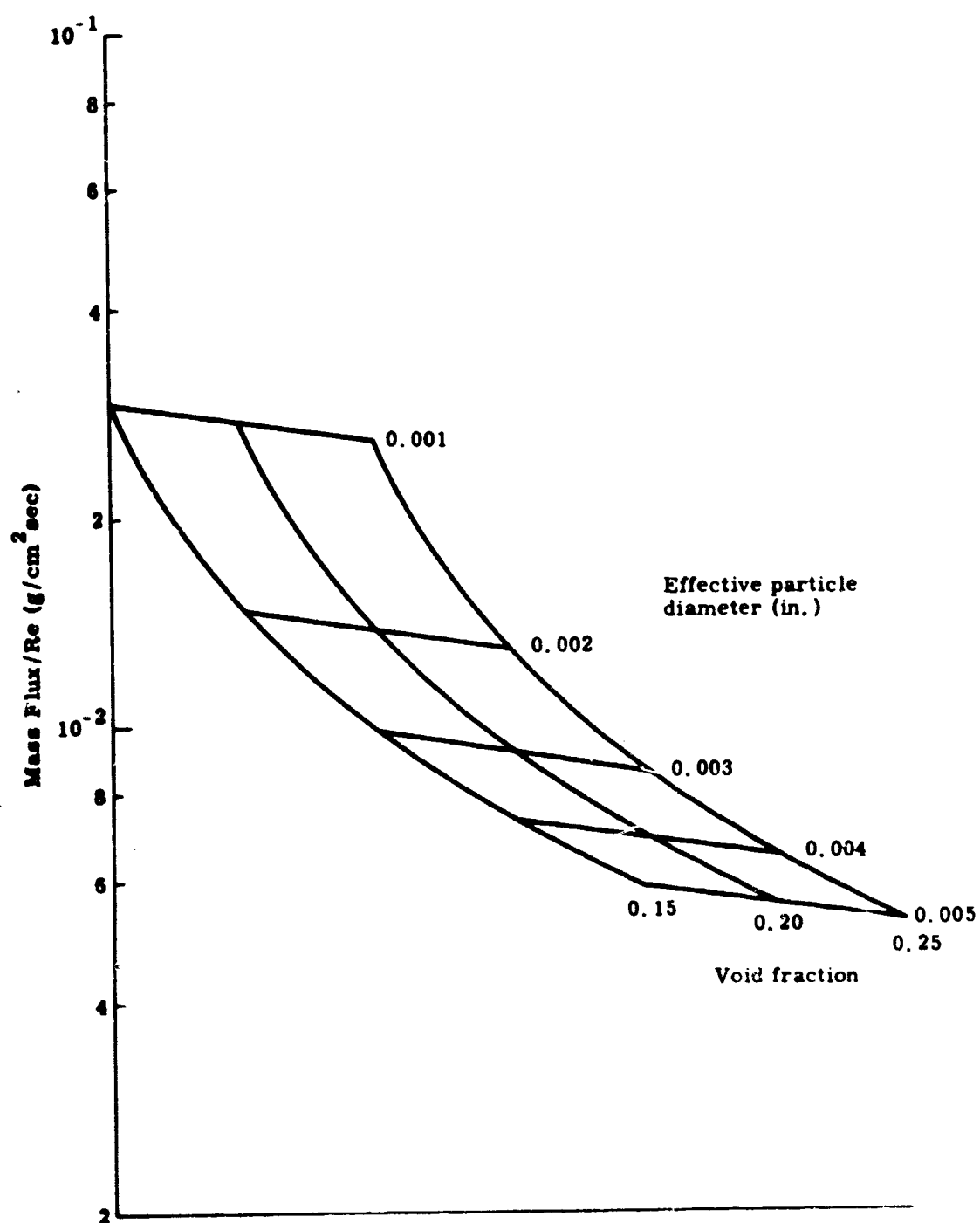
Figure 5. Anticipated Flow Rate

Table IV

HYDROGEN ABSORPTION TEST PARAMETERS

Run number	Body ID	Temperature (°F)	Hydrogen pressure step (atm)	Diluent gas	Diluent pressure (atm)
A010	S1	1000	0.1 to 1.1	None	0.0
A020		1150	0.1 to 1.1		
A030		1300	0.1 to 1.1		
A040		1400	0.1 to 1.1		
A050		1500	0.1 to 1.1		
A060		1000	0.5 to 1.5		
A070		1150	0.5 to 1.5		
A080		1300	0.5 to 1.5		
A090		1400	0.5 to 1.5		
A100		1500	0.5 to 1.5		
A110		1000	1.0 to 2.0		
A120		1150	1.0 to 2.0		
A130		1300	1.0 to 2.0		
A140		1400	1.0 to 2.0		
A150		1500	1.0 to 2.0	None	0.0
A160		1000	0.1 to 1.1	Argon	0 05
A170		1150	0.1 to 1.1		
A180		1300	0.1 to 1.1		
A190		1400	0.1 to 1.1		
A200		1500	0.1 to 1.1		
A210		1000	0.5 to 1.5		
A220		1150	0.5 to 1.5		
A230		1300	0.5 to 1.5		
A240		1400	0.5 to 1.5		
A250		1500	0.5 to 1.5		
A260		1000	1.0 to 2.0		
A270		1150	1.0 to 2.0		
A280		1300	1.0 to 2.0		
A290		1400	1.0 to 2.0		
A300	S1	1500	1.0 to 2.0	Argon	0.05
A310	S2	1000	0.1 to 1.1	None	0.0
A320	S2	1150	0.1 to 1.1	None	0 0

Table IV (cont'd)

Run number	Body ID	Temperature (°F)	Hydrogen pressure step (atm)	Diluent gas	Diluent pressure (atm)
A330	S2	1300	0.1 to 1.1	None	0.0
A340	↑	1400	0.1 to 1.1	↑	↑
A350		1500	0.1 to 1.1		
A360		1000	0.5 to 1.5		
A370		1150	0.5 to 1.5		
A380		1300	0.5 to 1.5		
A390		1400	0.5 to 1.5		
A400		1500	0.5 to 1.5		
A410		1000	1.0 to 2.0		
A420		1150	1.0 to 2.0		
A430		1300	1.0 to 2.0		
A440		1400	1.0 to 2.0	↓	↓
A450		1500	1.0 to 2.0	None	0.0
A460		1000	0.1 to 1.1	Argon	0.05
A470		1150	0.1 to 1.1	↑	↑
A480		1300	0.1 to 1.1		
A490		1400	0.1 to 1.1		
A500		1500	0.1 to 1.1		
A510		1000	0.5 to 1.5		
A520		1150	0.5 to 1.5		
A530		1300	0.5 to 1.5		
A540		1400	0.5 to 1.5		
A550		1500	0.5 to 1.5		
A560		1000	1.0 to 2.0		
A570		1150	1.0 to 2.0		
A580		1300	1.0 to 2.0		
A590	↓	1400	1.0 to 2.0	↓	↓
A600	S2	1500	1.0 to 2.0	Argon	0.05
A610	S3	1000	0.5 to 1.5	None	0.0
A620	S3	1150	0.5 to 1.5	None	0.0
A630	S3	1300	0.5 to 1.5	None	0.0

(table cont'd on next page)

Table IV (cont'd)

Run number	Body ID	Temperature (°F)	Hydrogen pressure step (atm)	Diluent gas	Diluent pressure (atm)
A640	S3	1400	0.5 to 1.5	None	0.0
A650	S3	1500			
A660	S4	1000			
A670	S4	1150			
A680	S4	1300			
A690	S4	1400			
A700	S4	1500			
A710	S5	1000			
A720	S5	1150			
A730	S5	1300			
A740	S5	1400			
A750	S5	1500			
A760	N1	1000			
A770	N1	1150			
A780	N1	1300			
A790	N1	1400			
A800	N1	1500			
A810	N2	1000			
A820	N2	1150			
A830	N2	1300			
A840	N2	1400			
A850	N2	1500			
A868	S5	1150			
A869	S6	1150			
A878	S6	1300			
A879	S6	1300			
A888	S6	1400			
A889	S6	1400			
A898	S7	1150			
A899	S7	1150			
A903	S7	1300	0.5 to 1.5	None	0.0

Table IV (cont'd)

Run number	Body ID	Temperature (°F)	Hydrogen pressure step (atm)	Diluent gas	Diluent pressure (atm)
A909	S7	1300	0.5 to 1.5	None	0.0
A918	S7	1400			
A919	S7	1400			
A928	N1	1150			
A929	N1	1150			
A938	N1	1300			
A939	N1	1300			
A948	N1	1400			
A949	N1	1400			
A958	F1	1150			
A959	F1	1150			
A968	F1	1300			
A969	F1	1300			
A978	F1	1400			
A979	F1	1400			
A988	F2	1150			
A989	F2	1150			
A998	F2	1300			
A999	F2	1300			
A1008	F2	1400			
A1009	F2	1400			
A1018	F3	1150			
A1019	F3	1150			
A1028	F3	1300			
A1029	F3	1300			
A1038	F3	1400			
A1039	F3	1400		None	0.0
A1040	Selected	1150		Krypton	0.15
A1050		1150		Krypton	0.015
A1060		1150		Krypton	Selected
A1070		1150		Xenon	0.15
A1080		1150		Xenon	0.015
A1090	Selected	1150	0.5 to 1.5	Xenon	Selected

(table cont'd on next page)

Table IV (cont'd)

Run number	Body ID	Temperature (°F)	Hydrogen pressure step (atm)	Diluent gas	Diluent pressure (atm)
A1100	Selected	1150	0.5 to 1.5	Oxygen	Selected
A1110	↑	1300	↑	↑	↑
A1120	│	1400	│	│	│
A1130	│	1150	│	│	│
A1140	↓	1300	↓	↓	↓
A1150	Selected	1400	0.5 to 1.5	Oxygen	Selected

Table V gives the nominal operating conditions of the cycling tests. The prefix C indicates a cycling run.

Table V

THERMAL CYCLING TEST PARAMETERS

Run number	Body ID	Temperature cycle (°F)	Pressure cycle (atm)
C010	S6	1200 to 1400	0.5 to 1.0
C020	S7	↑	↑
C030	F1	│	│
C040	F2	│	│
C050	F3	↓	↓
C060	N3	1200 to 1400	0.5 to 1.0

5. Apparatus and Test Procedures

a. Permeability

(1) Apparatus

A schematic of the main components of the permeability system is shown in figure 6, including valves, flowmeters, specimen holder assembly and pressure transducer connections. Provisions were included for flow and pressure measurement. Calibration curves prepared for each flowmeter were used to determine hydrogen flow rates for a given pressure and meter reading. Upstream pressures were measured by using the pressure gage and the absolute pressure transducer. Pressure drops across the test specimen were measured by using the differential pressure transducers. Output of these three transducers were recorded on an oscillograph.
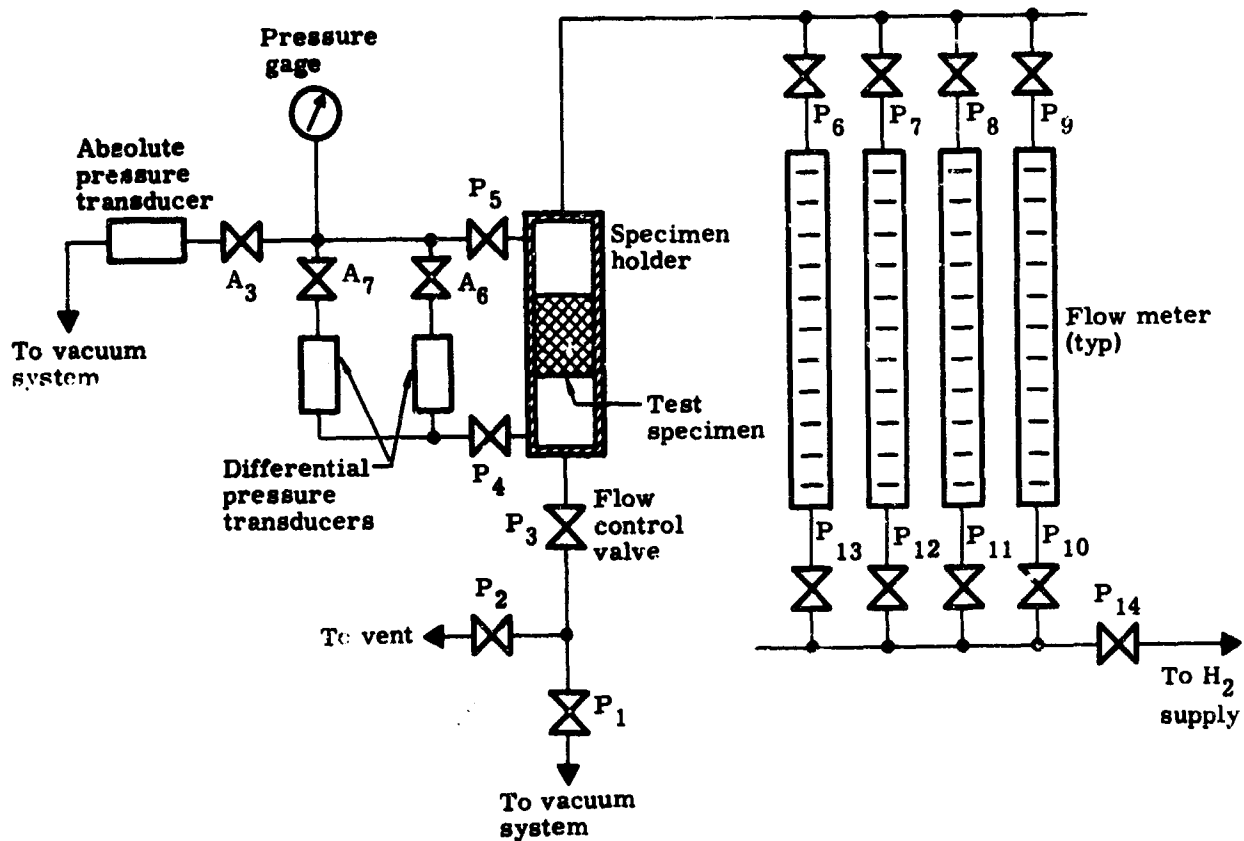
Figure 6. Hydrogen Permeation Test Apparatus

(2) Procedure

The procedure for performing the hydrogen permeability tests was as follows:

(1) Load the test specimen into the holder assembly, and evacuate the system to 10^{-3} torr by opening valves P_1 through P_{13}, excluding P_2. In addition, valves A_3, A_6 and A_7 were open, while valves A_2, A_5, and A_8 were closed (Cf. figures 6 and 7).

(2) Isolate vacuum pump at P_1 and check for vacuum leaks. Close valves opened in (1).

(3) Depending on the flow rate desired, open the valves at entrance and exit sections of the selected flowmeter.

(4) Open valve P_{14} and valve P_1 or P_2 to initiate flow. P_1 was used to obtain low pressure data while P_2 was used for certain high pressure runs.

(5) Make the valve adjustments required to obtain desired mass flow rate and pressure level.

All permeability test data pertaining to each specimen were documented, including: identification number, flow rates and corresponding pressure levels and pressure drops. In addition, it was noted whether the test specimen had previously undergone thermal cycling.

b. Hydrogen Absorption

(1) Apparatus

Basic components of the hydrogen absorption system, including arrangement of vacuum-pressure lines, are shown by figure 7. Valves are numbered to assist procedure instructions. Two gas supply lines were provided, one for hydrogen (valve A_{10}) and one for inert gas (valve A_9).

This system was so designed that with an initial pressure differential of 14.7 psi between the retort and the surge tank, the maximum pressure decay within the surge tank, after opening the solenoid valve (A_4), will be 2 psi. Pressure instrumentation includes two gages (0 to 100 psi), one on either side of valve A_4 and three transducers. The absolute pressure transducer (0 to 20 psi) has a dynamic vacuum on the negative side with the retort pressure on the positive side. The differential pressure transducers can be operated with either a dynamic vacuum or surge tank pressure on the negative side. Surge tank pressure was monitored on the positive side of the transducer.
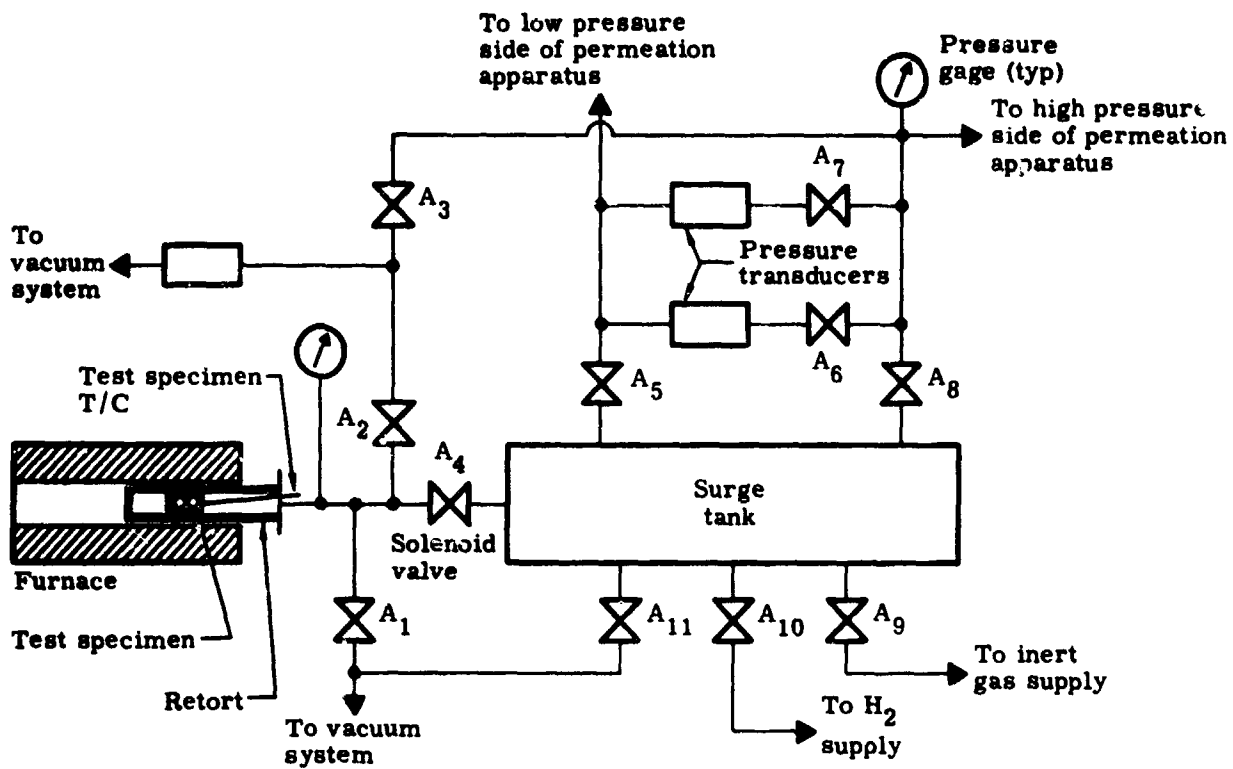
Figure 7. Hydrogen Absorption Test Apparatus

Furnace control instrumentation is shown in figure 8. The Simplytrol meter was set to shut off the furnace power whenever the furnace control thermocouple indicated 1550° F or above. Retort thermocouples are connected to the millivolt recorder. The sheath (specimen) thermocouple is connected to the oscillograph, as are the pressure transducers.

(2) Procedure

The procedure for performing hydrogen absorption tests is as follows:

(1) Load the specimen into a retort as indicated by figure 9, making certain that the sheathed thermocouple is in contact with the sample.

(2) Connect retort to system. Evacuate entire system to 10^{-3} torr by opening valves A_1 through A_8 (figure 7). Valve C_6 of figure 10, and valves P_4 and P_5 of figure 6 remain closed. Check for vacuum leaks by isolating vacuum pump (valve A_1).

(3) Close valves A_1, A_3, A_4, A_9, A_{10} and A_{11}.

(4) Heat specimen to test temperature.

(5) After reaching the pressure-temperature equilibrium of the specimen, pressurize surge tank to a pressure 14.7 psi greater than that of the retort. If desired, a mixture of hydrogen and inert can be obtained by manipulation of valves A_9 and A_{10}.

(6) Close valves A_8, A_9 and A_{10}.

(7) Start oscillograph, recording specimen temperature and the output of the pressure transducers.

(8) Open the solenoid valve A_4. If the subsequent pressure drop in the surge tank exceeds 0.2 psi, close valve A_7.

(9) After pressure equilibrium of surge tank-retort, close valve A_4.

(10) Proceed to next test condition.

(11) After test completion, isolate and cool the retort to room temperature and remove the test specimen.

All absorption test data pertaining to each specimen were recorded as follows: identification number, weight before and after test, dimensions, composition, and surface condition. Hydrogen content was determined by equilibrium pressure temperature data and specimen weight change. Because the retort was
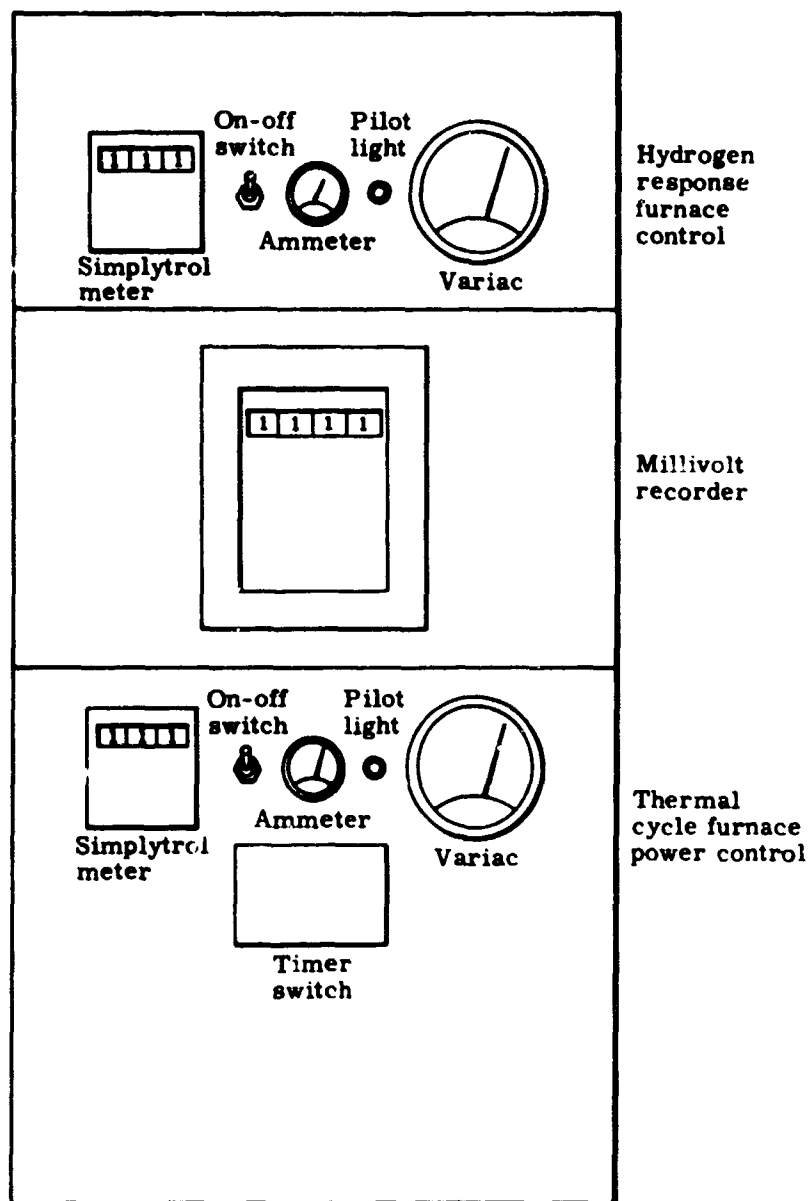
Figure 8. Furnace Control Console
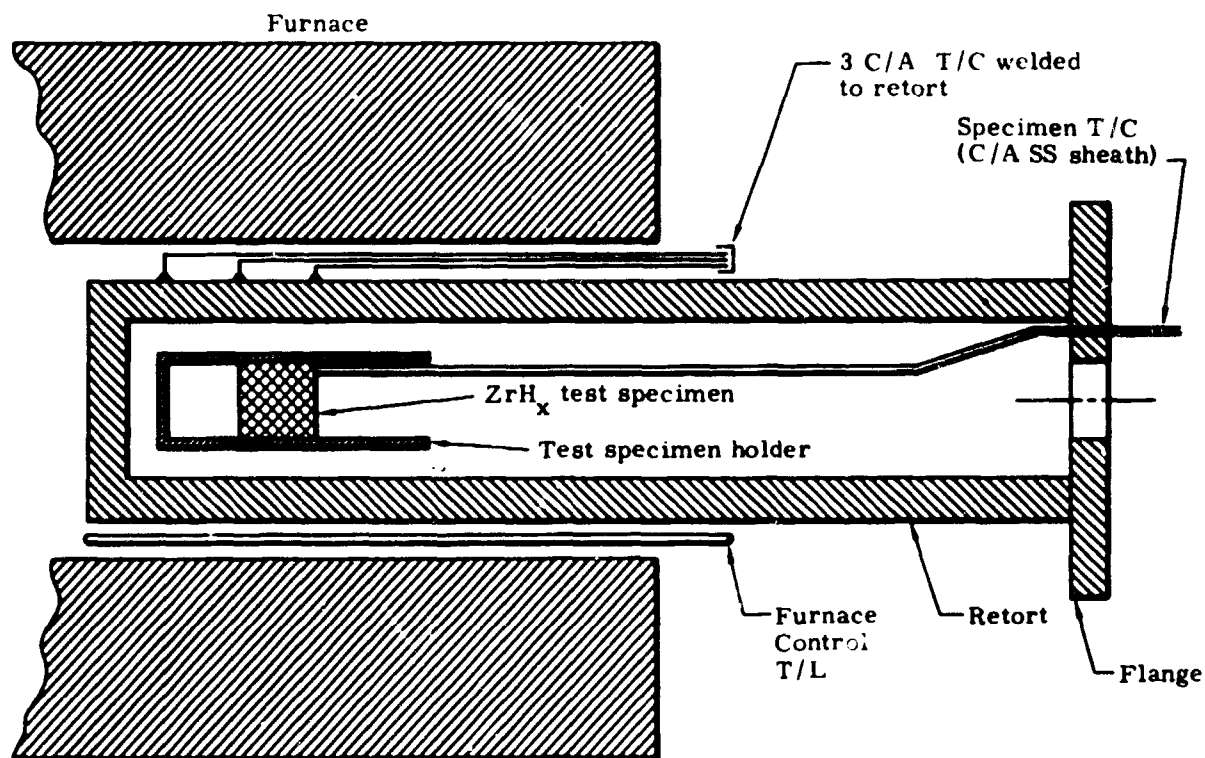
Figure 9. Typical Specimen Loading for Hydrogen Absorption and Thermal Cycle
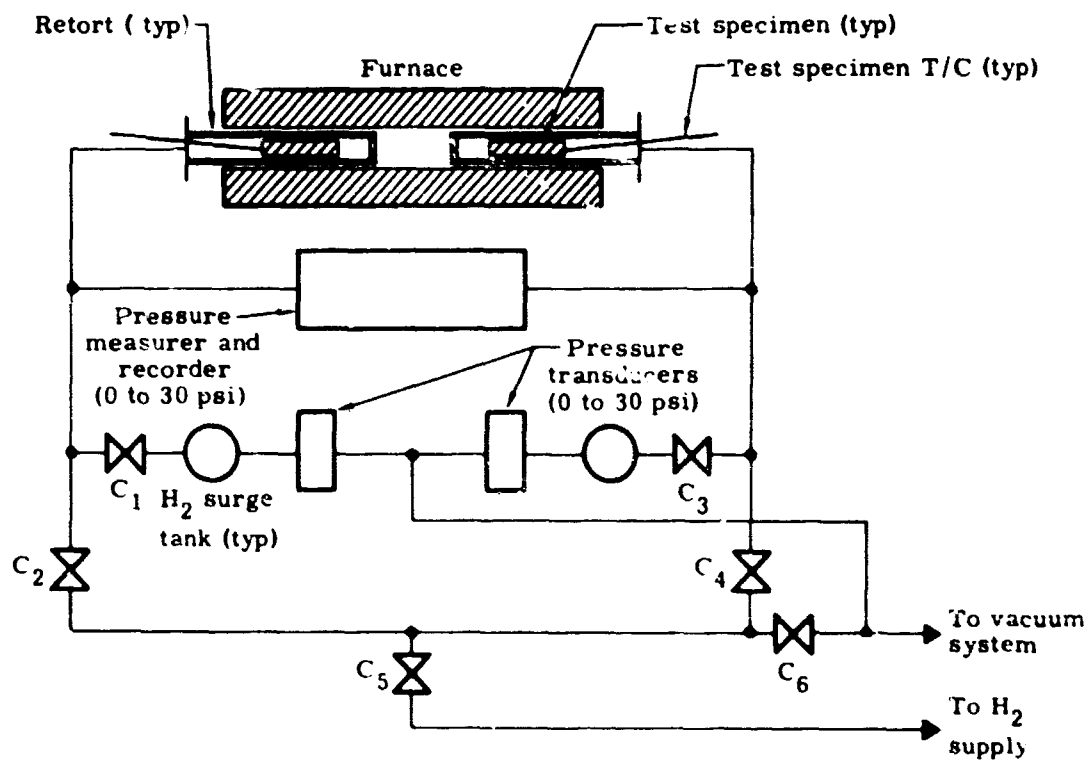
Figure 10. Thermal Cycle Test Apparatus

27

not at a uniform temperature, the amount of hydrogen in this void volume was difficult to calculate accurately. However, an "equivalent" void volume was measured. With the use of a dummy test specimen, the retort was pressurized at room temperature, the specimen temperature was increased to T_h, and the corresponding increase in pressure was measured. The equivalent volume was then calculated by the equation:

$$V_e = V_c \frac{P_c T_h}{P_h T_c}$$

where

V_e = equivalent volume occupied by the gas at temperature T_h

T_c = room temperature

P_c = pressure at T_c

V_c = gas volume at T_c

T_h = specimen temperature after heating

P_h = pressure at T_h

In this manner, an equivalent volume-temperature correlation was determined to cover the temperature range of hydrogen absorption testing. Thus, the moles of hydrogen which occupy this space during testing were calculated. Similar volume determination tests were performed on the thermal cycle retorts.

Initial pressures and temperatures of the surge tank and retort were recorded, as well as the oscillograph traces showing subsequent pressure-temperature changes after valve A_4 was opened.

c. Thermal Cycling

(1) Apparatus

The schematic of figure 10 shows the basic components of the thermal cycle system, including the arrangement of the vacuum-pressure lines. Each valve was numbered to simplify procedural instructions. Furnace control instrumentation is shown by figure 8. The Simplytrol meter is set to shut off the furnace power whenever the furnace control thermocouple or indicator rises to 1450° F. The timer switch is set to cycle the furnace between 1200° and 1400° F. The sheath (specimen) thermocouple and the retort thermocouples are connected to the millivolt recorder. The pressure transducers are connected to the oscillograph. Transducers operate with a dynamic vacuum on the negative side, and with the surge tank pressure on the positive side. A pressure line from each retort is connected to the pressure recorder (0 to 100 psi).

This system was designed to cycle the ZrH_x (or $ZrUH_x$) specimens between 1200° and 1400° F, with a corresponding pressure cycle of 7.4 to 14.8 psi. This represents about 0.02 gram of hydrogen movement, or six percent of the initial hydrogen in the specimens. Provision was included for the continuous monitoring of temperature and pressure throughout testing.

(2) Procedure

The procedure for performing thermal cycling tests is as follows:

(1) Load test specimens into retort as indicated by figure 9 making certain that the sheathed thermocouple is in contact with the sample.

(2) Connect retorts to system. Evacuate entire system to 10^{-3} torr by opening valves C_1 and C_6. Valves A_1 and A_{11} of figure 7 are closed. Check for vacuum leaks by isolating vacuum pump.

(3) Close valves C_2, C_4 and C_6. Heat specimens to 1200° F.

(4) After temperature equilibrium is attained, adjust pressure of retorts to 7.4 psi.

(5) With valves C_1 and C_3 opened and the remaining valves closed, initiate thermal cycling by adjustment of the timer switch (Cf. figure 8).

(6) After test completion (200 hours each of continuous cycling), the specimens are cooled to room temperature and removed from the retorts.

All cycling test data pertaining to each specimen are recorded as follows: identification number, weight before and after test, dimension, composition and surface condition. Amounts of hydrogen added to, or taken from, the test specimen are noted. In addition, typical strip chart recordings of temperature and pressure cycles are preserved.

6. Experimental Performance and Method of Data Reduction

a. Permeability

(1) Experiment

A thorough discussion of the experimental apparatus and test procedure was given in the preceding paragraphs. In brief, a gas underpressure was admitted at the end of the specimen and allowed to flow through the sintered body. The observed data consisted of the gas pressure and temperature, gas mass flow rate, the pressure drop over the length of the sintered body and the sintered body physical properties.

(2) Data reduction

Reduction of the raw data was performed by the digital code PERMA. The permeability coefficient was evaluated from Darcy's Law which states that the velocity of a gas (V) through a bed of solids is directly proportional to the pressure drop (dP/dx), and inversely related to the viscosity of the gas (μ), where the constant of proportionality is the permeability (d).

$$V = -\frac{d}{\mu}\frac{dP}{dx} \tag{13}$$

Because the mass flow rate (w) is related to the velocity by

$$w = \rho VA,$$

and employing the ideal gas law to evaluate the density,

$$\rho = \frac{P}{RT}$$

equation (13) becomes

$$d = R \left(\frac{\Delta X}{A}\right) \left(\frac{T\mu}{P}\right) \left(\frac{w}{\Delta P}\right) \tag{14}$$

where

    R   = ideal gas constant

    ΔX = specimen thickness

    A   = total cross section area of specimen perpendicular to the gas flow

    μ = viscosity of the gas at temperature (T) and pressure (P)

    P   = pressure drop across the specimen for a gas mass flow rate of w.

Equation (13) defines the pressure drop equal to zero for a gas velocity equal to zero. Thus, if one were to plot the gas velocity versus the pressure drop on a Cartesiar graph, a straight line through the origin would result with a slope proportional to the permeability constant. It was observed early in the data reduction that measurements at low mass flow rates produced relatively erratic results. The cause was eventually traced to instrument error bands. However, to evaluate the data, each data point was assigned a weighing factor (W) based upon the "lever" or "moment" principle.

$$W_i = \frac{\left(\Delta P_i^2 + w_i^2\right)^{1/2}}{\left(\Delta P_{max}^2 + w_{max}^2\right)^{1/2}}$$

Thus, the farther the data point was from the origin, the higher the weighing factor ($W_{max} = 1$). The average permeability was then evaluated by the following:

$$\bar{d} = \frac{\sum\limits_i W_i d_i}{\sum\limits_i W_i}$$

This technique of data reduction provided an excellent means of screening the experimental data and an immediate identification of questionable data points.

The standard deviation (SD) of the experimental permeability from the average value was calculated by

$$SD = \sum_{i=1}^{N} \frac{\left(d_i - \bar{d}\right)^2}{N - 1}$$

The range of the various parameters is given in table VI. Permeability measurements were made before and after the hydrogen absorption tests and before and after thermal cycling of the specimens.

Table VI

RANGE OF PARAMETERS--PERMEABILITY TEST

Parameter	Range
Pressure (psia)	35
Pressure drop (psia)	0.01 to 0.5
Gas mass flow (gm/run)	0.005 to 0.5
Specimen void fraction (%)	20 to 35
Specimen average particle size (mils)	1.0 to 6.5
Type of gas	A, H_2

b. Hydrogen Absorption Test

(1) Experiment

The experimental apparatus was divided into two sections: the retort section which contained the test specimen in an Inconel tube and furnace assembly, and the surge tank section which contained the pressurized hydrogen gas at room temperature. These two sections were connected by stainless steel tubing through a solenoid valve. The temperature of the top surface of the specimen was measured by a thermocouple which protruded through the retort flange and extended down to the specimen area.

The hydrogen pressure and specimen temperature in the retort were allowed
to come to a steady state equilibrium. The surge tank was then pressurized to a
level of approximately one atmosphere higher than that of the retort. Because
the system volumes were predetermined, the mass of hydrogen in each section
was known. The solenoid valve separating the two sections was then opened for
greater than 0.1 second but less than one second. The pressure drop in the
surge tank and the pressure rise and subsequent decay in the retort were meas-
ured by pressure transducers and recorded on an oscillograph.

The observed data consisted of the temperature and the initial and final pres-
sure in the surge tank, and the initial temperature and pressure and pressure
variation with time in the retort.

Initial hydrogen pressure and initial temperature were varied to observe
their effects on the absorption process for a given porous body. Specimens of
varying particle size and void fraction were tested in this way. To study the
influence of inert gases, the surge tank was initially pressurized with a mixture
of hydrogen and inert gas. Gases investigated were argon, krypton, and xenon.

(2) Data reduction

The reduction of the raw data was accomplished using the digital computer
code RESPND to solve the hydrogen continuity equation. At any time (t > 0):

Change in H_2 mass = change in H_2 mass + mass of H_2 absorbed + leakage

(surge tank)   (retort)   (specimen)

$$\left(\frac{\Delta PV}{RT}\right)_s = \left(\frac{\Delta PV}{RT}\right)_R + \frac{1.008 \ w_{Zr} \Delta X}{91.22} + Lt \quad (15)$$

where

ΔP = time dependent pressure differential $(P_t - P_o)$

V = volume

T = temperature

R = gas constant

w_{Zr} = weight of zirconium specimen

ΔX = change in H/Zr atom ratio $(X_t - X_o)$

L = leakage rate

t = accumulated test time

Equation (15) was used to reduce the experimental data to a time history of the percent of change in hydrogen content of the specimen because of absorption:

$$\% \; H_2 \; change = \frac{\Delta X}{X_o} \times 100\% \tag{16}$$

In selected cases, results obtained from the data reduction code were compared with those obtained from the digital computer code, HYDRA II.

c. Thermal Cycling Test

(1) Experiment

Four nonuranium-containing hydride specimens were subjected to the thermal cycling test. The procedure consisted of heating the specimens to approximately 1000° F under a dynamic vacuum. The specimens were then rehydrided to varying initial hydrogen-to-zirconium atom ratios (H/Zr), by proper selection of initial hydrogen pressure and specimen temperature. The minimum and maximum temperature points were then set on a temperature controller and the cycling commenced.

(2) Data reduction

The raw data generated by the cycling test consisted of temperature and pressure time histories recorded on chart paper. These records were then scanned to obtain the minimum and maximum temperatures and pressure variation in order to evaluate the net hydrogen movement during a cycle.

7. Experimental Program

a. Results and Analysis

Thirteen sintered specimens of varying powder particle sizes and shapes and void fractions were fabricated for this study. The pertinent body characteristics of the spherical and nonspherical zirconium hydride bodies are listed in table VII. The fuel bearing specimens are described in the classified volume II.

The particle sizes used to prepare the sintered compacts are reported as a function of bracketing USBS sieve numbers. For example, the particle diameter of a powder sample that went through an 80-mesh sieve but did not go through a 100-mesh sieve (-80 +100) would be in the range of 7.0 to 5.9 mils. This means of determining the powder particle size introduced an uncertainty of at most 8.5 percent based on the mean value. This uncertainty is further complicated when two mesh fractions are combined. Although this error in measured

particle size did not affect the data reduction of the experimentally determined permeability, it did contribute to uncertainties in the theoretical value for permeability as calculated from the Ergun correlation. Also, use of this average particle size in the hydrogen absorption predictions (HYDRA) introduced uncertainties into the analysis.

Table VII

SINTERED BODY CHARACTERISTICS

Specimen*	Powder mesh size	Average particle diameter (mils)	Void fraction
S1	100% of -270 +400	1.8	0.2229
S2	100% of -270 +400	1.8	0.2346
S3	100% of -150 +170	3.8	0.2336
S4	100% of -150 +170	3.8	0.2042
S5	100% of -400	1.0	0.2095
S6	100% of -80 +100	6.5	0.22682
S7	100% of -80 +10^	6.5	0.2342
N1	80% of -80 +100	5.52	0.2492
	20% of -325 +400		
N2	80% of -80 +100	6.2	0.2733
	20% of -100 +140		
N3	80% of -140 +200	3.1	0.2461
	20% of -325 +400		

*S = spherical powder specimen
N = nonspherical powder specimen

(a) Permeability

The empirical correlation for the permeability of a packed bed as a function of the bed characteristics proposed by Ergun states that in the case of laminar flow (Reynolds number < 10) the permeability is predicted by

$$d = \frac{D_p^2 \, f_F^2 \, \epsilon^3}{150 \, (1-\epsilon)^2} \tag{17}$$

where

d = permeability

D_p = particle diameter

ϵ = void fraction

f_F = shape factor

A comparison of the empirical or Ergun permeability evaluated from equation (17) and the experimental value evaluated from equation (14) was given in table VIII for pre- and post-hydrogen absorption or thermal cycle test conditions. The physical properties of the sintered bodies (grain or particle size, void fraction, etc.) are a function of the sintering temperature and the length of time a body is subjected to this temperature. Thus, as long as the test conditions are lower than the minimum sintering temperature (~1700° F), one should observe negligible change in the body structure and the effects of continual absorption and desorption of hydrogen and phase changes should be self-evident.

Table VIII

HYDROGEN PERMEABILITY

Specimen	Ergun	Permeability x 10^{+9} (cm^2)	
		Pretest	Post-test
S1	2.556	4.981	--
S2	3.069	4.896	4.780 6.725
S3	13.481	16.469 20.529	20.259
S4	8.355	11.357	11.941
S5	0.633	1.157 1.313	1.423
S6	35.471	--	35.720
S7	39.804	--	54.873
N1	35.992	--	7.626
N2	63.941	19.753	21.097
N3	10.846	4.528	4.364

Examination of the pre- and post-test permeabilities showed that essentially no change occurred. Variations are within the experimental error.

In order to compare the permeability of the porous sintered bodies with that predicted by Ergun for a packed bed containing the same void fraction and particle size, an effective particle size ($f_F x D_p$) evaluated by a rearrangement of equation 10 is defined.

$$\text{Effective particle size } (f_F \times D_p) = \left(\frac{150 (1 - \epsilon)^2 \, d}{\epsilon^3} \right)^{1/2}$$

A plot of the effective particle size based on the experimentally determined permeability versus the actual or measured particle size as determined from the sieve sizes is shown in figure 11. The slope of these lines is particle shape factor. Theoretically, the shape factor for spherical particles is unity, while nonspherical particles have shape factors of less than one. As noted on figure 11, the shape factor for bodies composed of sintered spherical particles is slightly greater than one. This higher value seems real and cannot be attributed to any experimental error. It can be explained by the fact that the void structure in a sintered body is more open, that is, the voids form channels, thus, lowering the pressure drop for a given flow rate. The sintered bodies composed of non-spherical particles have shape factors less than unity. The exact value of the shape factor was obscured because of the uncertainty in determining the actual partical size of the powder. However, the results are in close agreement with expected behavior.

Prior to starting the test program, it was postulated that there might be a pressure effect upon the permeability. As shown in figure 12, the hydrogen permeability is virtually constant over the range of pressures investigated. It should be noted that each data point on the graph represents numerous runs of varying hydrogen gas mass flow rates and pressure drops at constant pressure. Variations can be attributed to inherent experimental errors.

The effect of the constituent gas on permeability was also investigated by using hydrogen and argon for two pretest bodies. The results of this experiment are given in table IX. The permeability of the porous sintered bodies was apparently independent of the type gas used.

b. Hydrogen Absorption

The primary objective of this study was the evaluation of the hydrogen absorption response of porous zirconium hydride bodies for varying conditions. In performing this study, it was necessary to examine the effect of numerous combinations and permutations f the pertinent parameters. Rather than inundate the
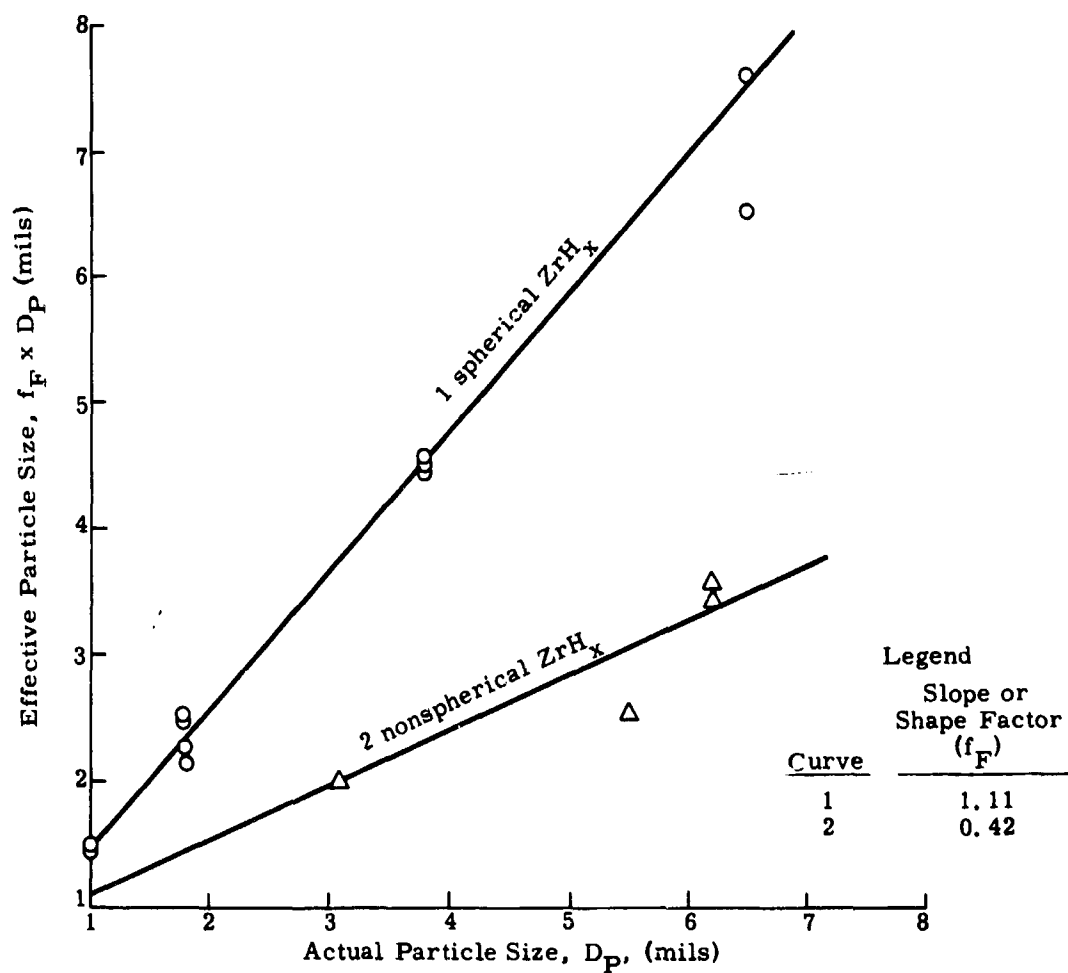
Figure 11. Hydrogen Permeability for Porous ZrH_x Sintered Bodies
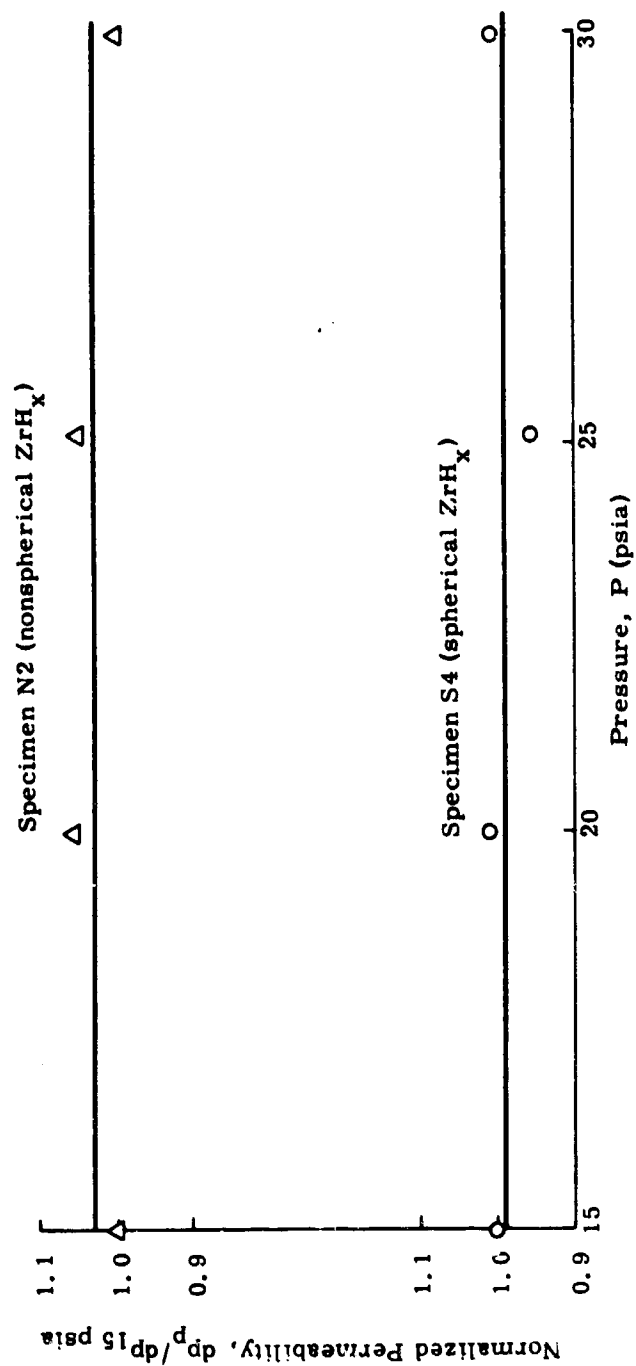
Figure 12. Pressure Effect Upon Permeability

reader with a myriad of data plots which may obscure the facts, the findings of this study will be discussed and specific plots will be introduced to substantiate the experimental observations.

Table IX

EFFECT OF CONSTITUENT GAS ON PERMEABILITY

	Permeability x 10^9 (cm^2)	
Specimen	Hydrogen	Argon
S2	4.896	4.346
S3	16.469	16.940
S3	20.529	16.370

(1) Temperature effect

Increasing the initial steady state temperature of a specimen results in the following:

(1) An increase in the hydrogen mass diffusion coefficient

(2) An increase in the H/Zr atom ratio differential for a constant pressure change.

Thus, the temperature effect would be one of increasing the rate of absorption with increasing specimen temperature. Table X illustrates these effects by comparing the percent change in the H/Zr atom ratio after a test time of 30 seconds as a function of initial specimen temperature. The pressure function in each case was a ramp change in hydrogen pressure from 0.5 to 1.5 atmospheres. Thus, an increase in the rate of hydrogen absorption with increasing initial temperatures was observed. This relationship is not a simple one because, as shown in figure 13, two different mechanisms are prevalent. In the first region (lower temperature region) the variation of the percent of hydrogen absorbed is almost linear with temperature. The second region exhibits an extreme temperature sensitivity. The particle diameter determines the slope of the linear portion of the curve. For small diameters, mass diffusion of hydrogen proceeds rapidly and is less sensitive to temperature. However, as the particle diameter increases, the temperature and, consequently, the diffusion coefficient have an increasing effect (steeper slope) upon the hydrogen absorption response. Figure 14 illustrates the same phenomena for the nonspherical particle specimens. This figure is a clear example of the effect of particle size as predicted earlier. In the low temperature range, the small particle size showed more rapid response
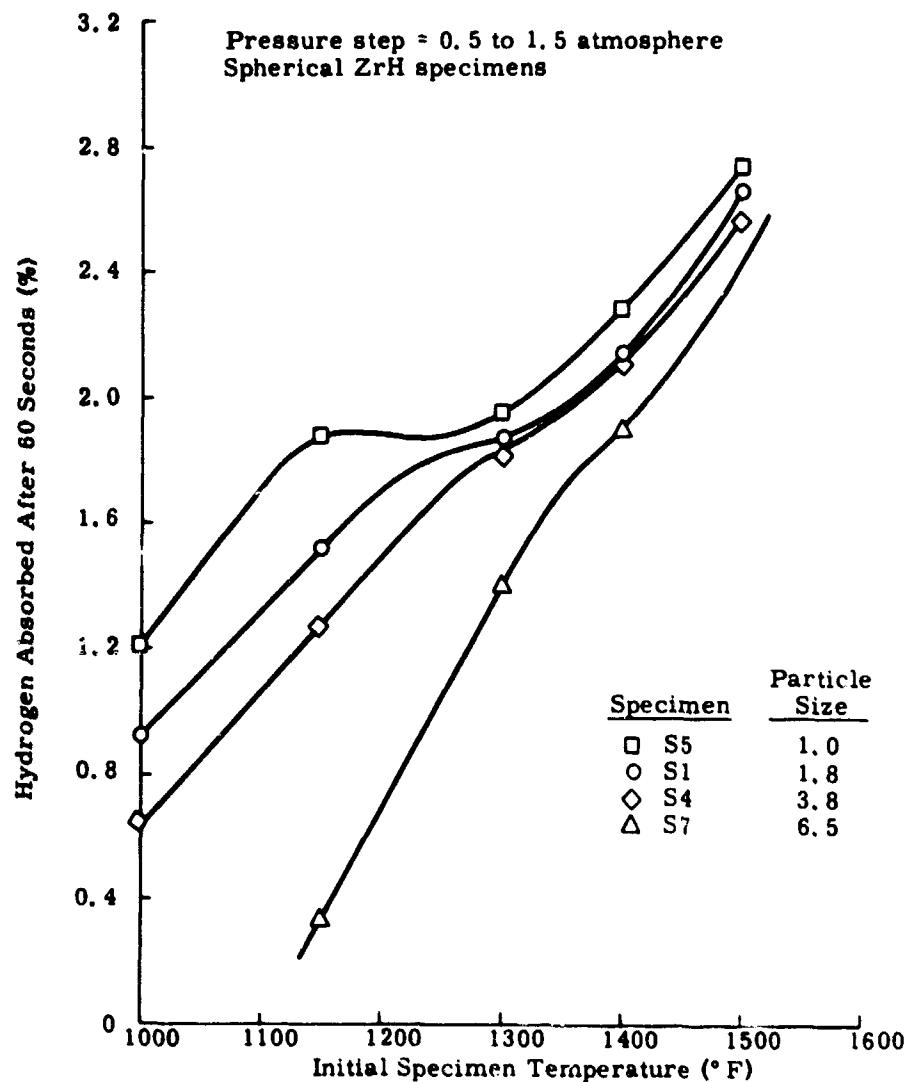
Figure 13. Hydrogen Absorption Response as Function of Initial Specimen Temperature and Particle Size
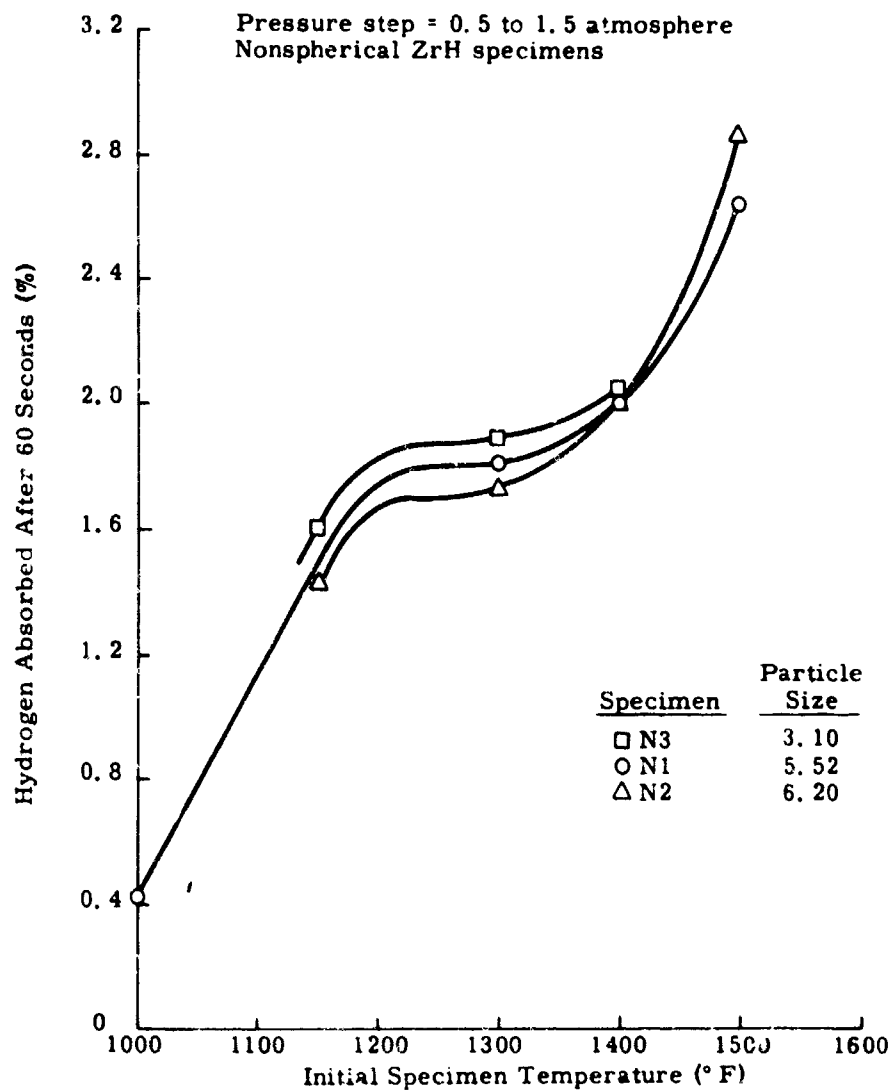
Figure 14. Hydrogen Absorption Response as Function of Initial Specimen Temperature and Size

because the rate of absorption was limited by the diffusion process. At higher temperatures, the order was reversed because diffusion was no longer an important rate-determining mechanism and body permeability becomes dominant. Figures 15 and 16 show the percent change in hydrogen concentration for the spherical and nonspherical particle specimens as a function of test time.

Table X

HYDROGEN ABSORPTION RESPONSE FOR HYDROGEN PRESSURE
RAMP OF 0.5 TO 1.5 ATMOSPHERES AS FUNCTION OF
INITIAL SPECIMEN TEMPERATURE

Specimen	Particle diameter (mils)	Change in H/Zr Atom Ratio After 60 Seconds (%)				
		1000° F	1150° F	1300° F	1400° F	1400° F
S1	1.8	0.919	1.520	1.875	2.135	2.657
S2*	1.8	ND	ND	2.083	2.715	3.54C
S3*	3.8	0.018	0.042	ND	1.652	3.086
S4	3.8	0.633	1.273	1.824	2.115	2.573
						2.516
S5	1.0	1.206	1.877	1.947	2.281	2.739
S6	6.5	ND	0.541	1.368	ND	ND
S7	6.5	ND	0.337	1.397	1.897	ND
N1	5.52	0.419	ND	1.810	1.999	2.633
N2	6.2	ND	1.425	1.727	2.003	2.850
N3	3.1	ND	1.601	1.888	2.942	ND

*Extensive surface contamination of specimen in the form of an oxide film.
ND = no data

(2) Pressure effect

It was previously mentioned that increasing the initial specimen temperature resulted in an increase in the initial H/Zr atom ratio differential for a constant pressure change. Decreasing the initial pressure had the same effect. Figure 17 illustrates the initial surface concentration (H/Zr atom ratio) differential for a one-atmosphere hydrogen pressure change as a function of the initial system pressure and specimen temperature. Thus, higher rates of absorption for lower initial system pressures could be expected. Table XI shows the experimental hydrogen absorption response for a hydrogen pressure change of one atmosphere as a function of initial hydrogen pressure and initial specimen temperature.

Figure 15. Hydrogen Absorption Response for Spherical ZrH as Function of Initial Specimen Temperature

Figure 16. Hydrogen Absorption Response for Nonspherical ZrH as Function of Initial Specimen Temperature

44
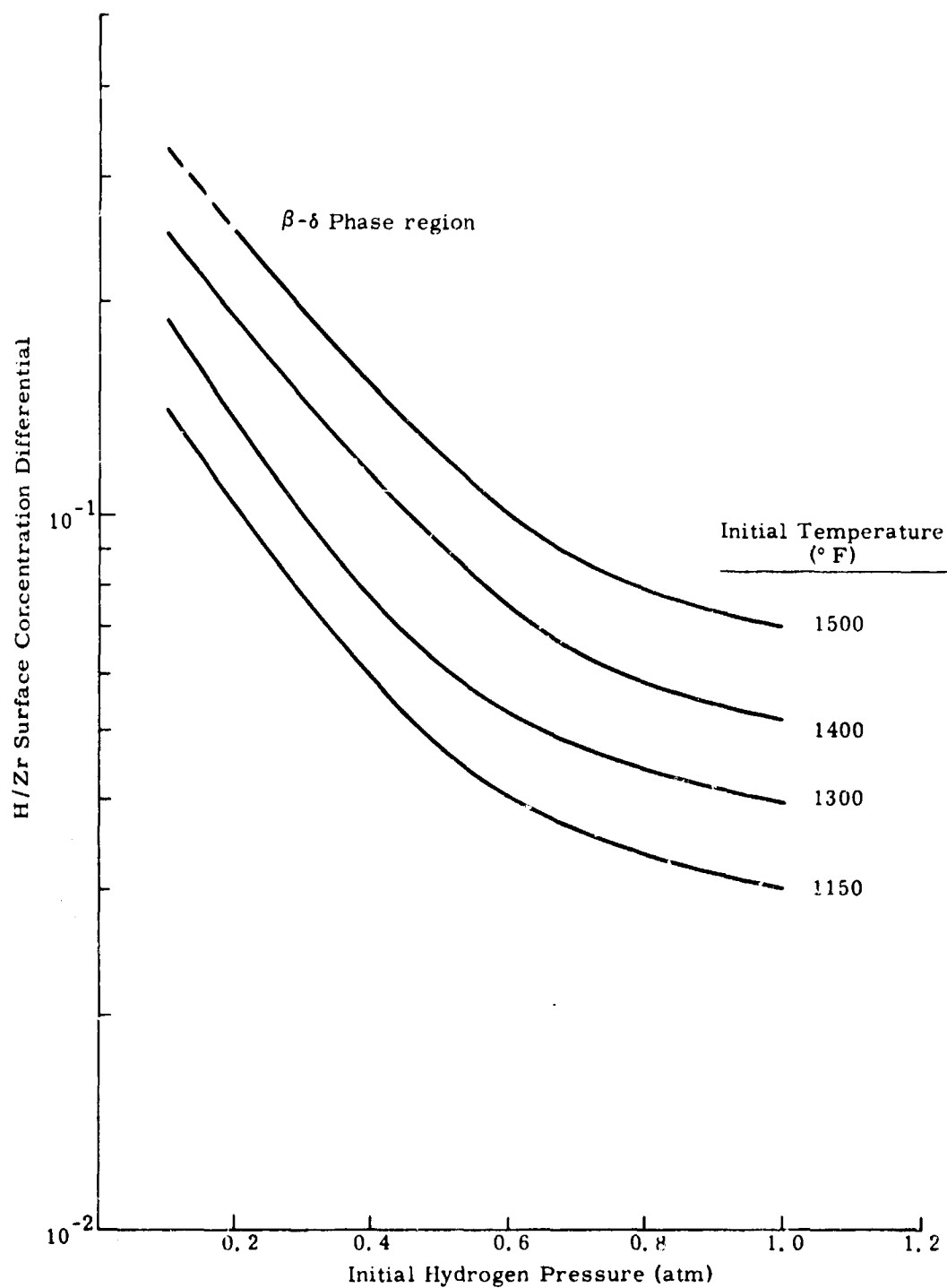
Figure 17. Surface Concentration (H/Zr Atom Ratio) Differential for One Atmosphere
Hydrogen Pressure Change as Function of Initial Pressure and Temperature

Table XI

HYDROGEN ABSORPTION RESPONSE FOR HYDROGEN PRESSURE
RAMP OF ONE ATMOSPHERE AS FUNCTION OF INITIAL HYDROGEN
PRESSURE AND INITIAL SPECIMEN TEMPERATURE

Specimen	Pressure ramp (atm)	Change in H/Zr Atom Ratio After 60 Seconds (%)				
		1000° F	1150° F	1300° F	1400° F	1500° F
S1	0.1 to 1.1	1.931	3.004	2.980	3.706	4.783*
	0.5 to 1.5	0.919	1.520	1.875	2.135	2.657
	1.0 to 2.0	ND	0.938	1.173	1.380	1.642
S2	0.1 to 1.1	ND	ND	3.126	4.579	5.037*
	0.5 to 1.5	ND	ND	2.083	2.715	3.540
	1.0 to 2.0	ND	ND	1.431	1.730	1.765

*ZrH specimen was initially in β phase and transformed to the δ phase by the end of the transient.

ND = no data

As expected, the transient with the highest initial specimen temperature and the lowest initial hydrogen pressure produced the largest change in hydrogen absorption. Figures 18 and 19 depict the percent change in hydrogen concentration versus time as a function of the initial specimen temperature and hydrogen pressure for a constant hydrogen pressure ramp change (one atmosphere).

(3) Particle size effect

Referring to table X, it is noted that decreasing the particle diameter of the ZrH specimen increases the absorption of hydrogen. However, as discussed in the section on temperature effects, the influence of the particle size effect diminished with increasing temperature (see figures 13 and 14). This results from the fact that the diffusion coefficient becomes sufficiently high that the rate at which hydrogen is absorbed depends on other processes.

The sphere has the lowest surface-to-volume ratio of all geometric figures. Thus, for a given solids volume, the nonspherical particle specimens should have a larger surface area. Because the hydrogen absorption phenomena is a strong function of the surface area, one would expect, body permeabilities being equal, that the nonspherical particle specimens would exhibit better hydrogen absorption characteristics when compared to the spherical particle specimens. Examination of the experimental data presented in table X shows that for approximately the same specimen properties and test conditions, the percent change in
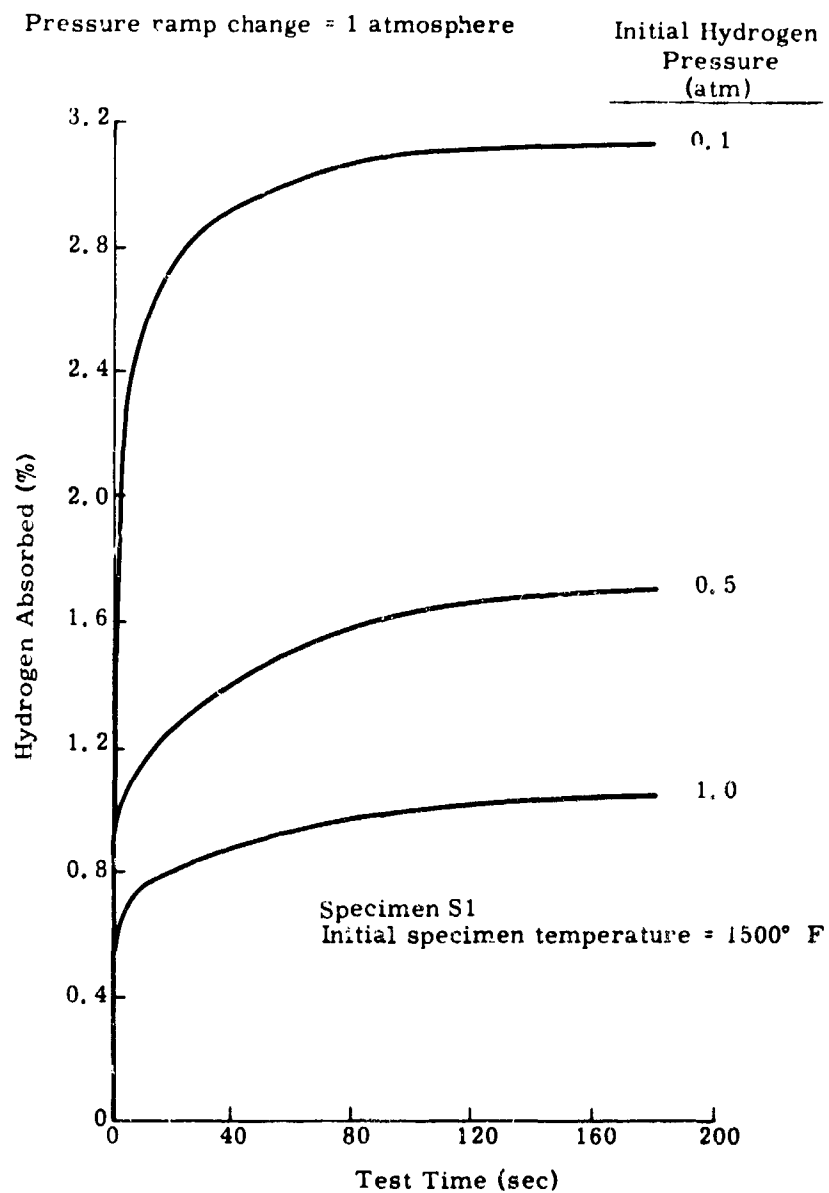
Figure 18.   Hydrogen Absorption Response for Spherical ZrH as Function of Initial Specimen Temperature and Hydrogen Pressure

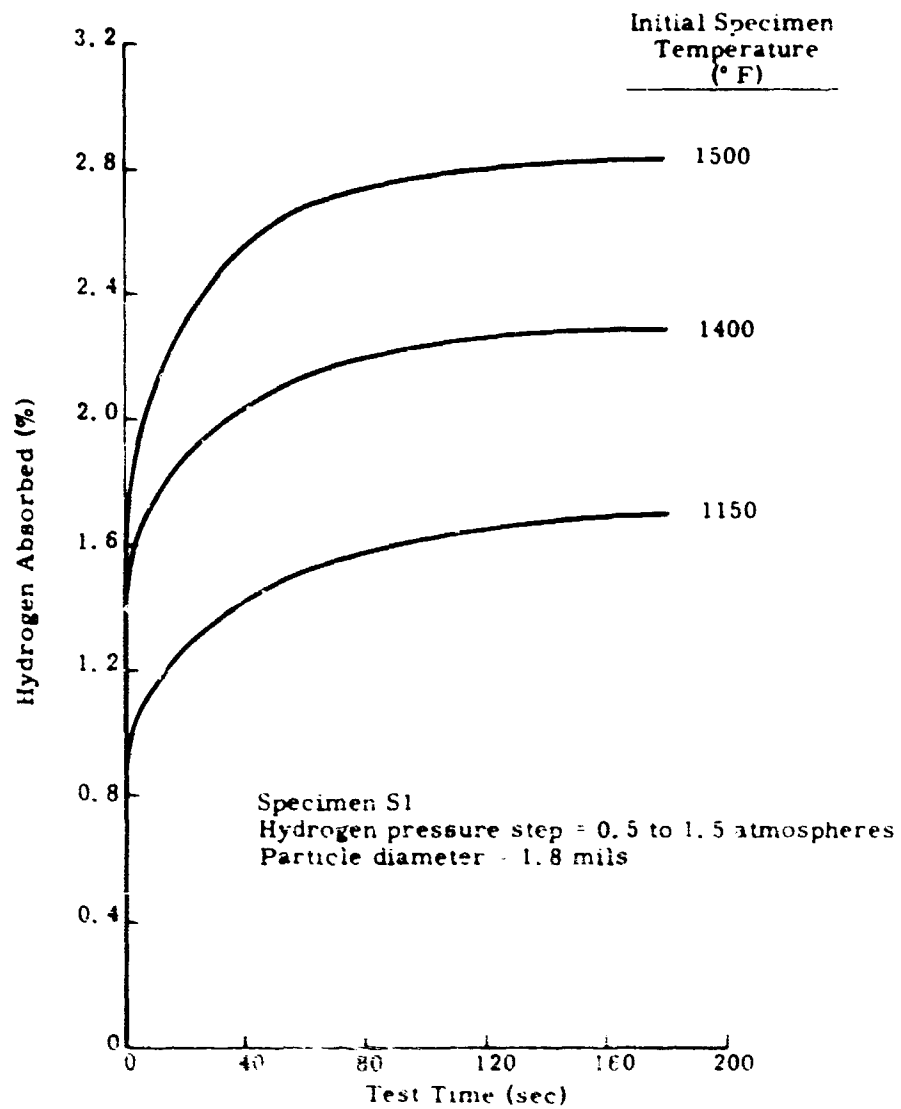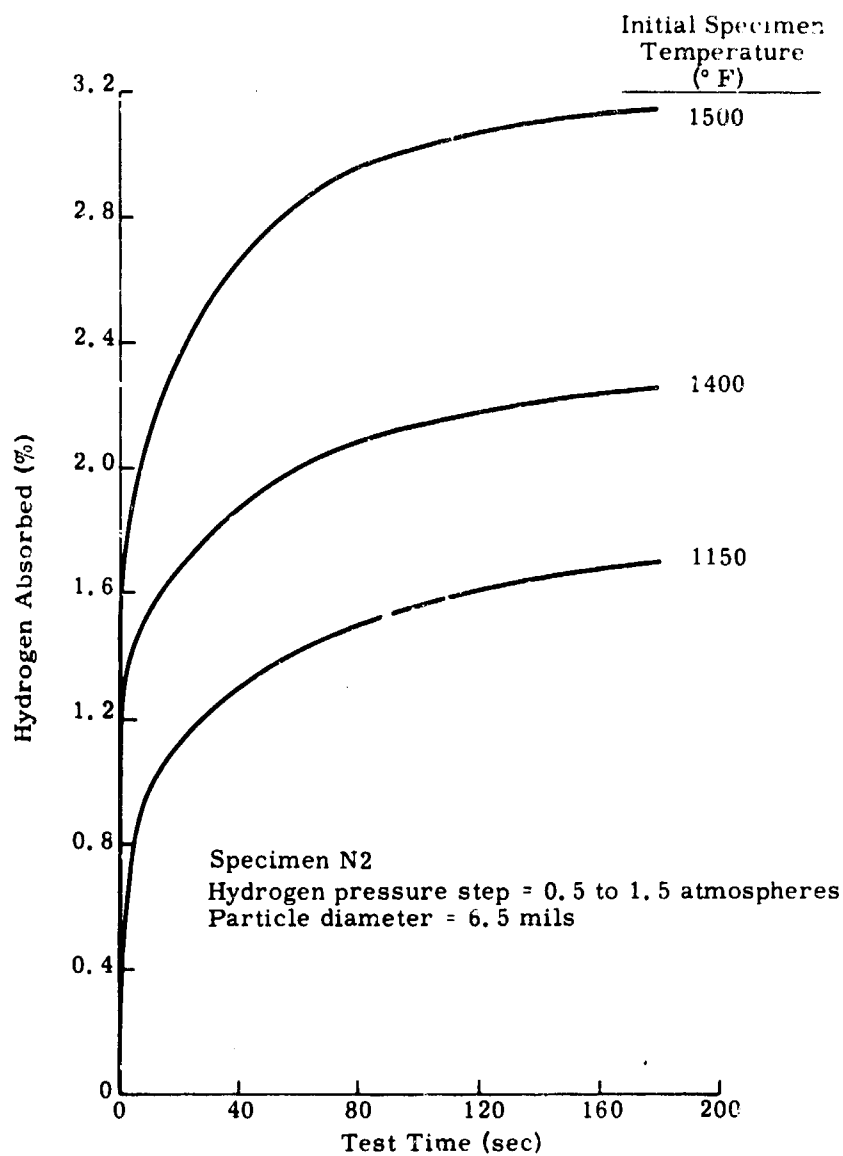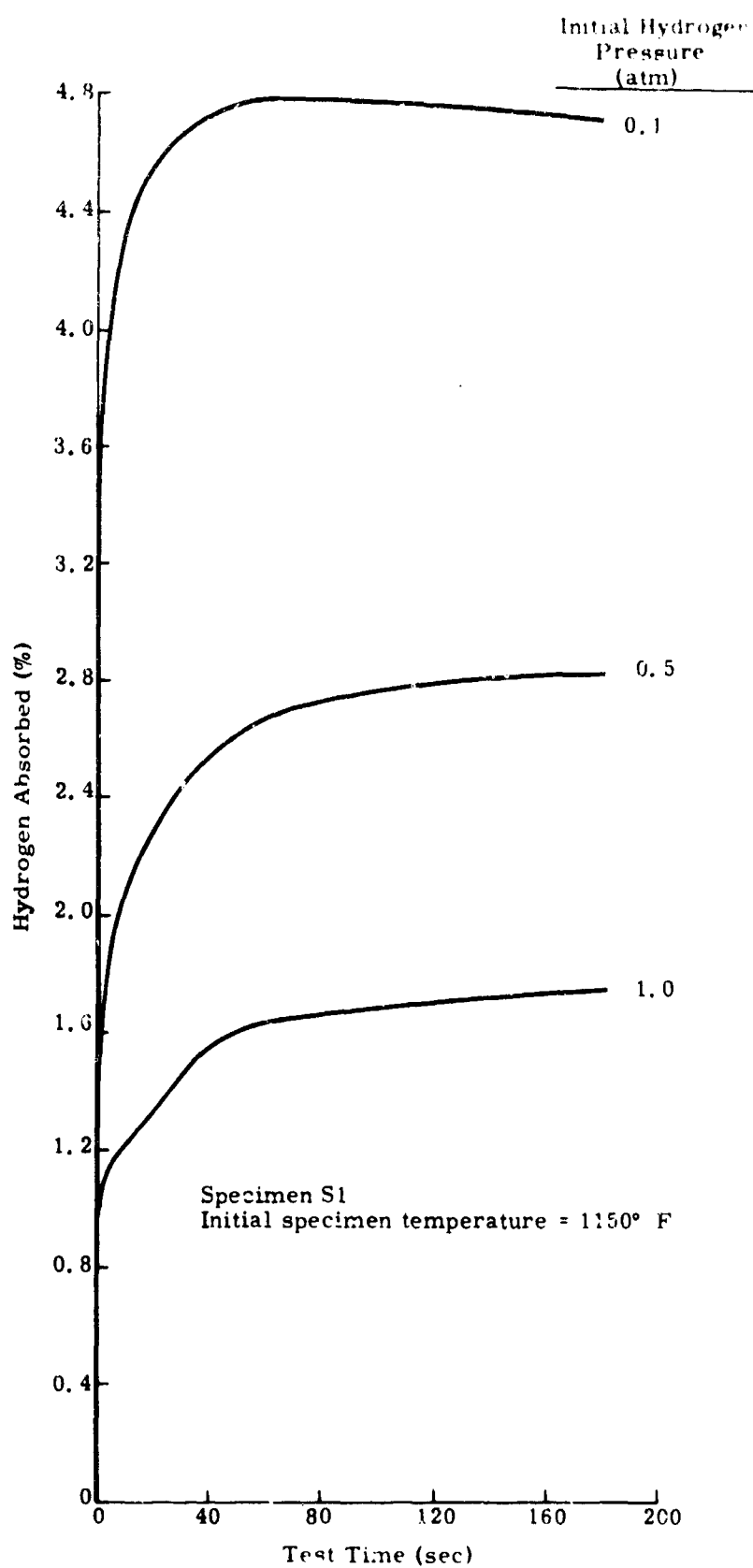Figure 19. Hydrogen Absorption Response for Spherical ZrH as Function of Initial Specimen Temperature and Hydrogen Pressure

hydrogen concentration is higher for the nonspherical particles. This is especially true at low temperatures where diffusion is more important. One can also conclude that the cold pressing and sintering operations have not caused extensive alteration of the individual characteristics of the powder particles.

(4) Inert gas effect

When an increase in system pressure occurs at the face of the specimen, the rate at which hydrogen will flow into the specimen is determined by the gas pressure gradient. In the case of the pure hydrogen gas transients, the absorption of hydrogen by the specimen results in a continual pressure gradient. When the pressure within the specimen is equal to the system pressure, no gas flow will occur and a new equilibrium is attained. This assumes that the specimen temperature is also in equilibrium with its surroundings.

When the increase in system pressure was from the addition of hydrogen and an inert gas, the initial response followed that of the pure hydrogen case. However, because the inert gas by definition did not react with the ZrH, no inert gas was absorbed. This resulted in a buildup of gas pressure within the specimen. When the pressure within the specimen, which was primarily inert gas, equaled the system pressure, the net gas flow into the specimen was essentially zero. However, because the void channels within the specimen contained a much higher percentage of inert gas constituent than was present in the system or at the face of the specimen, this concentration gradient resulted in a molecular diffusion of the constituent gases, such that the net flow of hydrogen was into the specimen while the net flow of inerts was out. Thus, a continual system pressure decay or hydrogen absorption was observed but at a much slower rate.

The experimental data for the inert gas test are given in table XII for varying test conditions and inert gas constituents.

Examination of table XII shows that the temperature, pressure and particle size effects are still evident. Superimposed upon these effects is that of the inert gas, which tends to suppress hydrogen absorption for the reasons stated. Referring to the krypton gas data, decreasing the initial inert gas fraction decreases the inert gas effect (see figure 20). The results illustrated in figure 20 are typical for almost all of the inert gas runs.

Table XII

INERT GAS TEST DATA

Specimen	Inert gas	Hydrogen pressure ramp (atm)	H/Zr atom ratio change after 60 seconds and initial inert gas fraction as functions of initial specimen temperature*		
			1300° F	1400° F	1500° F
S2	Argon	0.1 to 1.1	3.126% (0.0) 1.730% (0.038)	4.579% (0.0) 2.012% (0.038)	5.037% (0.0) 1.797% (0.037)
		0.5 to 1.5	2.083% (0.0) 1.386% (0.027)	2.715% (0.0) 1.752% (0.022)	3.540% (0.0) 2.009% (0.021)
		1.0 to 2.0	1.431% (0.0) 1.095% (0.12)	1.730% (0.0) 1.274% (0.012)	1.765% (0.0) 1.480% (0.012)
S1	Argon	0.1 to 1.1	2.980% (0.0) 1.843% (0.038)	3.706% (0.0) 1.920% (0.038)	4.783% (0.0) 2.080% (0.037)
		0.5 to 1.5	1.875% (0.0) 1.494% (0.021)	2.135% (0.0) 1.584% (0.021)	2.657% (0.0) 1.807% (0.020)
		1.0 to 2.0	1.173% (0.0) 1.296% (0.012)	1.380% (0.0) 1.435% (0.012)	1.642% (0.0) 1.739% (0.012)
S1	Krypton	0.5 to 1.5		1.854% (0.005) 1.695% (0.023) 1.681% (0.028) 1.041% (0.039)	
S1	Xenon	0.5 to 1.5		2.278% (0.007) 1.395% (0.027)	
		0.5 to 1.86		1.837% (0.042)	

*Numbers in parenthesis refer to initial inert gas fraction.
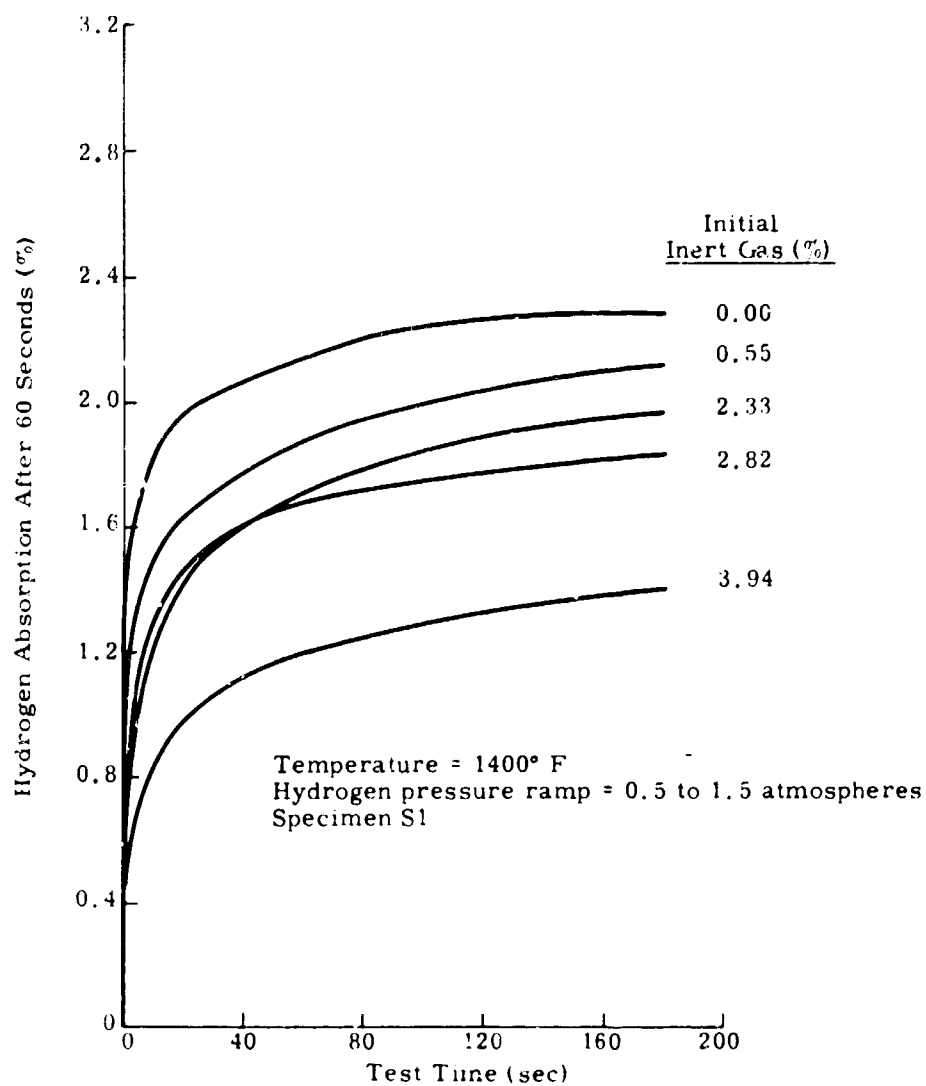
Figure 30. Effect of Inert Gas Upon Hydrogen Absorption Response (inert gas--krypton)

Hydrogen Absorption After 60 Seconds (%)

Test Time (sec)

Initial Inert Gas (%)

0.00
0.55
2.33
2.82
3.94

Temperature = 1400° F
Hydrogen pressure ramp = 0.5 to 1.5 atmospheres
Specimen S1

(1) HYDRA II vs experimental data

Of major concern in the preparation of HYDRA II was the validity of the mass transport model. As such, the diffusion and flow equations are elaborately developed while the heat transfer equations are included in a rather simple lumped model. One would, therefore, expect HYDRA II to most accurately describe the transport process in those cases where heat transfer effects are not controlling. In other cases, it was clear that a more accurate description of the specimen temperature distribution was necessary to improve the analytical predictions. Such was found to be the case in the present study.

The input parameters which most heavily influence the prediction of hydrogen absorption were:

d permeability of the body

f_D shape factor for diffusion

L heat loss term

ρC_p volumetric heat capacity

The value of d was taken directly from the results of the permeability tests. The other values were varied within their probable range to obtain best agreement with the data. The effect of each is discussed in the following paragraphs.

(1) The particle diffusion shape factor (f_D): The inverse of the shape factor was employed in the mass diffusion rate equation. Thus, decreasing its value increased the rate of hydrogen absorption or the initial slope of the percent hydrogen absorbed versus test time curve. However, a point was reached where decreasing the shape factor no longer affects the absorption rate. At this point, diffusion was essentially instantaneous and the absorption rate was controlled by thermal effects. In a perfectly insulated container, the absorption curve would be flat (slope = 0) after a few seconds because the absorption process continues only if a specimen heat loss exists.

(2) The heat loss factor (L): The value of the system heat loss term controls the rate at which the specimen exchanges heat with its environment. Thus, its effect was prevalent throughout the transient. In the present version of HYDRA II, the heat loss was taken as proportional to the temperature differential between the average specimen temperature and the ambient temperature which was assumed to be the initial specimen value. Estimates of the proportionality have been made. The primary mode of system heat loss was thought to be across the hydrogen gap between the specimen and the retort wall. As a result, the heat loss factor was expected to be on the order of the hydrogen conductivity value (approximately 10^{-3} cal/cm-sec-°C).

(3) Specimen specific heat $(\rho C)_s$: The specimen specific heat controlled the average temperature of the specimen for a given rate of heat addition or loss. Thus, its value, along with the system heat loss, determined the point in the transient where the absorption curve leveled out (slope ≈ 0). In the current version of HYDRA II, the value for the specific heat is a constant input parameter. In reality, the specific heat of zirconium hydride is a function of temperature and H/Zr atom ratio. Thus, the specific heat is more accurately taken as a time variant function.

By proper selection of these parameters, it is possible to obtain a fair agreement between HYDRA II and the experimental data (see figures 21 and 22). In general, HYDRA II followed the transients controlled by the diffusion process such as those run at 1150° F or with large particle sizes quite well. Where rates were dominated by heat transfer considerations, the success of the model was less dramatic, as shown by the results obtained with small particle sizes at 1300° or 1400° F.

The digital code has been converted to run on the IBM 360 Model 65 system which has a faster running time and larger storage capacity than the IBM 7094. The average computing time for a 60-second transient is approximately 20 minutes. The more severe a transient, the longer the running time. This results from the fact that for a transient in which the system parameters (pressure and temperature) are continually varying, all of the time history terms in the diffusion equation significantly affect the absorption rate and must be evaluated at every time step.

Efforts to reproduce the experimental results obtained with the inert gas were not completely successful. The code predicts much slower absorption rates and faster inert gas pressure buildup in the specimen voids than were experienced in the experiment. In general, predicted hydrogen absorption was about one-half of that observed. The mathematical model used does not account for these possibly significant processes:

(1) Adsorption of the inert gas by the porous body

(2) Molecular diffusion of the inert gas from the body

(3) Separation of the gas mixture during the flow process.

These and other causes can be checked analytically and experimentally and should the inert content of the TURPS fuel element gas space prove to be large,
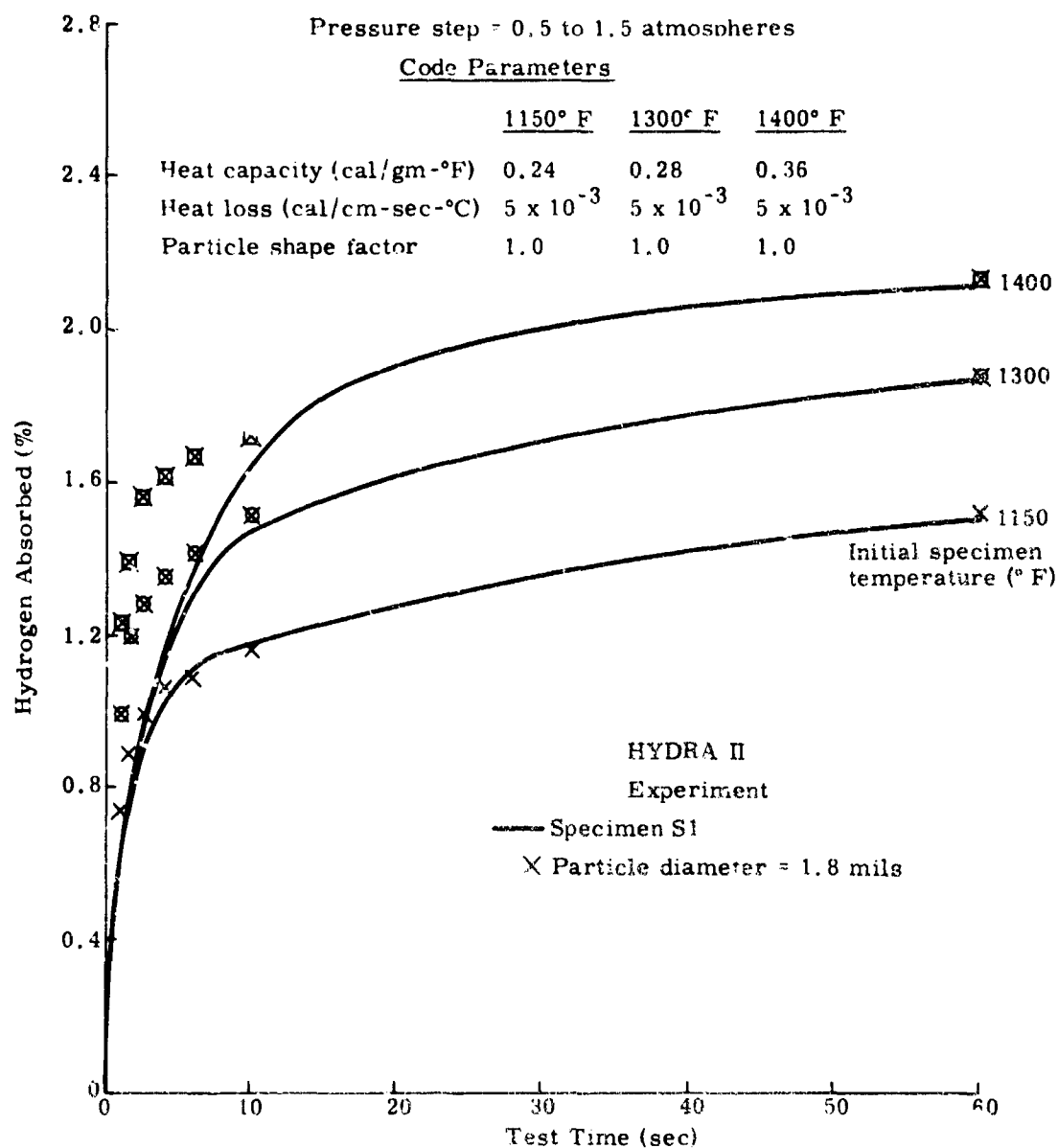
Figure 21. Hydrogen Absorption Response for Spherical ZrH_x
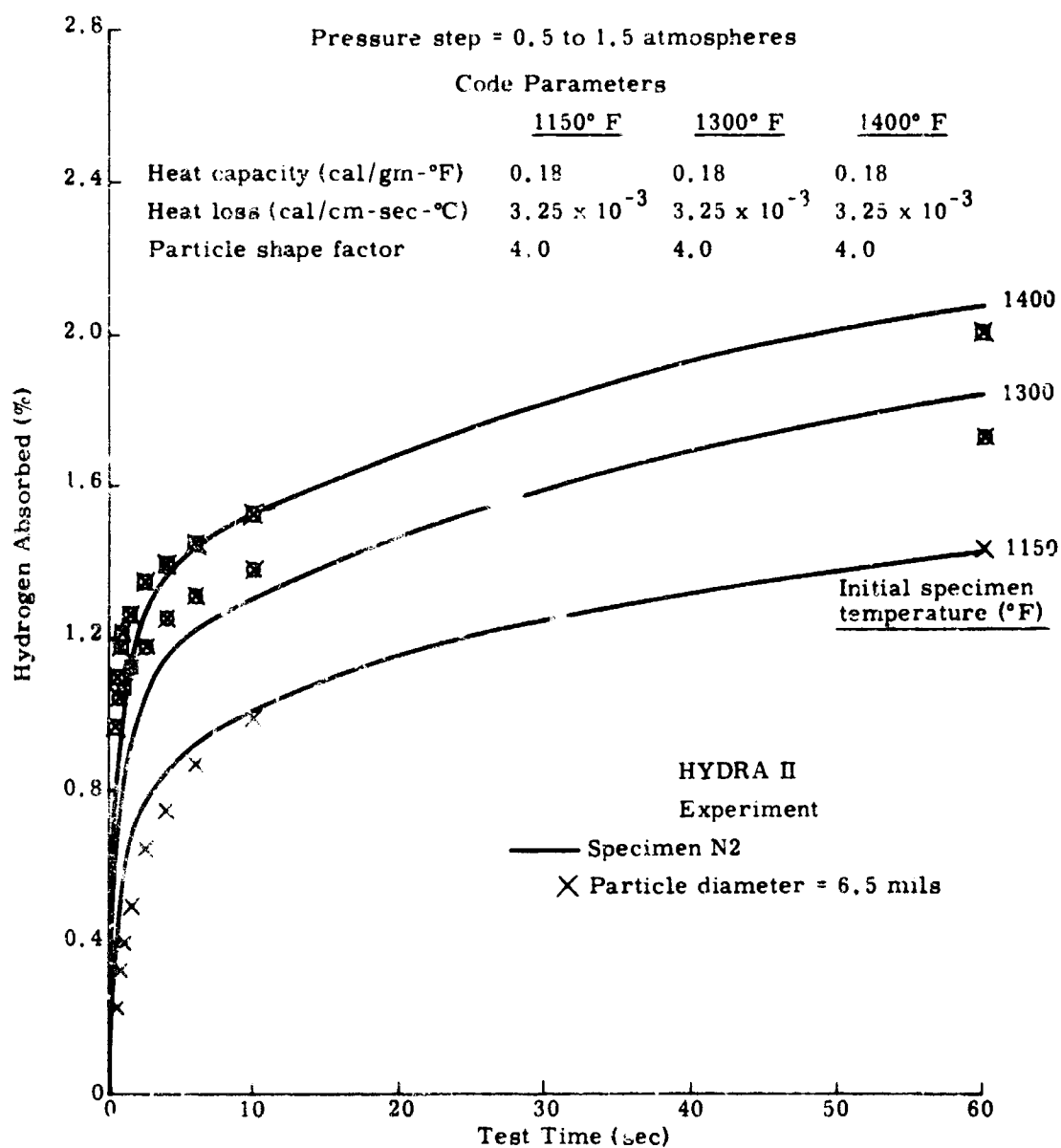
Figure 22. Hydrogen Absorption Response for Nonspherical ZrH_x

such action should be pursued. Section III is a discussion of gaseous fission product release.

c. Thermal Cycling Test

The thermal cycling test data are presented in table XIII. The minimum and maximum points for the system parameters are given for a typical cycle in the test history. A trace of the variation of the system parameters during these typical cycles is shown in figure 23.

The permeation rate of hydrogen through a metal is quite significant at the thermal cycling temperature (approximately 5 cm^3 (STP)/cm^2/hr/mil at 760 mm H_g). Thus, a hydrogen loss and the resulting continual hydrogen pressure decrease throughout the course of the test was observed. It was also noted that setting the retort heater power too high resulted in the override of the temperature controller set points. Both of these caused a variance in the retort hydrogen pressure and the shape of the system parameter trace (see figure 24). Referring to figure 24, it was observed that the leakage of hydrogen from the retort lowered the hydrogen pressure to the point where the specimen (S6) was cycled through the β-δ phase equilibrium.

Visual examination of the specimens at the conclusion of the thermal cycling test revealed no change in appearance. As previously discussed. there was no discernible difference in the permeability values. The only difference noted was that for Specimen N3, the hydrogen absorption rates for the 1300° and 1150° F initial specimen temperature runs were higher for the pretest condition. Examination of the rates at 1400° F revealed no change between the pre- and post-test results. The cause may well have been an increase in specimen contamination during the long cycling run. Such an effect would be most evident at low temperature.

d. Effect of Testing on Bodies

As previously mentioned, the porous bodies were prepared by cold pressing and sintering. They were then placed in a stainless steel capsule and hydrided. The density change on hydriding provided a very tight expansion fit. Figure 25 shows a typical body prior to testing. The small pitted areas were caused during handling of the green (unsintered) body and have no effect on the results. Figures 26 and 27 show the tightness of the fit for a typical cross section. The maximum and minimum gaps are shown.

Table XIII

THERMAL CYCLING TEST DATA

| Specimen | Cycle Data | | Hydrogen Pressure | | Temperature | | H/Zr Atom Ratio | |
	Total Number	Time (hr)	Minimum (psia)	Maximum (psia)	Minimum (°F)	Maximum (°F)	Minimum	Maximum
N3 (1)	300	191	7.75	14.15	1183	1390	1.687	1.81
S7 (2)	405	256	3.40	9.80	1154	1380	1.670	1.793
S6 (3)	405	256	0.6	4.90	1250	1450	1.520	1.580
S6 (4)			0.2	4.80	1225	1450	β phase	1.537

(1) Minimum and maximum points presented for 72nd cycle

(2) Minimum and maximum points presented for 294th cycle

(3) Minimum and maximum points presented for 294th cycle

(4) Minimum and maximum points presented for 405th cycle

57
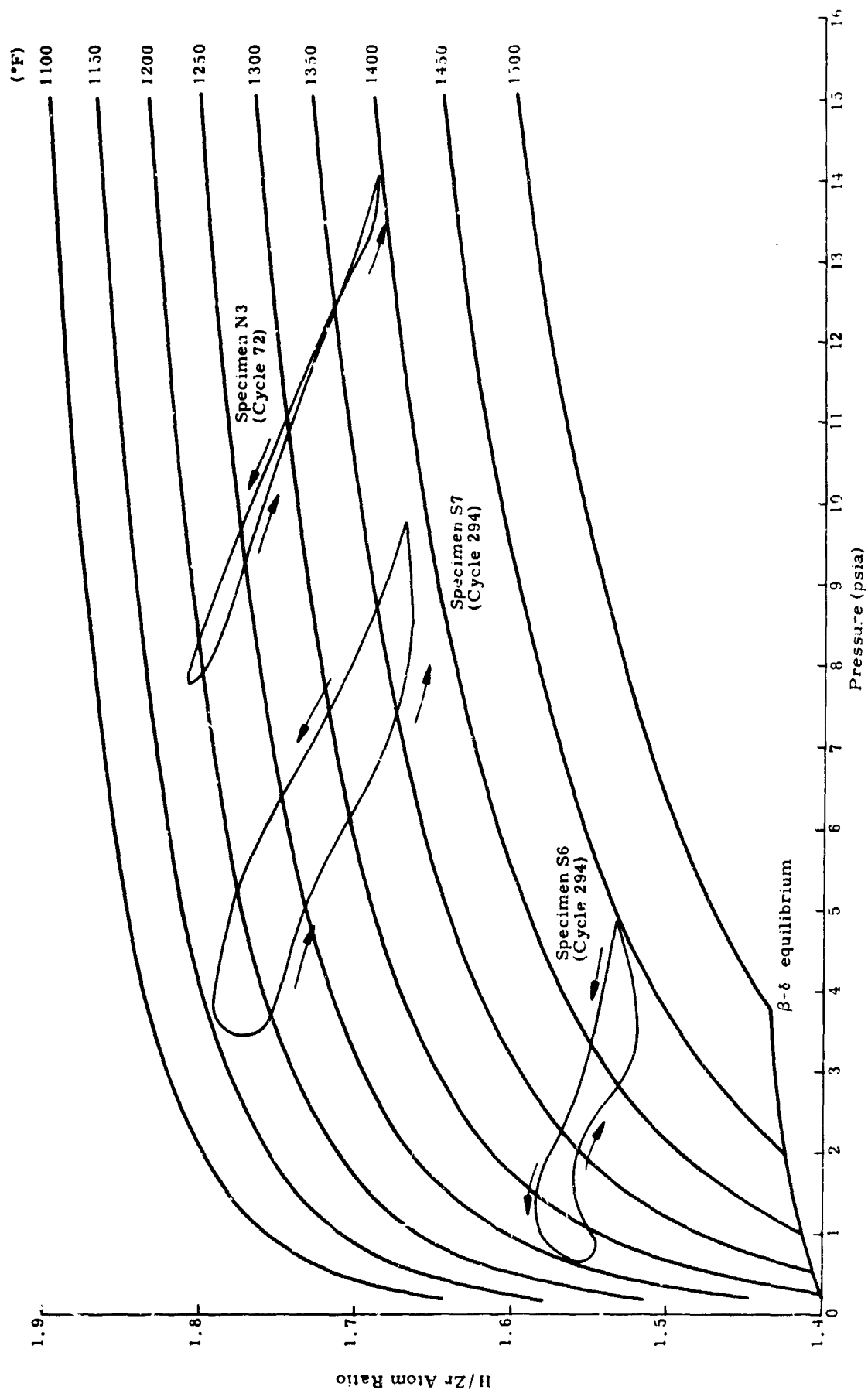
Figure 23. Thermal Cycle Test
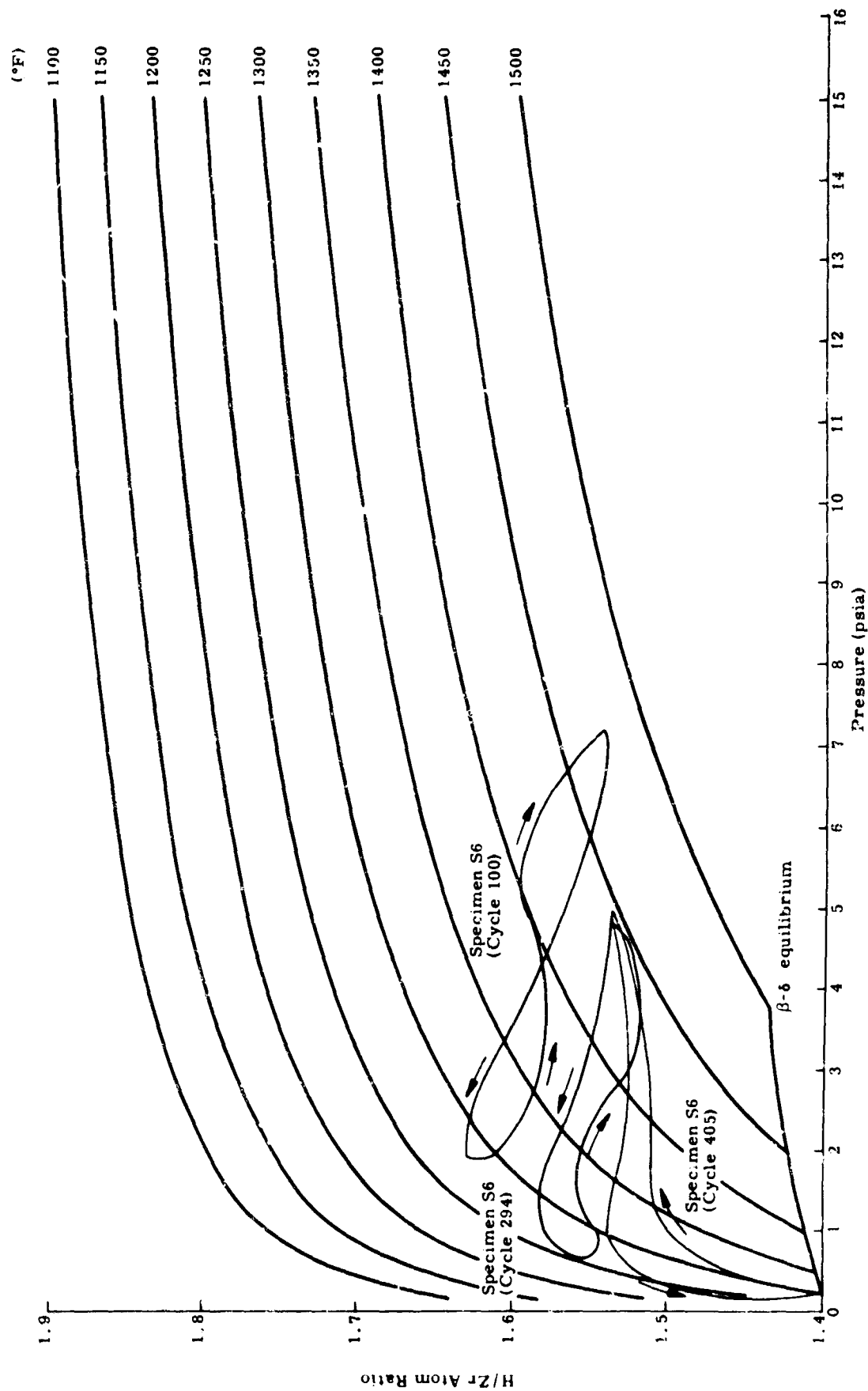
Figure 24. Thermal Cycle Test

Figure 25. Typical Body Prior to Testing (Sample S4)
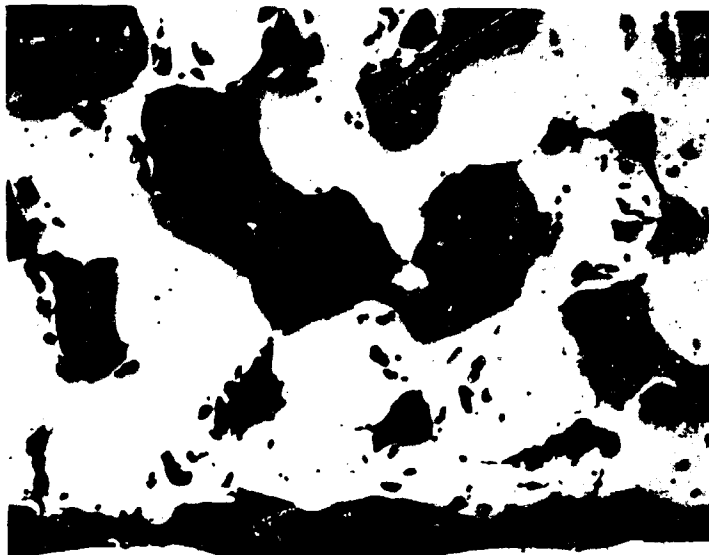
Figure 26. Maximum Gap Between Hydrided Body and SS 304 Tube
(Gap = 0.0012 inch, Sample S4, Magnification 200 X)

Figure 27. Minimum Gap Between Hydrided Body and SS 304 Tube
(Gap = 0.0004 inch, Sample S4, Magnification 200 X)

60

Following absorption testing, the bodies were inspected for cracking and other effects. Most of the nonuranium-containing bodies showed no effect. Three such bodies are shown in figure 28. Some showed surface contamination apparently from oxygen inadvertently introduced into the system. Even these were intact and showed only the surface cracks and imperfections that were noted prior to testing (figure 29).

Those bodies which were thermal-hydrogen cycled for 300 to 400 cycles appeared free from physical damage. A typical body is shown in figure 30. There was no visible spallation and no measurable loss of material from these bodies.

8. Conclusions and Recommendations

The following conclusions and recommendations are made:

(1) Within the limits of experimental error, the hydrogen absorption testing and thermal-hydrogen cycling had no effect on the permeabilities of the bodies. It is concluded, therefore, that the basic pore size and structure were unaffected by these tests.

(2) The permeability measurements show that previous application of the Ergun correlation to sintered bodies gave conservative values in that predicted values were found to be lower than experimental values. Shape factors for bodies formed from sintered spheres indicate the behavior is very close to that of loosely packed spheres. It is, however, recommended that the permeability of all future porous bodies be experimentally determined to minimize analytic uncertainties. This appears necessary because of the wide variations that can be introduced by varying the pressing and sintering condition.

(3) The permeability of the porous bodies was found to be independent of the gas used or its pressure in the range investigated. Flow through the bodies was laminar and obeyed Darcy's law.

(4) Expected temperature, pressure and body characteristic effects were observed in the hydrogen absorption tests. Because of sharply increasing diffusion coefficients, absorption rates were found to increase rapidly with temperature. Varying the initial pressure of the transient resulted in changing the initial driving function (concentration change). The available concentration change increases as the initial pressure is lowered, thus resulting in a higher rate of absorption.
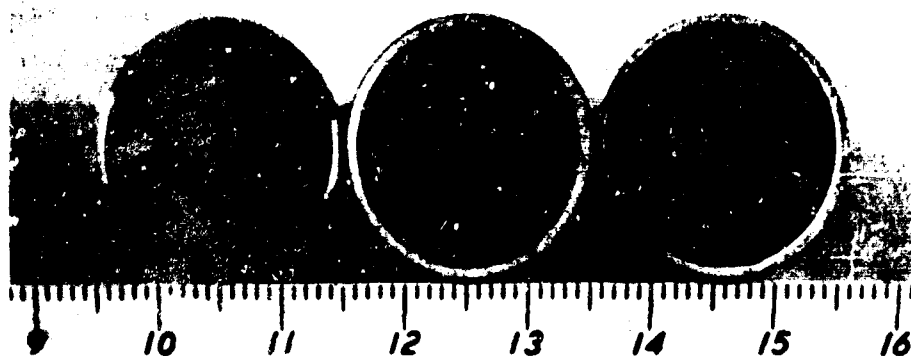
Figure 28. Typical Body Appearance After Absorption Testing
with No Surface Contamination
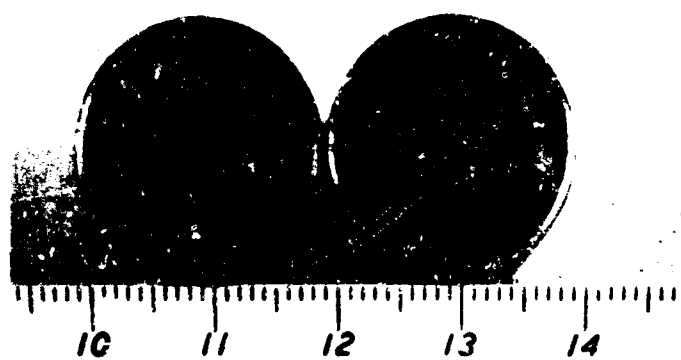
Figure 29. Typical Body Appearance After Absorption Testing
with Severe Surface Contamination
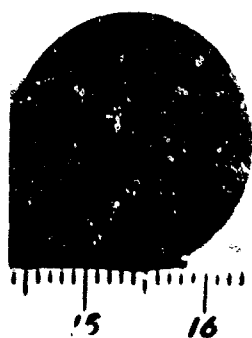
Figure 30. Typical Body Appearance After 405 Thermal Cycling
and Absorption Testing

The inert gas results exhibited higher absorption rates than anticipated, although the net effect of the inerts was to reduce the hydrogen absorption, at least in the short-term transient. There appeared to be no basic difference between the various gases used, i.e., argon, krypton and xenon.

(5) Good analytical agreement with the absorption experiments was obtained where the absorption rate was controlled by transport processes. Poorer agreement was obtained in those cases where heat transfer processes were rate controlling. Such results are understandable in light of the rather simple lumped heat transfer model being used. The results confirm the validity of the mass transport model. A more complete thermal model should be used in future TURPS analysis where appropriate.

(6) With the exception of some surface contamination on a few of the samples, the testing had no effect on the physical appearance of the porous bodies. This included bodies that were thermal-hydrogen cycled for up to 105 cycles. No physical damage of any kind was attributed to the testing.

This page intentionally left blank.

SECTION III

THERMAL CONDUCTIVITY OF POROUS ZIRCONIUM HYDRIDE

1. Purpose

The thermal conductivity of the porous fuel body and reservoir matrix of TURPS is an important system characteristic. Because maximum fuel temperatures are major design constraints, it is important to have accurate knowledge of thermal conductivity to enable optimum design. Prior to this investigation, the Bruggeman variable dispersion model for porous matrices was used. From this model, knowledge of the solid material and gas conductivities yields a prediction of the matrix conductivity in the following equation:

$$\frac{k_1 - k_m}{k_1 - k_2} \left(\frac{k_2}{k_m}\right)^{1/3} = \epsilon$$

where the subscripts 1, 2 and m refer to the solid, gas and composite matrix, respectively, and ϵ is the void or gas volume fraction. The objective of this study was to test the validity of this model for TURPS sintered matrix material and to provide empirical data for reactor design use.

The technique chosen for evaluation of thermal conductivity was the flash method (reference 1) of obtaining thermal diffusivity together with separate evaluation of specific heat. This method provided a means of avoiding troublesome heat loss considerations encountered in conventional steady-state methods and elimination of gross hydrogen concentration gradients from impressed temperature gradients.

It was recognized, however, that the thermal diffusivity measurements might be impaired by hydrogen dissociation upon impingement of the heat source (light flash) and therefore the experiments were conducted in two stages. The first stage used unhydrided, sintered zirconium bodies composed of differing spherical particle size distribution to yield a range of matrix densities. Also, the void space was varied to contain argon, helium and vacuum to enable determination of the gas contribution to thermal conductivity. The second stage used hydrided, sintered zirconium bodies in which the effects of vacuum and argon gas presence in the void could be examined up to 650° F, a temperature range in which the hydrogen dissociation pressure is negligible. Following this, a hydrogen atmosphere was introduced to investigate the behavior of the hydride material at higher temperatures.

The thermal diffusivity is related to thermal conductivity, specific heat and density by the following equation:

$$\alpha \text{ (thermal diffusivity)} = \frac{k}{\rho C_p}$$

where:

k = thermal conductivity

ρ = density

C_p = specific heat

In this investigation, the thermal diffusivity was obtained from the time required for a temperature pulse to reach one-half of its maximum value (asymptotic maximum in a perfectly insulated body) at the rear surface of a slab whose front surface receives an impulse of radiant energy. According to Parker (reference 1), if the energy pulse duration is short compared to the temperature rise time, and if heat losses are negligible, the following relationship is applicable:

$$\alpha = \frac{1.37 \, L^2}{\pi^2 T_{1/2}}$$

where L is the slab thickness and $T_{1/2}$ is the time for the temperature to reach one-half of its maximum rear surface value.

2. Experiment Description

All samples tested were made of sintered, spherical zirconium particles. The particle size distributions used and the dimensions of each specimen are given in table XIV. The densities of both hydrided and unhydrided bodies were calculated from the post-sintering dimensions and weight (before hydriding). It is of interest to note that although the sintering was done at two conditions, 900° C for two hours and 1100° C for four hours, only those bodies sintered at the latter condition possessed suitable strength for handling during the diffusivity measurements.

After unsuccessful attempts at using pressure contact for the chromel-alumel thermocouple against the rear surface of the test specimens, a spot welding technique was developed. Because of the porous nature of the surfaces, spot welding was difficult, particularly for the hydride material. Furthermore, it was found essential to weld each wire separately to the surface so that a bead-induced temperature lag would be avoided. It was during the spot welding development that the 900° C sintered bodies were deemed not suitable for testing. Interparticle adherence was insufficient to allow a suitably strong bond between the thermocouple wires and the surface.

Corrections for heat loss from the test specimens were made according to a one-dimensional heat transfer model (references 1 and 2). Because the heat loss was nearly equal for specimens tested in vacuum and in argon or helium atmospheres, it was concluded that the main path was conduction to the insulator and the thermocouple wire holders pressed against the rear surface of the pellet. The effect was small, however, causing only about a four percent decrease in the observed response time.

The accuracy and reliability of this thermal conductivity determination method was estimated by comparison with a known material (Zircaloy-2 specimen) and by checking the reproducibility of measurements. Reproducibility differences of less than five percent and Zircaloy-2 results, in agreement within 10 percent of accepted literature values, indicate an overall accuracy of about 10 percent.

3. Results

a. Unhydrided Zirconium

A summary of the porous zirconium body test results is presented in table XV. The measured thermal diffusivities at various temperatures for vacuum, argon and helium gas presence are listed for each specimen studied. The values of thermal conductivity were derived with the aid of zirconium heat capacity data of figure 31. Figure 32 contains gas conductivities for use in the analytical prediction of porous body thermal conductivity by the Bruggeman model.

The experimentally determined thermal conductivities for 76, 78, and 80 percent density zirconium matrices are presented graphically in figure 33 together with analytic predictions with helium and argon gas environments (one atmosphere pressure). Also included is a best literature result for pure solid (100 percent dense) zirconium. It is apparent that the analytic model grossly underestimates the absolute value of matrix conductivity, while overestimating the gas effect. This failure is readily understandable in that the model assumes point contact of spherical particles whereas photomicrographs of the porous bodies show a clear connection between the particles. The effectiveness of this particle interconnection is illustrated by the high values of conductivity in vacuum environment.

The observed sensitivity of thermal conductivity with body void fraction (or density) is shown in figure 34. It should be noted that the gross parameter

(void fraction) is dependent upon the particle size distribution and the sintering
process used in specimen fabrication. Therefore, this graph should be inter-
preted cautiously until further study of microscopic structure effects is per-
formed.

Table XIV

SPECIMEN FABRICATION DATA

Specimen number	Composition (particle grading)	Length (in.)	Diameter (in.)	Weight (gm)	Density %	X
	Unhydrided Zirconium					
6-9	70%, -170 +270 Mesh 20%, -80 +270 Mesh 10%, -400 Mesh	0.071	0.481	1.0482	76.2	—
6-7	70%, -400 Mesh 30%, -230 +325 Mesh	0.072	0.470	1.0388	78.1	—
3-7	80%, -170 +270 Mesh 20%, -400 Mesh	0.074	0.494	1.0863	72.0	—
3-5	100%, -400 Mesh	0.065	0.479	0.9975	80.0	—
	Hydrided Zirconium ZrH$_x$					
6-3	75%, -100 +120 Mesh 25%, -80 +270 Mesh	0.056	0.493	0.8316	73.1	1.59
6-8	70%, -400 Mesh 30%, -230 +325 Mesh	0.047	0.471	0.6850	78.6	1.59
6-10	70%, -170 +270 Mesh 20%, -230 +325 Mesh 10%, -400 Mesh	0.071	0.480	1.1100	79.2	1.78
3-6	100%, -400 Mesh	0.070	0.479	1.0732	79.7	1.59
3-8	80%, -170 +270 Mesh 20%, -400 Mesh	0.074	0.494	1.0863	72.4	1.78

Table XV

EXPERIMENTAL RESULTS

Temperature (°F)	Gas	α (cm^2/sec)	k (Btu/hr-ft-°F)
Specimen 6-9; ρ = 76.4 percent			
70	Vacuum	0.044	3.5
330	Vacuum	0.045	3.9
730	Vacuum	0.044	4.2
1080	Vacuum	0.045	4.4
70	Argon	0.046	3.6
300	Argon	0.045	3.9
710	Argon	0.045	4.2
70	Helium	0.049	3.8
250	Helium	0.049	4.2
600	Helium	0.048	4.4
1040	Helium	0.049	4.8
Specimen 6-7; ρ = 78.1 percent			
70	Vacuum	0.058	4.7
350	Vacuum	0.058	5.2
690	Vacuum	0.054	5.2
1112	Vacuum	0.054	5.5
70	Argon	0.058	4.7
325	Argon	0.056	5.1
660	Argon	0.054	5.2
1100	Argon	0.057	5.7
70	Helium	0.061	5.0
250	Helium	0.059	5.2
450	Helium	0.058	5.4
900	Helium	0.058	5.7

Table XV (cont'd)

Temperature (° F)	Gas	(cm^2/sec)	k (But/hr-ft-° F)
Specimen 3-7; ρ = 72 percent			
70	Vacuum	0.051	3.8
350	Vacuum	0.047	4.0
710	Vacuum	0.045	4.0
1050	Vacuum	0.046	4.2
70	Argon	0.051	3.8
300	Argon	0.048	3.9
680	Argon	0.047	4.2
1010	Argon	0.046	4.2
70	Helium	0.052	3.9
300	Helium	0.050	4.1
550	Helium	0.051	4.5
900	Helium	0.050	4.5
Specimen 3-5; ρ = 80 percent			
70	Vacuum	0.061	6.3
275	Vacuum	0.064	7.2
700	Vacuum	0.059	7.3
70	Argon	0.064	6.6
300	Argon	0.062	7.1
660	Argon	0.058	7.1
70	Helium	0.065	6.7
190	Helium	0.066	7.3
460	Helium	0.059	7.0

b. Hydrided Zirconium

The diffusivity measurement results and the derived values of thermal con-
ductivity for the hydrided porous zirconium matrix specimens are contained in
table XVI. The heat capacity data of Beck as presented in AFWL-TR-66-16 and
reproduced in figure 35 was verified over a limited range of temperatures by
calorimetry measurements on specimens of zirconium hydride prepared simul-
taneously with the diffusivity test bodies.
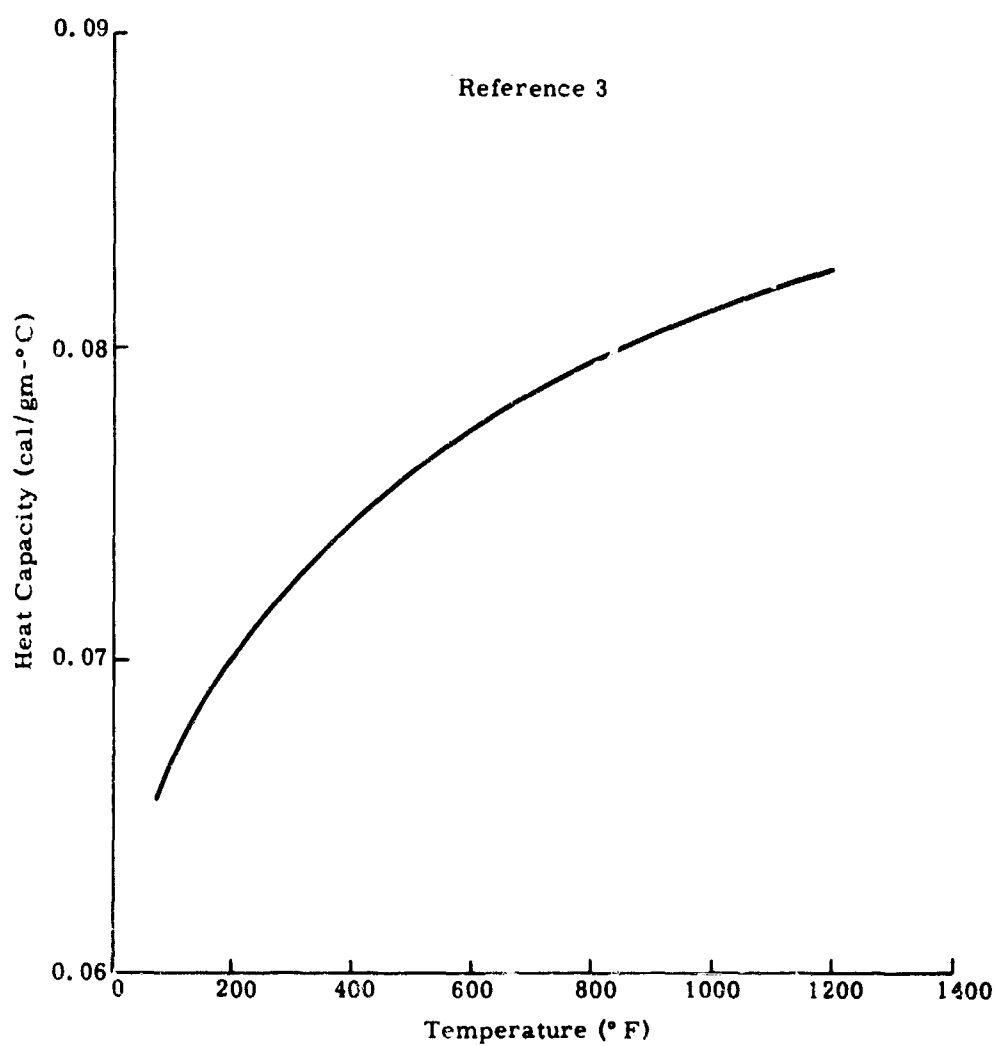
Figure 31. Heat Capacity of Zirconium
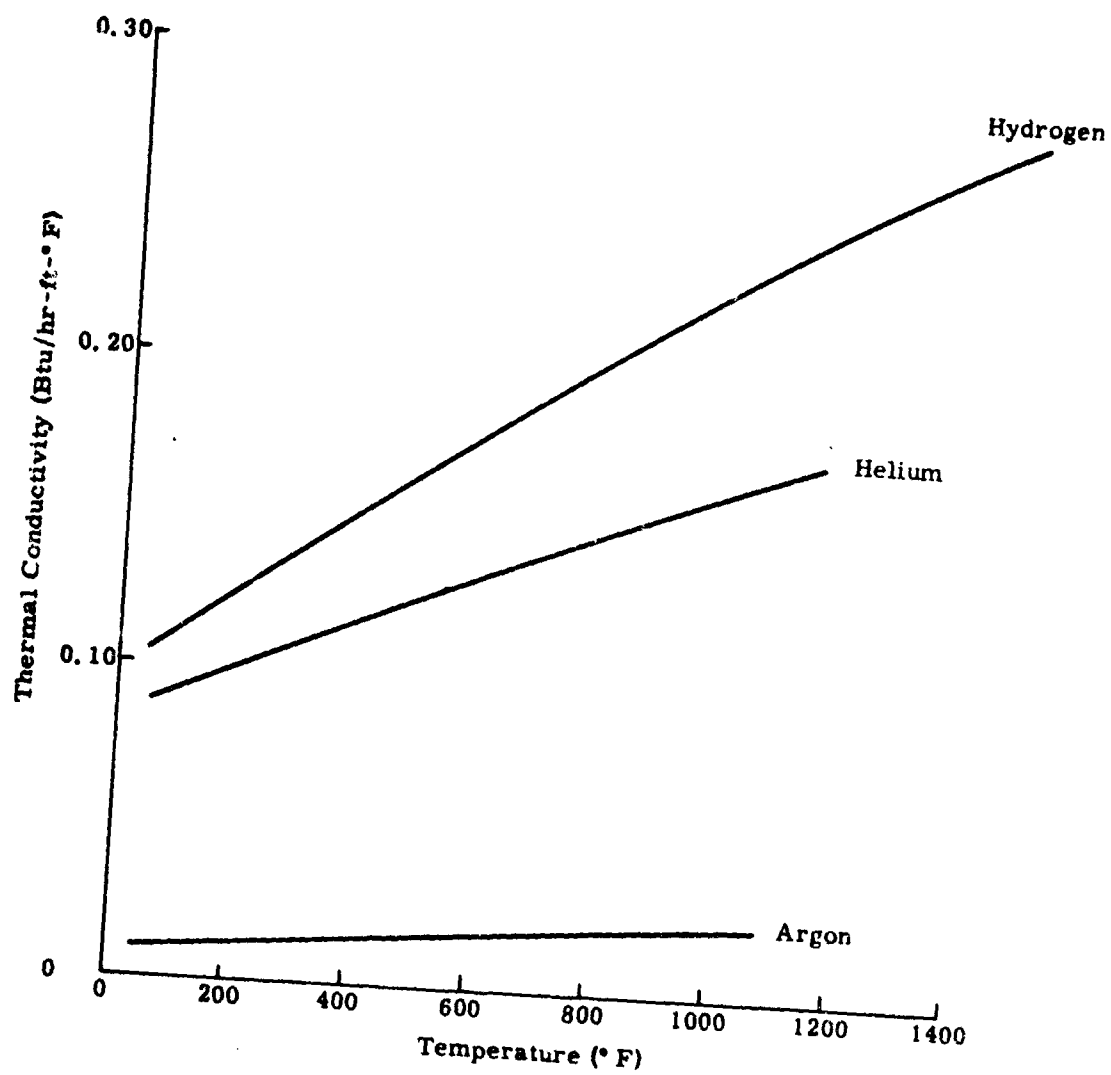
Figure 32. Thermal Conductivities of Hydrogen, Helium and Argon (references 5, 6)
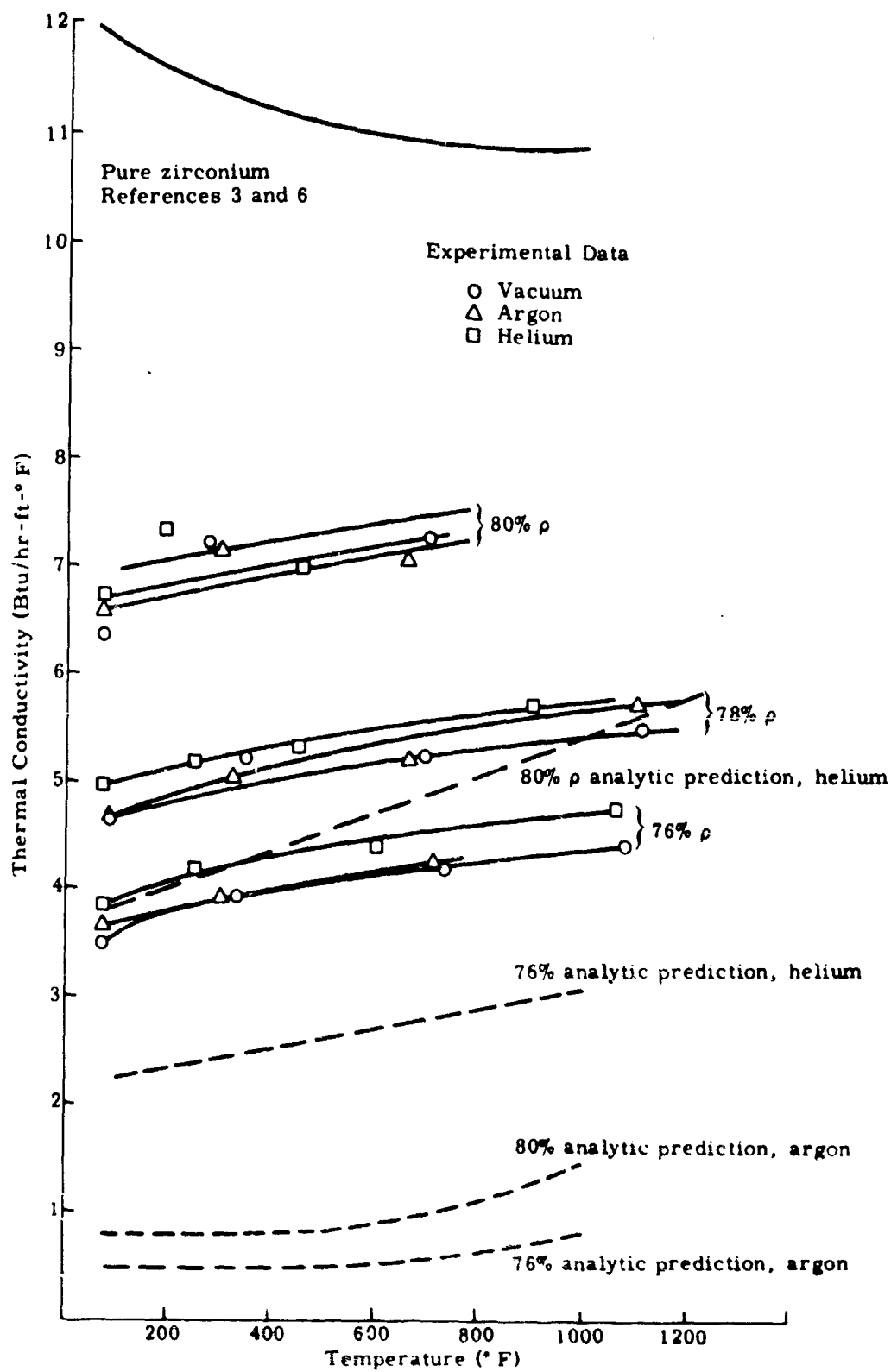
Figure 33. Conductivity of Porous Sintered Zirconium Bodies
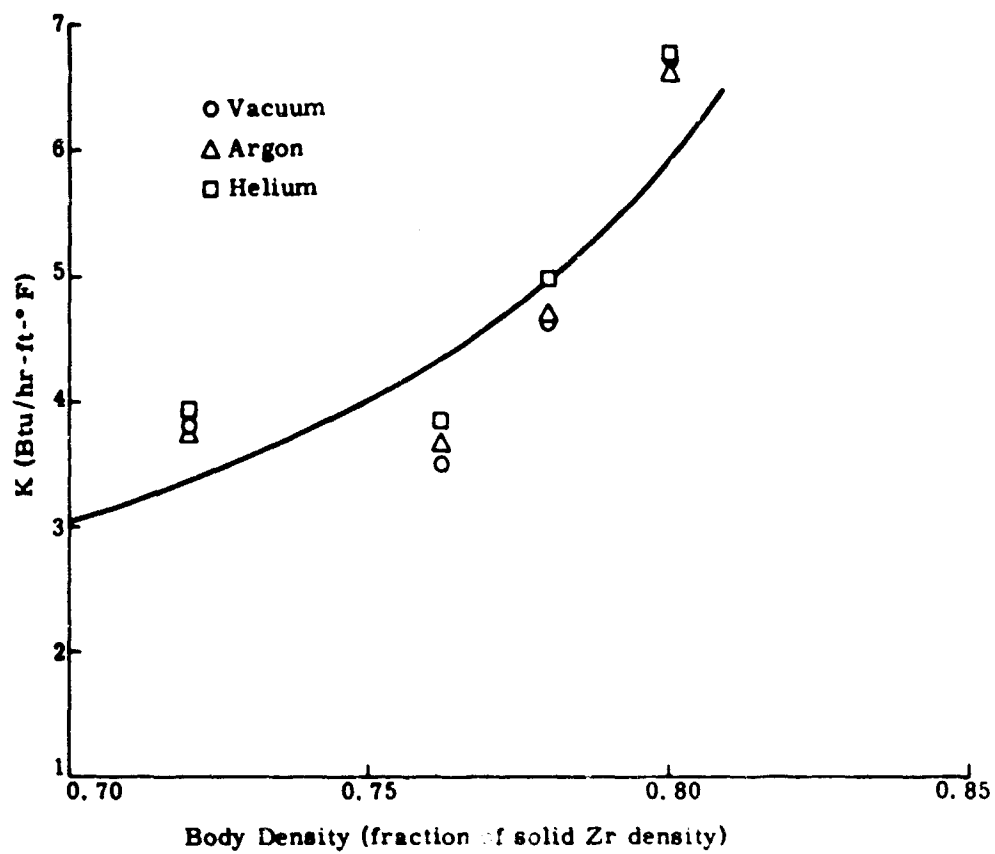
Figure 34.   Relationship Between Conductivity and Body Density at 70° F

Table XVI

EXPERIMENTAL RESULTS FOR HYDRIDED SPECIMENS

Temperature (°F)	Gas	α (cm^2/sec)	k (Btu/hr-ft-°F)
Specimens 6-3; ρ = 73.1 percent; x = 1.59			
70	Vacuum	0.038	3.5
305	Vacuum	0.033	3.7
655	Vacuum	0.030	4.2
70	Argon (1 atm)	0.040	3.6
300	Argon (1 atm)	0.035	3.9
650	Argon (1 atm)	0.032	4.4
Specimen 3-6; ρ = 79.7 percent; x = 1.59			
70	Vacuum	0.047	4.6
345	Vacuum	0.043	5.2
690	Vacuum	0.038	5.9
70	Argon (1 atm)	0.050	4.9
330	Argon (1 atm)	0.044	5.3
700	Argon (1 atm)	0.041	6.3
Specimen 3-8; ρ = 72.4 percent; x = 1.78			
70	Vacuum	0.040	4.0
290	Vacuum	0.038	4.6
640	Vacuum	0.032	4.7
70	Argon (1 atm)	0.044	4.5
280	Argon (1 atm)	0.040	4.7
640	Argon (1 atm)	0.035	5.2
Specimen 6-10; ρ = 79.2 percent; x = 1.78			
70	Vacuum	0.044	5.0
300	Vacuum	0.043	5.7
600	Vacuum	0.038	5.9
800	Vacuum	0.035	6.2
900	Vacuum	0.034	6.3
800	H_2 (1 atm)	0.043	7.5
Specimen 6-8; ρ = 78.6 percent, x = 1.59			
70	Vacuum	0.038	3.8
305	Vacuum	0.037	4.4
625	Vacuum	0.034	5.0
70	95% Ar - 5% H (1 atm)	0.043	4.2
300	95% Ar - 5% H (1 atm)	0.040	4.8
600	95% Ar - 5% H (1 atm)	0.038	5.5
930	95% Ar - 5% H (1 atm)	0.036	6.3
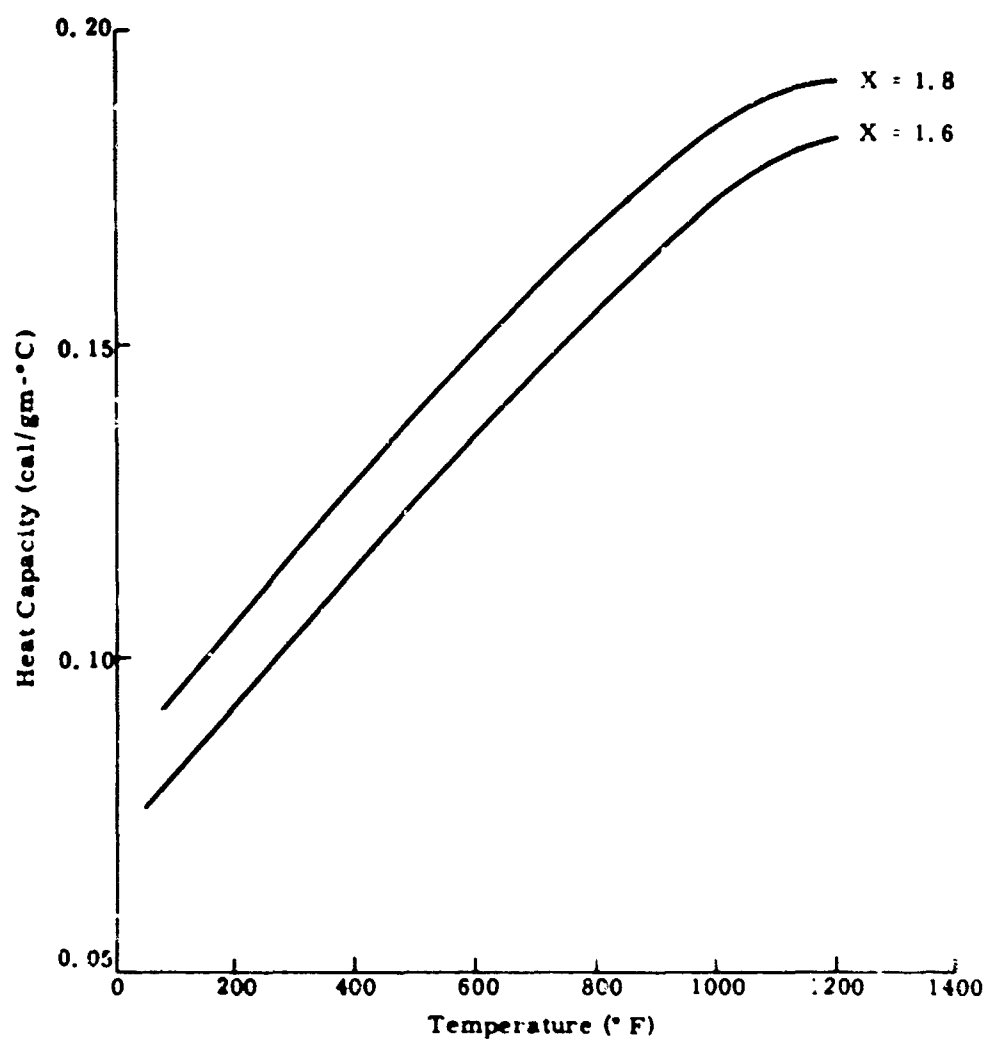
Figure 35. Heat Capacity of ZrH$_x$ (from AFWL TR-66-16)

(1) Low temperature evaluation (no significant hydrogen dissociation pressure)

The thermal conductivity of porous bodies of about 73 and 80 percent of maximum density is compared in figure 36 to solid hydride material conductivity obtained by other investigators. It is apparent that without the presence of gas in the void space, the porous bodies possess about 50 to 60 percent of the solid material conductivity, a result similar to that obtained for the unhydrided zirconium. Likewise, the tabulated data show that argon gas exerts a small effect, less than 10 percent on the body conductivity.

The relationship between conductivity and void fraction for the hydrided bodies is weaker than that observed for the unhydrided zirconium. This small dependence, illustrated in figure 37, is probably a result of increased particle contact during the hydriding process.

(2) High temperature evaluation

Measurements of thermal diffusivity at temperatures where the hydrogen dissociation pressure is significant were undertaken with a mixed argon-hydrogen atmosphere and with a pure hydrogen atmosphere. During the energy pulse transient, the imposed partial hydrogen pressure was maintained at the equilibrium value for the corresponding initial temperature and hydrogen content of the hydride. Because of the small sample temperature rise incurred during the transient ($< 5°$ F), no adjustment was deemed necessary.

The significant finding of these experiments was a marked reduction in the maximum temperature rise recorded. This observation can be explained by the dissociation of hydride in the specimen upon receipt of the radiant energy impulse. Unfortunately, because of the resultant small noisy signal, detailed analysis was not possible. Future efforts are required to yield data amenable to interpretation by application of hydrogen transport analysis.

4. Conclusions and Recommendations

As indicated by the data, the Bruggeman model failed to predict accurate thermal conductivity of the porous zirconium or zirconium hydride matrix. One may conclude that the sintering operation yields sufficient interparticle connection and that the presence of gas in the void space is not necessary to yield good thermal conductivity. This result adds further emphasis to the importance of thorough sintering of the particle matrix. Not only is the body strength increased, but the thermal conductance is greatly enhanced. From the results of hydride
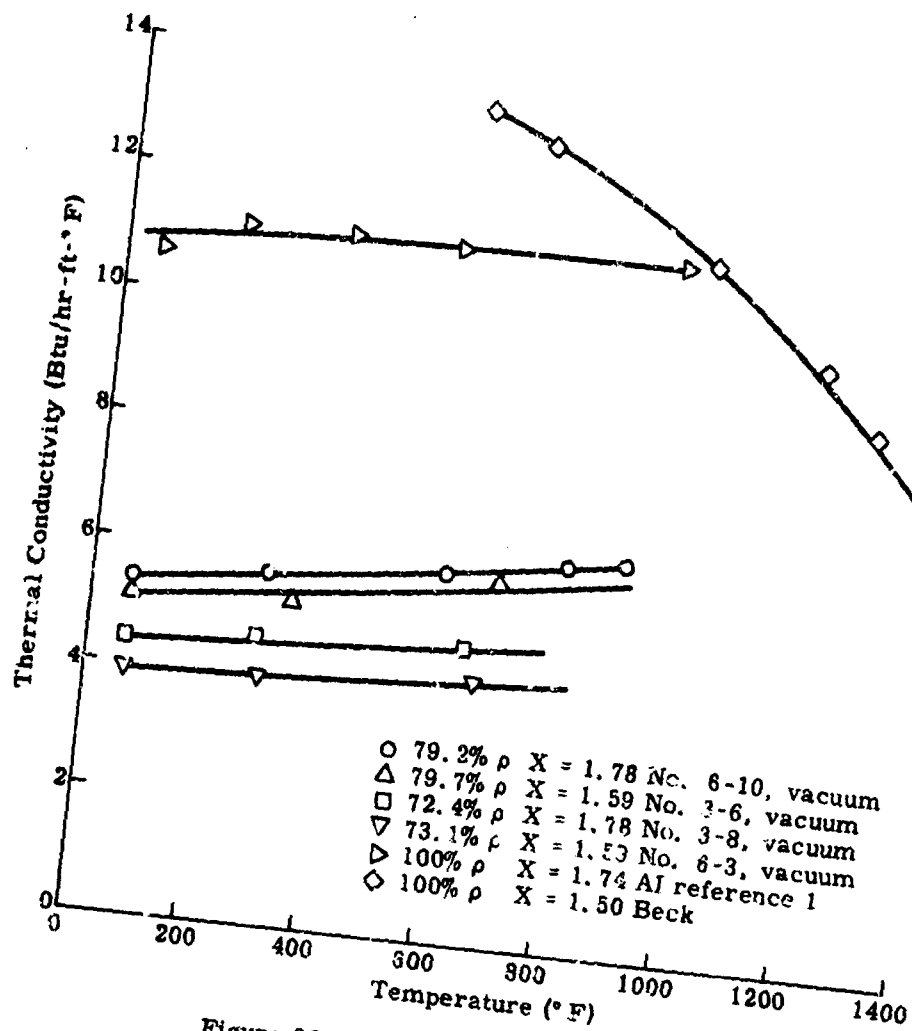
Figure 36. Thermal Conductivity of ZrH_x

- ○ 79.2% ρ   X = 1.78 No. 6-10, vacuum
- △ 79.7% ρ   X = 1.78 No. 3-6, vacuum
- □ 72.4% ρ   X = 1.59 No. 3-6, vacuum
- ▽ 73.1% ρ   X = 1.78 No. 3-8, vacuum
- ▷ 100% ρ   X = 1.59 No. 6-3, vacuum
- ◇ 100% ρ   X = 1.74 Al reference 1
         X = 1.50 Beck

- △ ZrH_x X = 1.78
- ○ ZrH_x X = 1.59
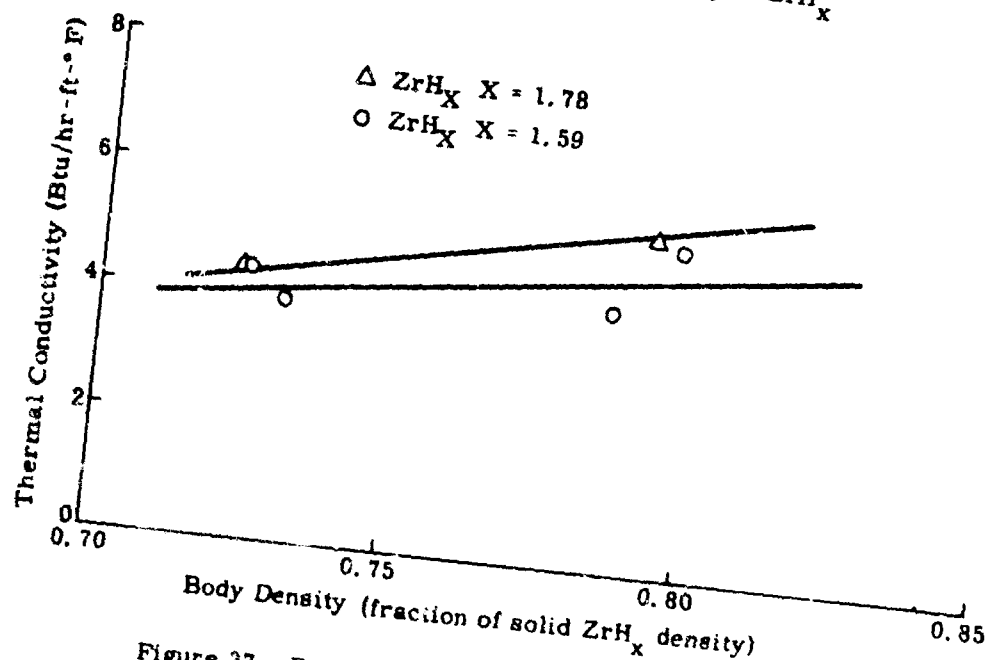
Figure 37. Relationship Between Thermal Conductivity and
Body Density--70° F, Vacuum Conditions

78

conductivities made at low temperature, together with the effect of hydrogen gas on the conductivity of specimen 6-10 at 800° F (a 20 percent increase), it is reasonable to expect thermal conductivities of 7 to 9 Btu/hr-ft-° F at 1500° F for porous bodies of 70 to 80 percent density.

In view of the desirability for measurements at higher temperatures where significant hydrogen pressures exist, together with an investigation of the important effects of the sintering process, additional thermal conductivity studies are recommended. These efforts should encompass a range of specimen fabrication techniques (particle size and sintering) and should emphasize testing at TURPS operating conditions. Also, analysis of the thermal-hydrogen transport phenomena by adaption of the techniques presented in Section II of this report will enable better application of the thermal diffusivity method to this task.

This page intentionally left blank.

SECTION IV

CHEMICAL AND PHYSICAL PROPERTIES OF THEON (P_4S_3)

1. Purpose

It was the purpose of this task to establish, by means of analysis and/or measurement, the specific characteristics of Theon required to permit future TURPS reactor core designs using this material as the coolant. The necessity for undertaking such an investigation stems solely from the lack of such information in the existing literature.

The particular characteristics or properties of interest are as follows:

(1) Viscosity

(2) Surface tension

(3) Thermal conductivity

(4) Vapor pressure

(5) Liquid density

(6) Heat of fusion

In performing the investigation, two major areas of activity were required. The first concerned the preparation of purified Theon to supply the requirements for property evaluation and other tasks such as the Theon irradiation and chemical compatibility studies. The second major area concerned the design and performance of the various physical property measurement experiments.

2. Preparation of Theon

a. Preparation of Purified Stoichiometric Theon (P_4S_3)

Commercial grade P_4S_3 contains trace amounts of elements introduced during the synthesis procedure and, supposedly, a slight excess of free sulfur added to increase the stability of the material. Removal of these impurities, along with any of the higher homologues of phosphorus and sulfur (P_4S_5, P_4S_7, P_4S_{10}...), is desirable to lessen the likelihood of significant changes in the physical and chemical properties of the reactor coolant. The preparation procedure constituted the present standard production procedure for pure P_4S_3. Commercial grade P_4S_3 was purified and converted to stoichiometric P_4S_3 through a series of solvent extraction and distillation steps as follows:

(1) The starting material was heated for two hours at 250° C under an argon atmosphere. Sulfur and the higher sulfides of phosphorus are not stable toward phosphorus when melted, thus only P_4S_3 and P remained in the melt. The addition of excess phosphorus was not necessary because chemical analyses indicated an excess of phosphorus already present in the as-received material.

(2) The molten material, consisting of P_4S_3, red phosphorus, white phosphorus, and inorganic impurities, was allowed to cool to room temperature with the flow of argon continued.

(3) Dissolution of the solid cake was accomplished by the addition of CS_2 to the reaction vessel. The CS_2 dissolved the P_4S_3 and any white phosphorus present, but left the red phosphorus and other solid impurities behind.

(4) After filtration to remove suspended solids, the solution was cooled to dry-ice temperature where the P_4S_3 and white phosphorus separated as fine crystals. The crystals were filtered off, washed with ether and vacuum dried.

(5) The removal of white phosphorus was accomplished through vacuum distillation where the purified P_4S_3 was heated to 360° C under vacuum. The white phosphorus, being more volatile, came off in the first fraction and was discarded. The remaining fraction, consisting of P_4S_3 free of white phosphorus, was cooled, dissolved, recrystallized, filtered, washed and dried as in step 4.

(6) Confirmation of the complete removal of phosphorus was afforded by heating samples of purified P_4S_3 to approximately 500° C for one hour and noting the absence of red or white phosphorus in the condensed vapor.

b. Preparation of Nonstoichiometric Theon (P_4S_3)

(1) Preparation

Theon forms containing five percent excess sulfur, one percent excess sulfur and five percent excess phosphorus were prepared for use in the static corrosion studies. The compositions were formulated by the addition of pure sulfur, and phosphorus to stoichiometric P_4S_3. Wet chemical analyses were performed to confirm the excess sulfur and phosphorus concentrations.

(2) Verification of Theon composition

A weighed sample of Theon was placed in an Erlenmeyer flask and reacted with red fuming HNO_3 under an argon atmosphere in an ice bath. The phosphorus content was thereby oxidized to phosphoric acid and the sulfur was oxidized to sulfuric acid.

The phosphorus was precipitated with a magnesia mixture, collected, calcined at 850° C and weighed as $Mg_2P_2O_7$.

The sulfur was then converted to SO_2, which passed through an iodine solution and was titrated with standard thiosulfate solution. Sulfur content evaluation was less consistent than the phosphorus determination and repeated analyses were necessary.

This method yielded 99.8 percent accountability of stoichiometric P_4S_3 constituents (P and S) and thus enabled confidence in the analysis of excess sulfur and phosphorus systems. For comparison, it should be noted that as-received P_4S_3 showed a slight excess of phosphorus and approximately 2.3 percent other impurities.

   c. Produce Specification Testing for Stoichiometric Theon (P_4S_3)

Procedures for verifying the purity of stoichiometric P_4S_3 include detection of free phosphorus, emission spectroscopy and wet-chemical analysis. Infrared spectroscopy has been used to identify P_4S_3, but adequate sensitivity for impurity inspection has not been obtained yet.

   (1) Detection of free phosphorus

Free phosphorus is detected by heating P_4S_3 to 500° C at the bottom of a Vycor glass tube and observing the vapor condensate in the cool upper tube region. Concentrations of a few parts per million will yield the typical red phosphorus color. White phosphorus is observed by breaking the tube after it has cooled to room temperature. Spontaneous ignition or fuming indicates free white phosphorus.

   (2) Emission spectroscopy

Small quantities of impurities can be detected by emission spectroscopy techniques. Theon material purified by the method described previously showed about 50 ppm silicon content. Less than 1 ppm was observed for any other impurity elements detected (Al, Ca, Cu, Zr, Fe).

   (3) Wet chemistry

As described previously, wet chemical determination of phosphorus and sulfur content will assure Theon content of these components to within 0.2 percent. However, present techniques have not been directed toward impurity detection by this means.

3. Physical Properties Measurements

Measurements of viscosity, surface tension, and thermal conductivity were made. In addition, vapor pressure and liquid density values were obtained for P_4S_3 conditions approximating TURPS operation. Of further interest was the heat of fusion; the heat content measurements about the normal melting point yielded this quantity.

a. Viscosity

To eliminate the necessity for flow corrections, a comparative method was used with a liquid of known, comparable viscosity over the temperature range of interest. Preliminary experiments showed that bismuth was a suitable comparator, and its viscosity was available from references 8, 9 and 10. Measurements of the effluent times for bismuth and P_4S_3 in the same reservoir-capillary configuration (figure 38) at each temperature point of interest enabled P_4S_3 viscosity determination from the following equation which is a simplification of an approach suggested by Kaaschow (reference 11).

$$\eta = \frac{\eta_0 \, \rho \, t}{\rho_0 t_0} \left[1 + k \left(\frac{1}{t_0^2} - \frac{1}{t^2} \right) \right]$$

where:

η = required viscosity of P_4S_3

η_0 = known viscosity of bismuth

ρ, ρ_0 = respective densities of P_4S_3 and bismuth

t, t_0 = respective effluent times of P_4S_3 and bismuth

k = $\dfrac{m \, V^2}{\pi^2 \, \ell_g \, r^4}$

m = a calibration constant

V = volume of P_4S_3

ℓ = capillary length $\simeq$ mean pressure head

r = capillary radius

g = gravitational acceleration

Two capillary-reservoir systems, A and B, and two independently prepared P_4S_3 samples, 1 and 2, were employed in this experiment. The results of system A with samples 1 and 2, and system B with sample 2 are listed in table XVII. These values are plotted in figure 39 and the best fit experimental line is compared to the analytically predicted curve. It is seen that the measured
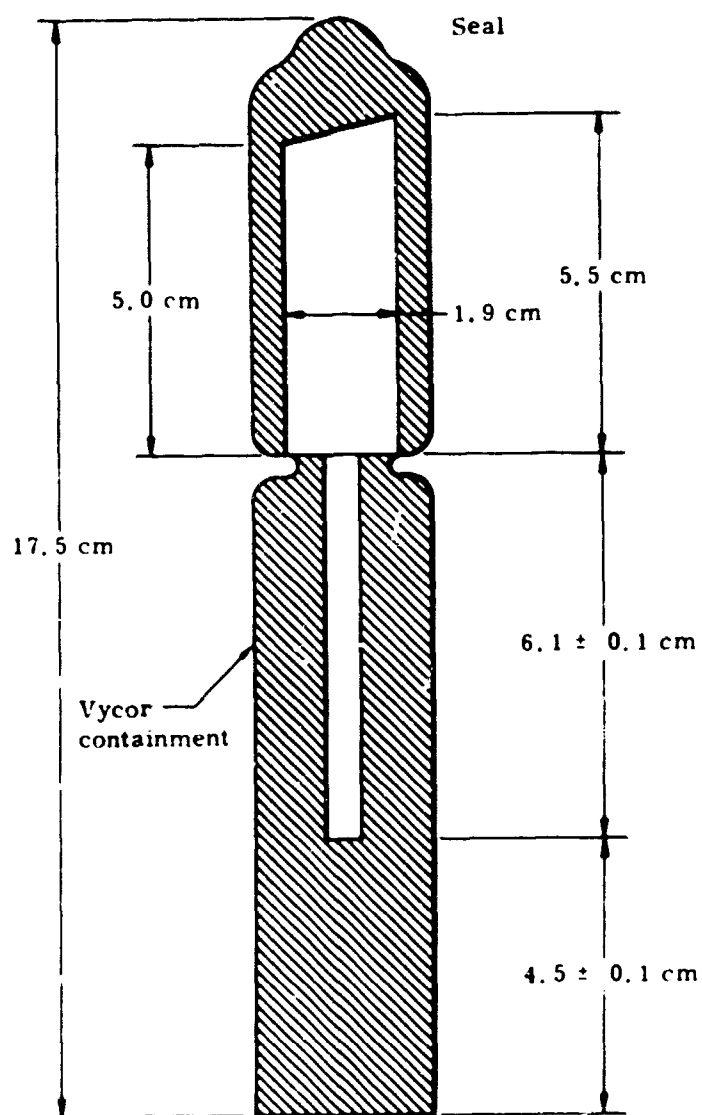
Figure 38. P_4S_3 Viscosity Determination Capsule

85
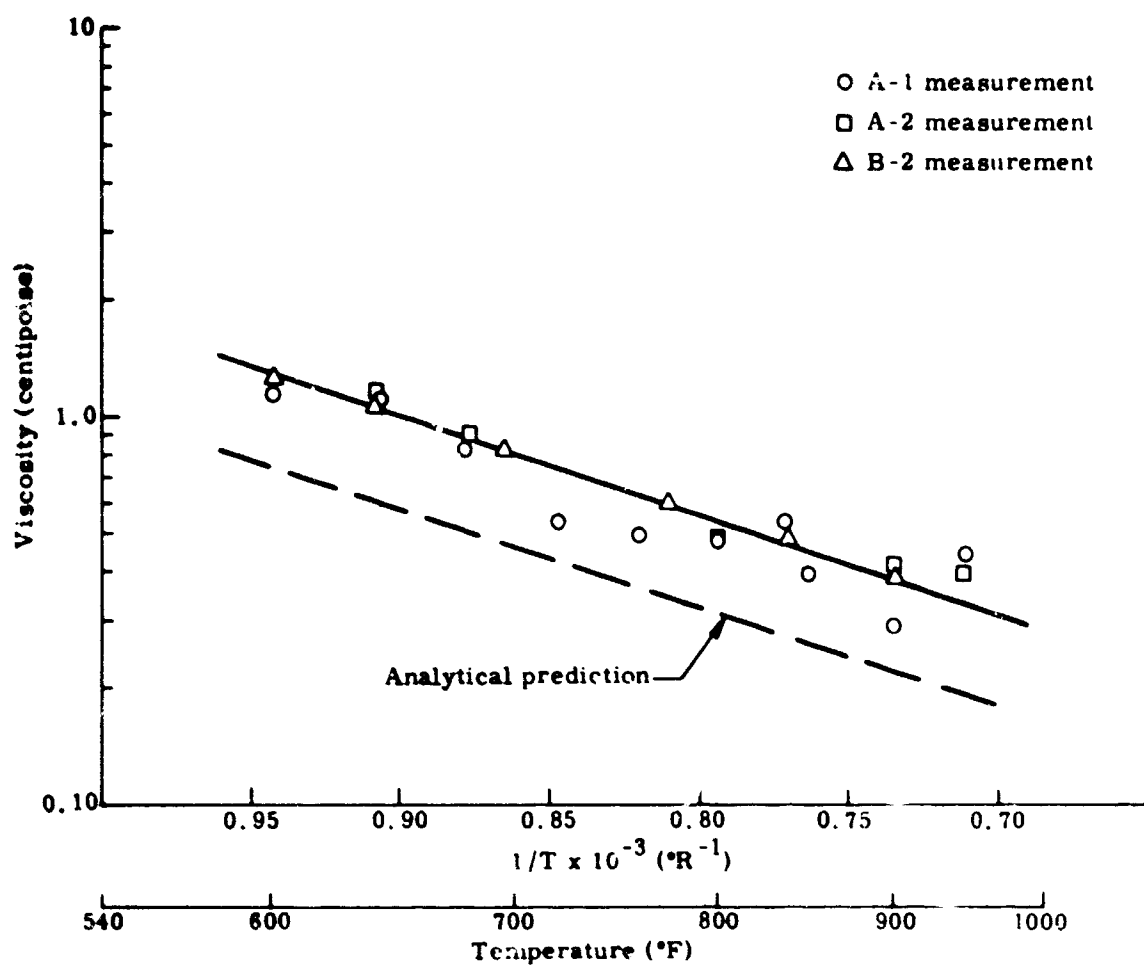
Figure 39. Viscosity of P_4S_3

variation with temperature is very close to the predicted behavior although the absolute value prediction is, as expected, only a rough approximation of the actual observed values.

Table XVII

P_4S_3 EXPERIMENTAL VISCOSITY

1/T (°R^{-1})	Temperature (°F)	Test Viscosity (centipoise)		
		A-1	A-2	B-2
0.943	600	1.160	--	1.261
0.909	640	1.124	1.135	1.057
0.877	680	0.824	0.905	--
0.865	696	--	--	0.827
0.847	720	0.531	--	--
0.820	760	0.491	--	--
0.810	775	--	--	0.601
0.794	800	0.485	0.490	--
0.772	835	0.534	--	--
0.769	840	--	--	0.489
0.763	850	0.392	--	--
0.735	900	0.285	0.425	0.395
0.712	945	0.437	0.398	--

b. Surface Tension

Surface tension measurements of P_4S_3 to 510° C require a pressurized system adapted to the particular physical and chemical characteristics. The method used in this investigation was the capillary-rise technique. The simple apparatus shown in figure 40 provided the basic experimental tool. Careful calibration with known materials assured sufficient accuracy.

The governing liquid rise relationship is: $2\pi r \gamma \cos\theta = \pi r^2 h \rho g$

where

    r = radius of the capillary

    h = height of liquid in capillary above the surface of liquid in which capillary is immersed

    θ = angle of contact of liquid and capillary

    ρ = density of liquid

g = gravitational acceleration

γ = surface tension (dynes/cm)

The values of h and θ are obtained by measurement of the P_4S_3 system, and the radius of the capillary is carefully determined prior to use.

The average diameter of the capillary is determined by classical mercury displacement methods. Tubing lengths of best diameter uniformity are found by examining with a Kodak optical comparator and are used in the regions of capillary rise measurement.

In preparing the surface tension unit, the P_4S_3 was admitted through the top, the assembly evacuated and the Vycor cylinder tapered and sealed. The quantity of P_4S_3 was governed by the known diameter characteristics of the individual capillary tube.

The sealed surface tension unit was then placed in a controlled temperature furnace and subjected to the temperature range of interest while measurements of the capillary rise and liquid contact angle were made with an optical level. Figure 41 shows the arrangement of this experiment. Figure 42 presents the experimental data together with a straight line fit whose equation is

$$\gamma \text{ (dynes/cm)} = 81.5 - 0.398\ T \quad (T = {}^\circ R)$$

It is of interest to note that extrapolation of the data to zero viscosity suggests a critical temperature of about 1590° F, whereas the theoretical prediction was about 1860° F.

c. Thermal Conductivity

The thermal conductivity of P_4S_3 was measured by the flash method of obtaining thermal diffusivity. Separate determination of heat capacity and density enabled evaluation of the thermal conductivity from the following relationship

$$k = \alpha C_p \rho$$

where

k = thermal conductivity

α = measured diffusivity

C_p = measured heat capacity

ρ = measured density

Table XVBI contains the measured quantities, while figure 43 presents the thermal conductivity variation with temperature. It is of interest to note that

Figure 41. Surface Tension Measurement Apparatus
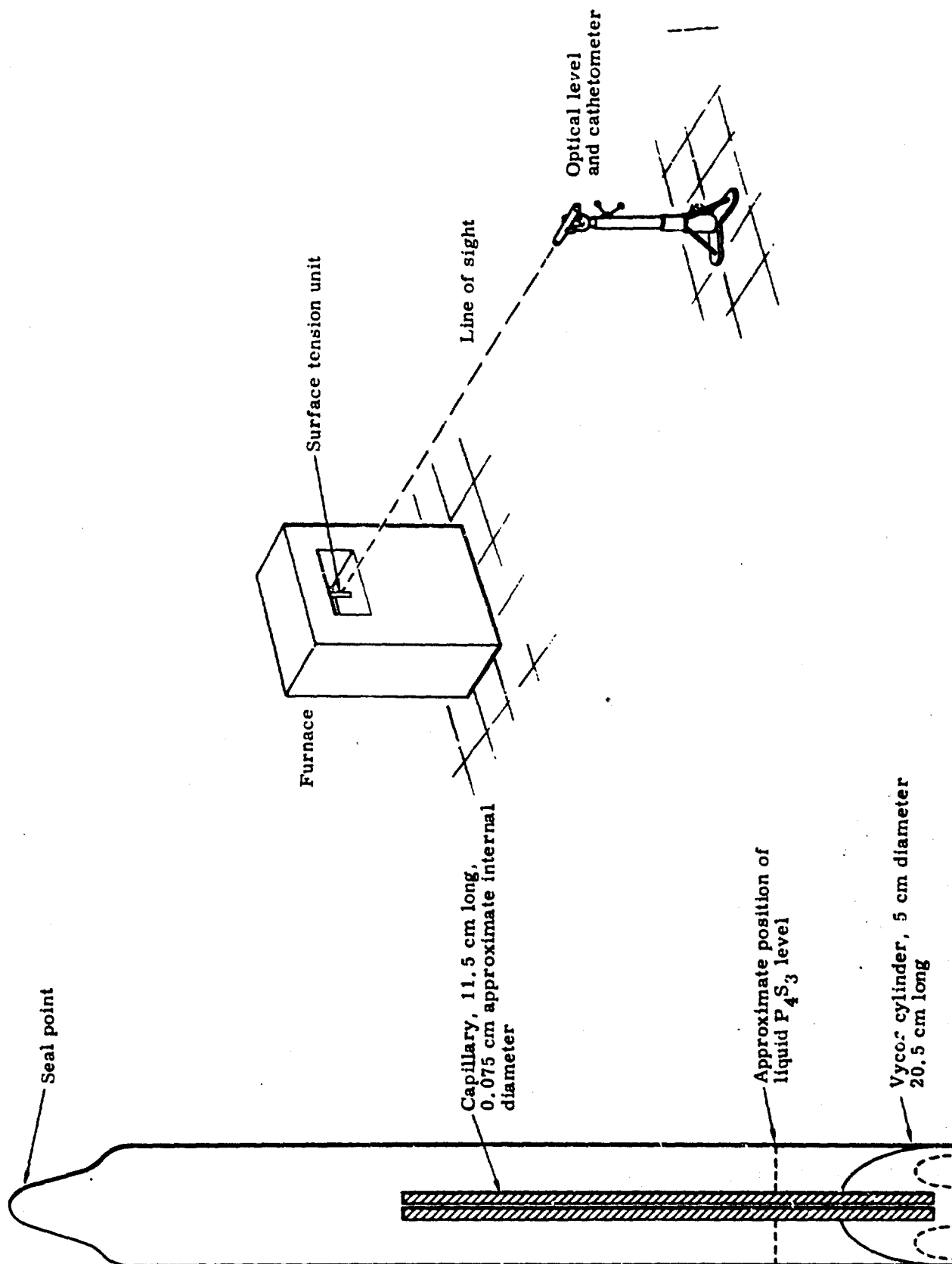
Figure 40. P_4S_3 Surface Tension Unit
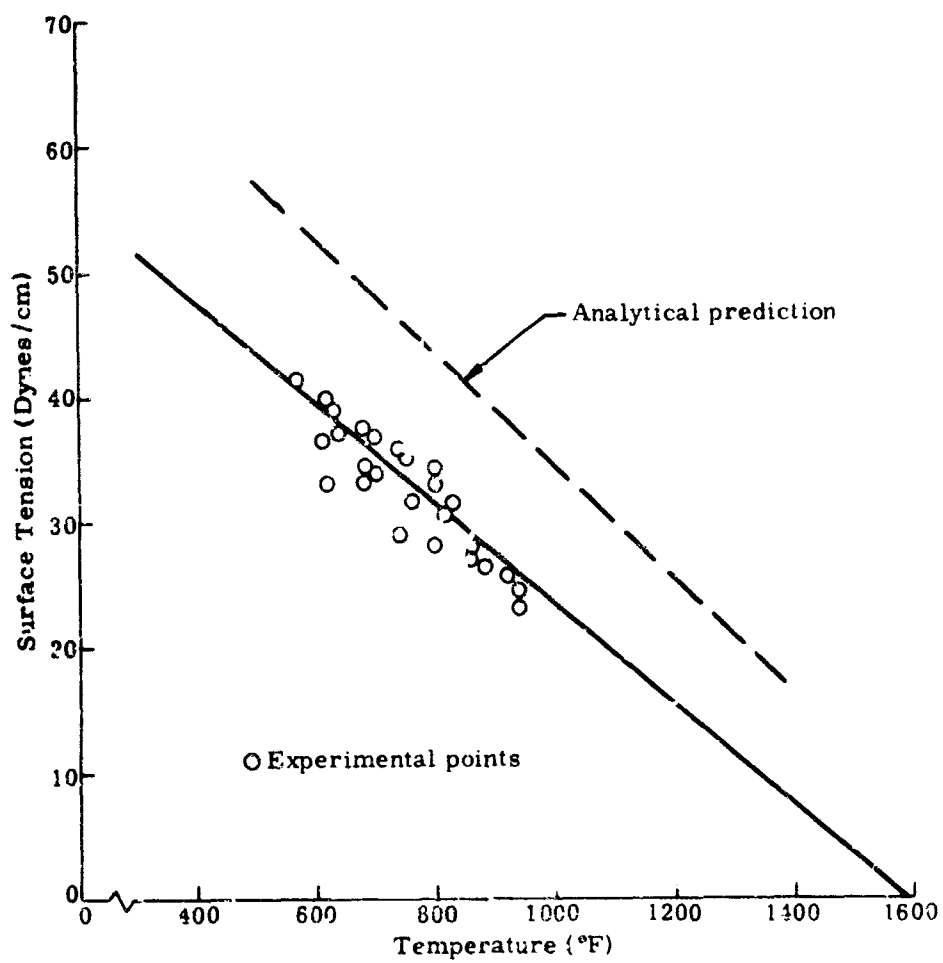
Figure 42. Surface Tension of P_4S_3
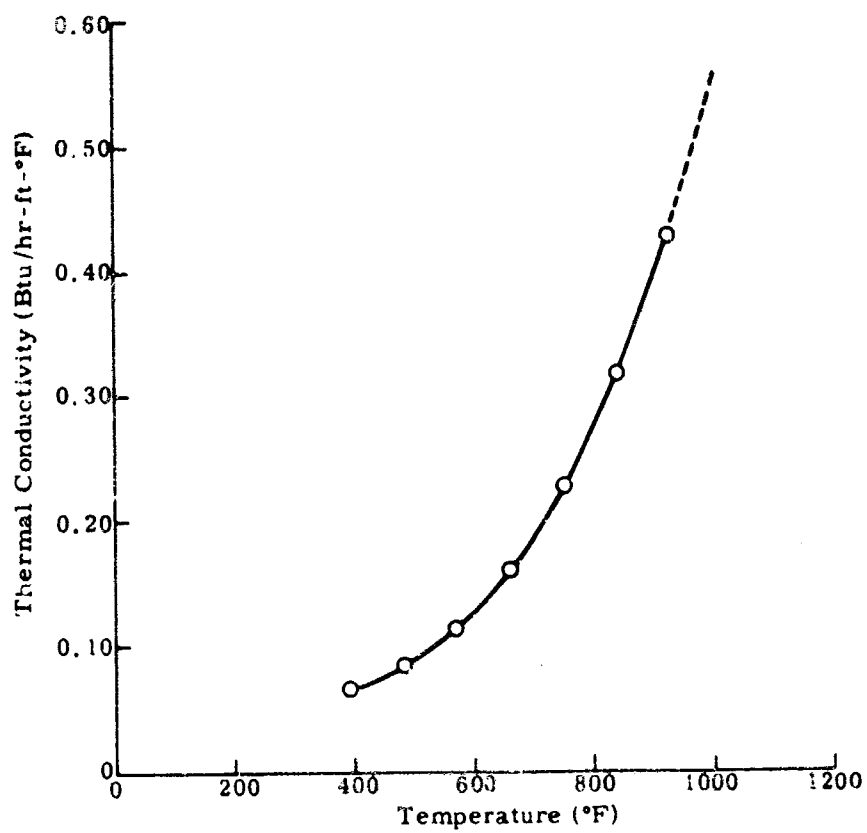
Figure 43. Thermal Conductivity of P_4S_3

the conductivity at 950° F is 0.45 Btu/hr-ft-°F, significantly greater than the prior predicted value of 0.09 Btu/hr-ft-°F. Such a value invites recognition of P_4S_3 as a promising forced circulation coolant with a Prandtl number at 950° F close to that of water (1.0).

Table XVIII

THERMAL CONDUCTIVITY DETERMINATION OF P_4S_3

Temperature (°C)	Density (gm/cm^3)	Heat capacity $(cal/gm-°C)$	Diffusivity (cm^2/sec)	Thermal conductivity $(cal/sec-cm-°C)$
200	1.665	0.184	0.88×10^{-3}	0.270×10^{-3}
250	1.616	0.217	1.02×10^{-3}	0.358×10^{-3}
300	1.570	0.254	1.20×10^{-3}	0.478×10^{-3}
350	1.525	0.298	1.46×10^{-3}	0.663×10^{-3}
400	1.483	0.350	1.80×10^{-3}	0.934×10^{-3}
450	1.445	0.410	2.19×10^{-3}	1.30×10^{-3}
500	1.412	0.481	2.61×10^{-3}	1.77×10^{-3}

d. Vapor Pressure

The vapor pressure of P_4S_3 was measured with the configuration depicted in figure 44. As shown, argon gas was used to balance the P_4S_3 vapor pressure and the U-tube extension was connected to a mercury manometer. Measurement of the argon pressure to maintain equal liquid levels in both sides of the U-tube provided P_4S_3 vapor pressure values up to about 940° F.
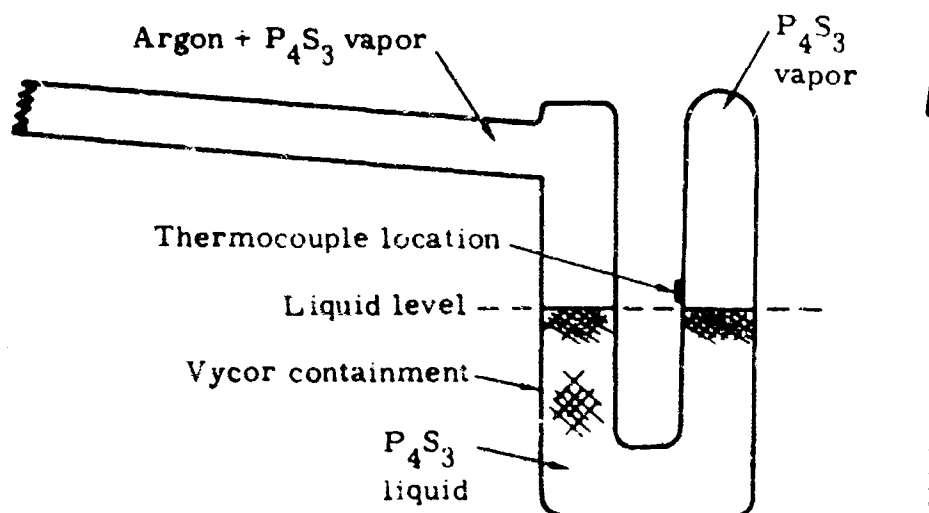
Figure 44. U-Tube for Vapor Pressure Measurement

The experimental data are shown in figure 45. Regression analysis yielded the following equation:

$$\log_{10} P = 6.86 - \frac{2.70 \times 10^3}{T}$$

$P = $ mm Hg

$T = °K$

e. Liquid Density

The liquid density of P_4S_3 was measured by determining the volume of a known weight of P_4S_3. The volume change with temperature was noted by observing the liquid height in a highly uniform and accurately measured Vycor cylinder. A small correction for the Vycor thermal expansion was included.

The experimental results are shown in figure 46 together with a curve which gives the best representation of the recently obtained and previous data.

f. Heat of Fusion

The heat content of solid and liquid P_4S_3 has been reinvestigated about this melting point (172° C) to obtain accurate evaluation of the heat of fusion. The new data, together with that obtained previously (reference 12) is presented in figure 47. From where the solid and liquid heat content intercepts the 172° C temperature line it can be seen that the heat of fusion is nearly 10 cal/gm.

The experiments were performed with an adiabatic ice calorimeter (figure 48) and a vertical drop-tube furnace. The calorimeter had been calibrated to $\pm$ 3 percent accuracy.

The solid P_4S_3 heat content data between 50° and 170° C can be expressed as

$$\Delta H \text{ (cal/gm)} = e^{6.44 \times 10^{-3} T + 2.72}$$

where

$T = °C$

Differentiating this equation with respect to temperature gives the solid material heat capacity versus temperature

$$C_p \text{ (cal/gm-°C)} = \left[6.44 \times 10^{-3} \right] \left[e^{6.44 \times 10^{-3} T + 2.72} \right]$$
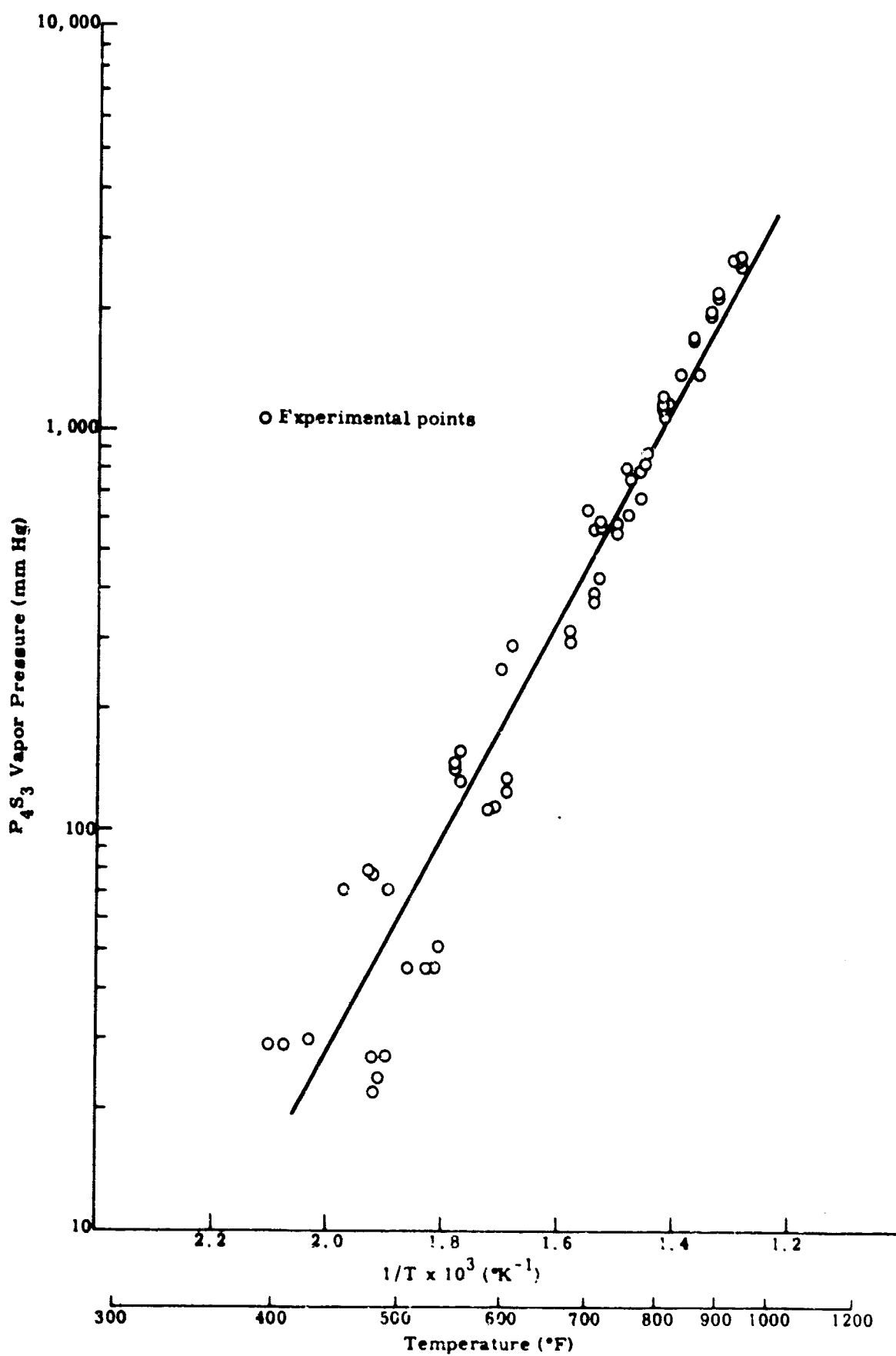
Figure 45. P_4S_3 Vapor Pressure

94
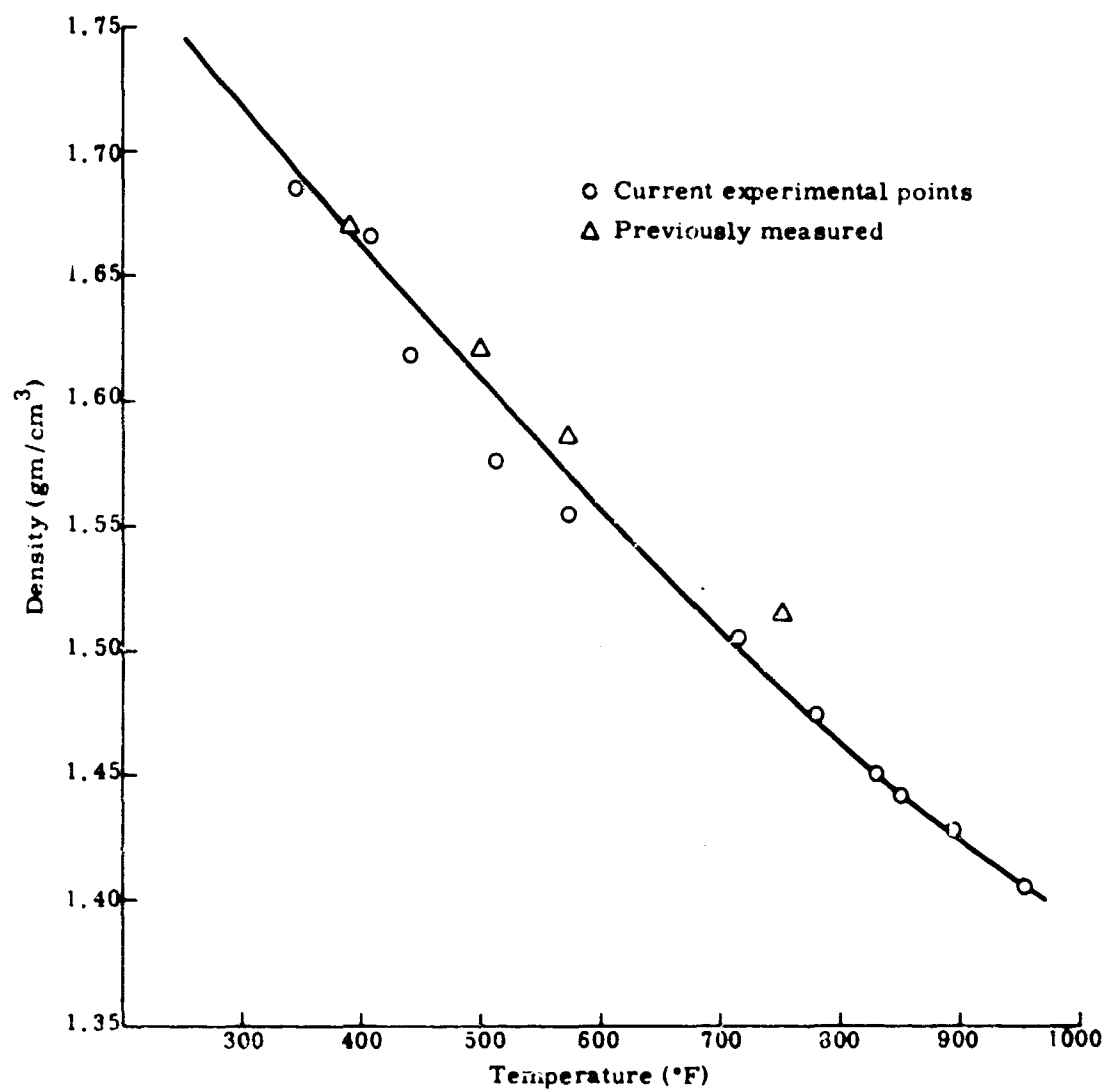
Figure 46. Liquid Density of P_4S_3
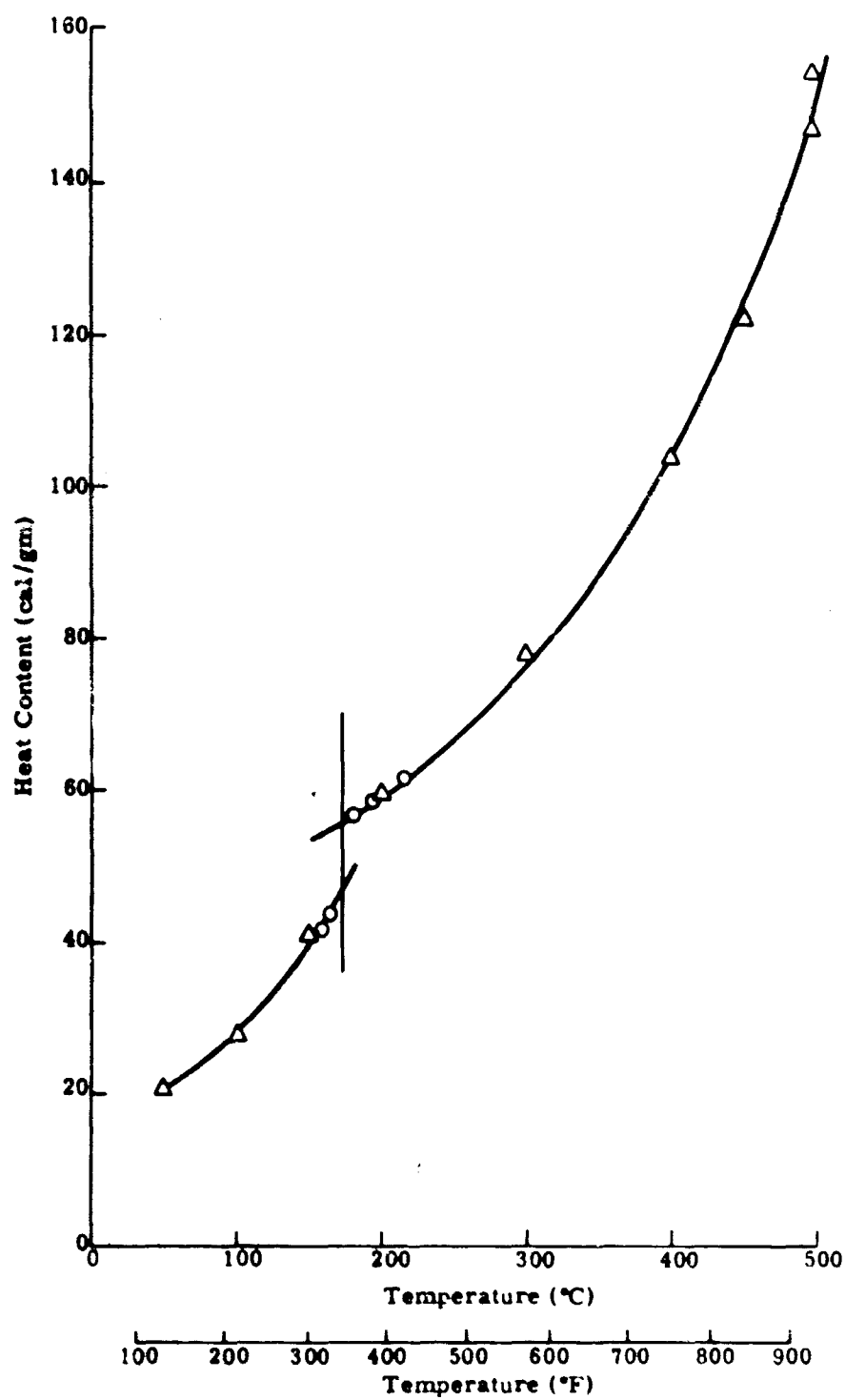
Figure 47. Heat Content of P_4S_3
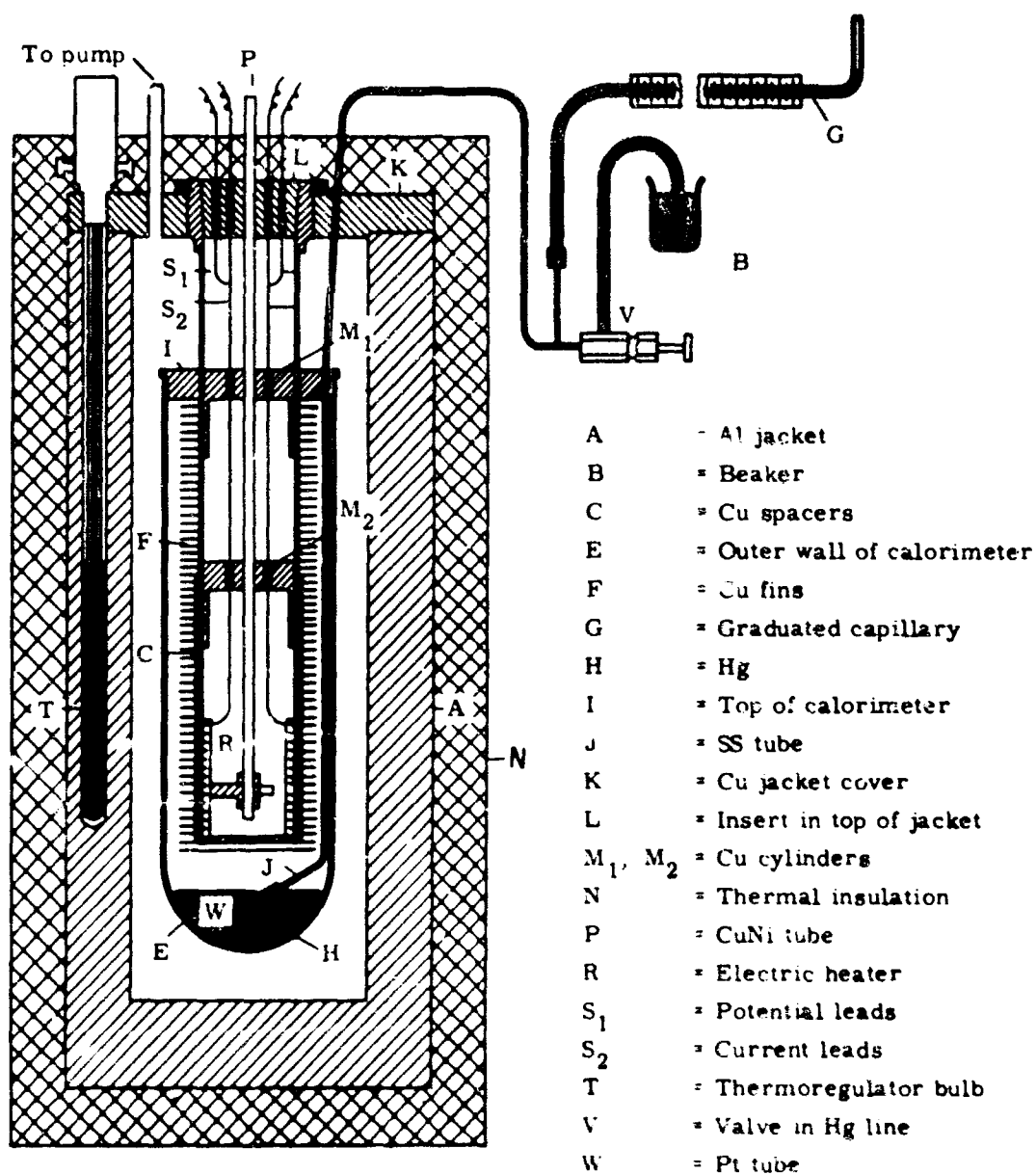
Figure 48. Schematic Drawing of Calorimeter

A   — Al jacket
B   = Beaker
C   = Cu spacers
E   = Outer wall of calorimeter
F   = Cu fins
G   = Graduated capillary
H   = Hg
I   = Top of calorimeter
J   = SS tube
K   = Cu jacket cover
L   = Insert in top of jacket
M_1, M_2 = Cu cylinders
N   = Thermal insulation
P   = CuNi tube
R   = Electric heater
S_1 = Potential leads
S_2 = Current leads
T   = Thermoregulator bulb
V   = Valve in Hg line
W   = Pt tube

Similarly, the liquid heat content follows the relationship

$$\Delta H \text{ (cal/gm)} = e^{3.18 \times 10^{-3}T + 3.425}$$

and the specific heat is given by

$$C_p \text{ (cal/gm-°C)} = 3.18 \times 10^{-3} \left[e^{3.18 \times 10^{-3}T + 3.425} \right]$$

between 180° and 500° C

SECTION V

IRRADIATION OF THEON (P_4S_3)

1. Purpose

The purpose of this task was to investigate the behavior of P_4S_3 in an operating reactor environment of neutron and gamma fluxes. A concurrent analytic-experimental program was performed. The analytic effort enabled study of the energy exchange mechanisms and thereby yielded information for predicting radiation effects. Actual performance data were obtained by irradiating P_4S_3 in the Air Force NETF reactor at cold (< 200° F) and elevated temperatures approximating TURPS operation.

The major efforts under this task included:

(1) Analytic study of radiation effects

(2) Design and fabrication of the test apparatus

(3) Post-irradiation examination

2. Analytic Study of Radiation Effects

The radiation damage of P_4S_3 results from the neutron and gamma fields in the TURPS core. To estimate the magnitude of this effect, it is necessary to calculate the energy deposited in P_4S_3 by neutrons and gammas and the fraction of this energy which results in decomposition. At this point, it should be recalled that from the data on heat of formation, it is evident that to decompose a P_4S_3 molecule (i.e., to form $P_4 + S_3$) at least 1.5 ev of energy must be deposited for each P_4S_3 molecule.

Gamma radiation interacts mostly with the bound electrons, producing free electrons, ions, and X-rays. The X-rays lose energy by collisions with electrons, converting all their energy to heat. The ions and electrons can recombine, liberating more X-rays (ultimately, heat), or, if the lifetimes of the ions are large, they may induce or accelerate chemical reactions leading to molecular decomposition products. In water, ions persist for a long enough time that ionic reactions constitute an important source of stable molecular decomposition products. However, ions are not nearly so stable (have shorter lifetimes) in P_4S_3 as in water, so that ion-ion reactions will contribute less significantly to radiation decomposition processes which terminate in molecular residue. Therefore, it will be assumed that gamma radiation will not contribute significantly to the decomposition of P_4S_3.

Neutron damage is caused primarily by elastic collision of incident neutrons with atomic nuclei in P_4S_3. In a fast neutron collision, the chemical binding energy of the scattering atom can be neglected. For example, in an elastic collision with sulfur, a neutron will, on the average, lose six percent of its energy. This means that a 1 Mev neutron, upon colliding with sulfur, will yield a 940-kev neutron and a 60-kev sulfur atom. Only when the incident neutron energy is as low as 10 ev does the chemical binding energy of the atom become important.

To determine the nature of neutron damage, it is necessary to follow the recoil and determine the manner in which it loses its energy. If ionization is the mode of energy loss most of the energy will be converted to heat as is the case with gamma rays and X-rays. On the other hand, elastic collisions will lead to continued decomposition. The velocity of particles below which ionization becomes negligible is given by (reference 13)

$$V = \frac{e^2}{h} = \frac{c}{137} = 0.22 \times 10^9 \text{ cm/sec}$$

For sulfur this velocity corresponds to an energy of 800 Kev, which is greater than the recoil energy resulting from an elastic collision with a fast neutron. Ionization is not, therefore, the mode of energy loss of the scattered particle. Instead, it will lose energy by elastic collisions, thus causing further decomposition. It can be assumed that in a primary collision the scattered particle will lose all its energy by breaking chemical bonds.

The equilibrium concentration of any chemical decomposition product will depend on its production rate and its chemical recombination rate. It is assumed that all chemical decomposition follows the reaction

$$P_4S_3 \xrightarrow{\text{radiation}} P_4 + 3S$$

It is also assumed that the back reaction rate is given by the following second-order rate equation:

$$\frac{d[P_4]}{dt} = - B [P_4][S_3]$$

where

$$B = B_0 e^{-E/kT}$$

$[P_4]$ and $[S_3]$ are the concentrations of P_4 and S_3, respectivel

and

B_0 and E are constants.

The temperature dependence of B is that of a characteristic Arrhenius reaction, where the chemical reaction is exponentially dependent on the energy of the potential barrier. This equation holds for most reactions where no intermediate products are present, and is assumed to hold for the present case. The net P_4 formation rate is then given by

$$\frac{d[P_4]}{dt} = A - B [P_4] [S_3] \tag{18}$$

where A is the production rate of P_4. The solution to equation (18) is

$$[P_4] = \frac{A}{\alpha} \left[\frac{e^{2\alpha t} - 1}{e^{2\alpha t} + 1} \right] \tag{19}$$

where
$$\alpha = \sqrt{AB}$$
if $[P_4] = [S_3]$.

The corresponding transient time (time for P_4 to achieve 1/e of its equilibrium value) is given by the relation

$$\tau = \frac{1}{2\alpha} \ln \frac{e + 1}{e - 1} \tag{20}$$

and the equilibrium P_4 concentration is

$$[P_4]_o = \frac{A}{\alpha} \tag{21}$$

Equation (19) is the solution to equation (18) when all the free sulfur and phosphorus formed results from the decomposition of P_4S_3. If, however, an excess of sulfur is present and if the concentration of sulfur does not change significantly during the decomposition of P_4S_3, another solution of equation (18) results.

$$[P_4] = \frac{A}{B [S]} \left\{ 1 - e^{-B [S] t} \right\} \tag{22}$$

The transient time is

$$\tau = \frac{1}{B [S]} \tag{23}$$

and the equilibrium concentration is

$$[P_4]_o = \frac{A}{B [S]} \tag{24}$$

To evaluate the decomposition of P_4S_3 in any reactor environment, it is necessary to evaluate A, B_0 and E.

The production rate, A, can be estimated by calculating the energy deposited in the coolant by neutron slowing down scattering.

$$Q = \int_0^\infty \sigma_s \, N \, \phi \, E \, \frac{2M}{(M+1)^2} \, dE \text{ ev/sec cm}^3 \qquad (25)$$

$$\cong N \sum_i \sigma_s \, \phi_i \, \overline{E}_i \frac{2M}{(M+1)^2} \qquad (26)$$

in the notation of the multigroup specification of energy space.

N = atom density in P_4S_3 coolant

σ_s = scattering cross section

ϕ = neutron flux

M = atomic mass of scattering nucleus (30.9 for P, 32.1 for S)

$\overline{E}_i$ = is the midpoint energy of group i

$$\phi_i = \int_{E_{i-1}}^{E_i} \phi(E) \, dE$$

For the TURPS reactor

$$Q = 2.58 \times 10^{20} \text{ ev/sec-cm}^3$$

Since three sulfur atoms must be removed from P_4S_3 to form P_4, the energy of decomposition is 1.5 ev, and this yields a production rate of

$$A = 1.72 \times 10^{16}/\text{cm}^3\text{-sec}$$

B_0 is called the frequency factor in the Arrhenius rate equation. It is related to the degrees of freedom of reacting molecules and to the temperature. A conservative estimate of B_0 is obtained from two complex molecules reacting which yields

$$B_0 \cong 10^{-15} \text{ cm}^2/\text{molecule-sec} \qquad \text{(reference 14)}$$

The activation energy must be determined from experiment and is at the present unknown. It is estimated that 10 kcal/mole is a highly conservative

value in view of the activation energy of other reactions. Consider, for instance, the activation energy for these typical second-order Arrhenius reactions (data from reference 14):

$$H + H_2 \longrightarrow H_2 + H \qquad E = 7.5 \text{ kcal}$$

$$Cl + H_2 \longrightarrow H^{Cl} + H \qquad E = 5.5 \text{ kcal}$$

$$CH_3 + C_3H_6 \longrightarrow C_4H_9 \qquad E = 6.0 \text{ kcal}$$
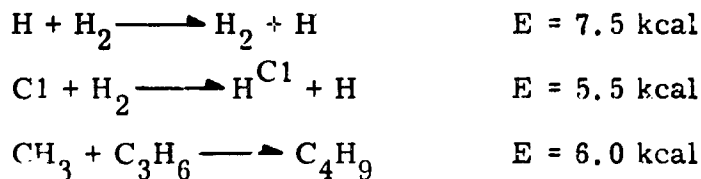
Finally, computation of the back-reaction constant obtains

$$B = 10^{-15} \, e^{-10 \text{ kcal/kt}}$$

$$B = 10^{-18} \text{ cm}^3/\text{molecule-sec}$$

These values yield, when substituted into equations (20) and (21),

$$\tau = 5.0 \text{ seconds}$$

$$[P_4]_o = 2.3 \times 10^{17} \text{ molecules/cm}^3$$

The concentration of P_4S_3 in the coolant is

$$[P_4S_3] = 1.30 \times 10^{21} \text{ molecules/cm}^3$$

so that P_4 represents 0.017 percent of the coolant molecules.

If an excess of one weight percent sulfur is assumed, equations (23) and (24) yield

$$\tau = 1.1 \times 10^{-2} \text{ seconds}$$

$$[P_4]_o = 1.92 \times 10^{14} \text{ molecules/cm}^3$$

so that an excess of sulfur reduces the phosphorus concentration considerably.

The phosphorus concentrations derived are those which would exist in solution with P_4S_3. They should not be taken as the concentrations which exist in the vapor near the condensing surfaces. To determine the amount of free phosphorus which accumulates in the vapor is a problem yet to be investigated; it will depend upon the thermodynamic and chemical properties of both phases, and it may exceed the concentration in liquid phase.

3. Design and Fabrication of Test Apparatus

a. Low Temperature Apparatus

Investigation of P_4S_3 behavior in a reactor environment of neutron and gamma fluxes was pursued by irradiation tests performed in the Air Force NETF reactor. Capsules containing purified stoichiometric P_4S_3 were subjected to an integrated neutron dose of about 10^{19} nvt. The samples were irradiated at ambient temperature (gamma heating to about 200° F) and at 1000° F. Glass encapsulation served to contain P_4S_3 with and without the presence of Zircaloy specimens to test the effect on metal reaction on the radiation stability of P_4S_3.

During the first irradiation in which the test apparatus was under water the heated capsules developed thermocouple performance problems and were not able to complete the required 300 hours irradiation. The unheated capsules performed satisfactorily. Subsequent examination of the first set of heated capsules revealed water leakage and destruction of the specimens.

The results of the unheated capsule irradiation are presented later in this report. The unheated capsule test apparatus consisted of the glass vial as shown in figure 49 further protected by an aluminum outer container.

b. High Temperature Apparatus

The desire to obtain higher fast neutron fluxes than are available in the NETF Bulk Shield Facility, together with the obvious advantage of avoiding the water environment which led to the failure of the first tests, prompted use of the NETF West Test Cell for the second high temperature P_4S_3 irradiation. The air environment of the test cell enabled use of a conventional furnace arrangement with doubly encapsulated P_4S_3 specimens located inside the heated zone. Further, a large part of the heating was supplied by core-evolved gammas and only supplemental electrical heating by the furnace was required.

Figure 50 illustrates the furnace and capsule configuration. Six P_4S_3 capsules were contained inside a Hoskins furnace core. Because of the large gamma heating contribution and relatively low heat loss to the surrounding air, only minimal insulation was required at the top and bottom. Figures 51 and 52 are photographs of the completed furnace assembly and its installation on the NETF West Test Cell dolly.

Each of the six P_4S_3-containing quartz capsules was doubly encapsulated in titanium, a material which incurs low activation and has a short half-life. The P_4S_3 specimens were composed of stoichiometric P_4S_3, P_4S_3 with 0.5 percent excess sulfur, and P_4S_3 with 1 percent excess sulfur. Three vials contained

Figure 49. P_4S_3 Capsule and Titanium Containment Prior to Assembly
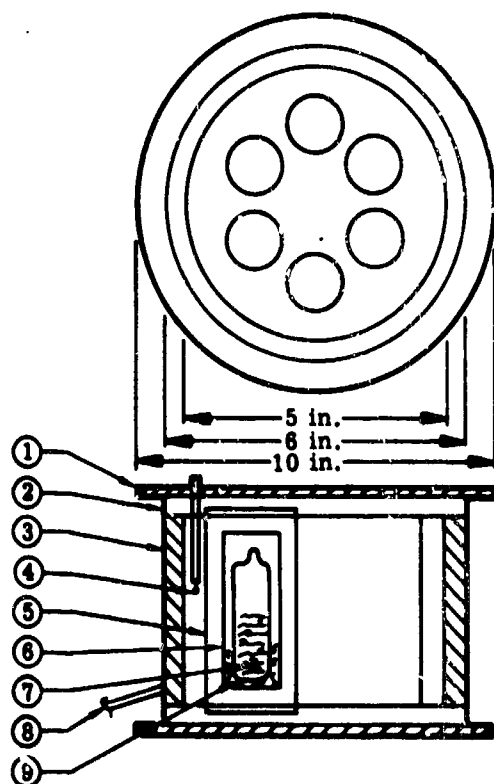
(1) Aluminum plate 10 inch OD x 1/16-inch thick (2, top and bottom)

(2) Fire brick 6 inch OD x 1/4-inch thick (2, top and bottom)

(3) Furnace core (SiC wound with nichrome wire)

(4) Chromel-alumel thermocouples with ceramic insulators

(5) Outer titanium capsules (~5-1/2 inches high x 1 inch OD x 0.012 inch wall
     Six tubes placed as shown on 3-inch ϕ circles 60 degrees apart

(6) Inner titanium capsules (~5 inches high x 3/4-inch OD x 0.040 inch wall

(7) Quartz tubes (6) containing 10 grams P_4S_3 each.   15-millimeter diameter
     x 1-millimeter wall, ~4 inches in height

(8) Aluminum holddown rods (4) spaced 90 degrees apart

(9) Glass wool

Figure 50.   Furnace Configuration of High Temperature P_4S_3 Irradiation
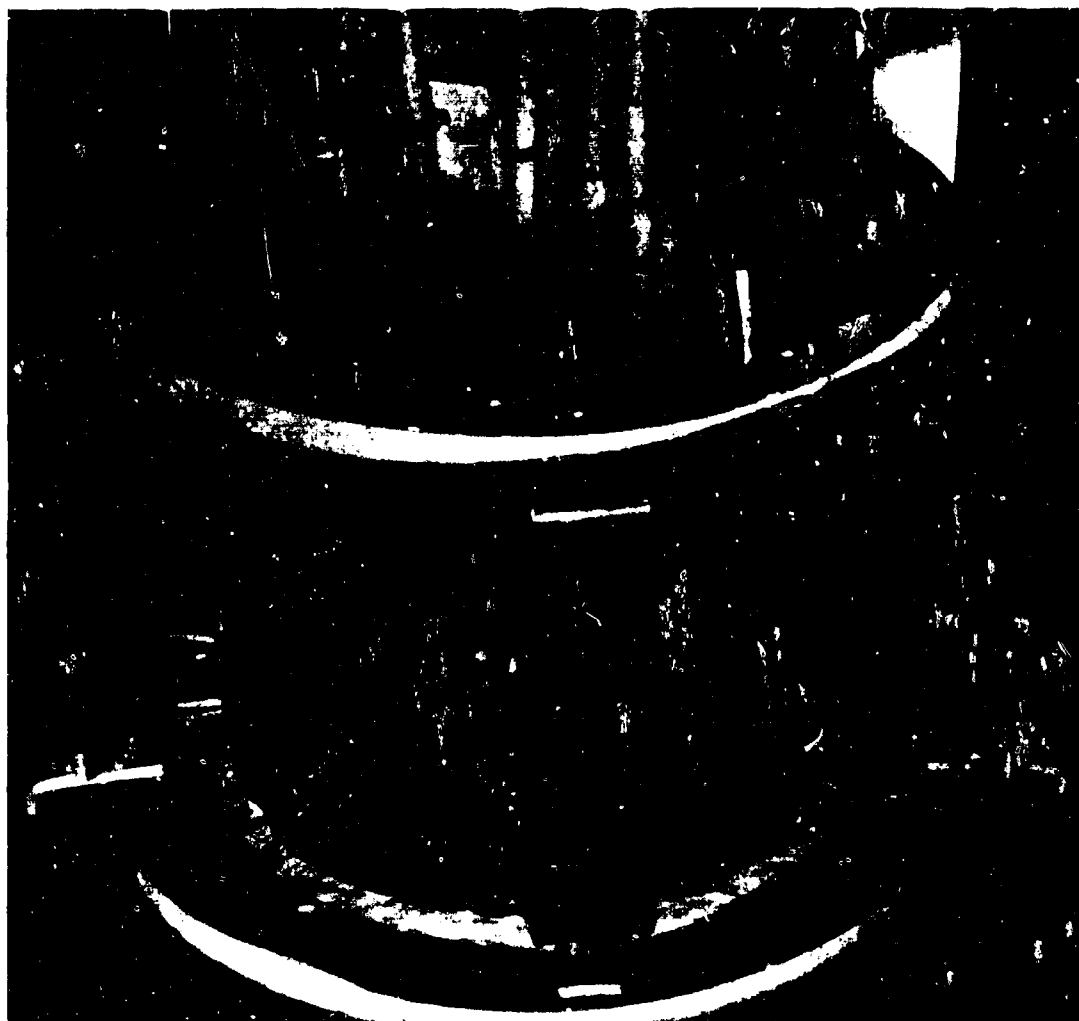
Figure 51. Furnace Assembly of P_4S_3 Irradiation Test
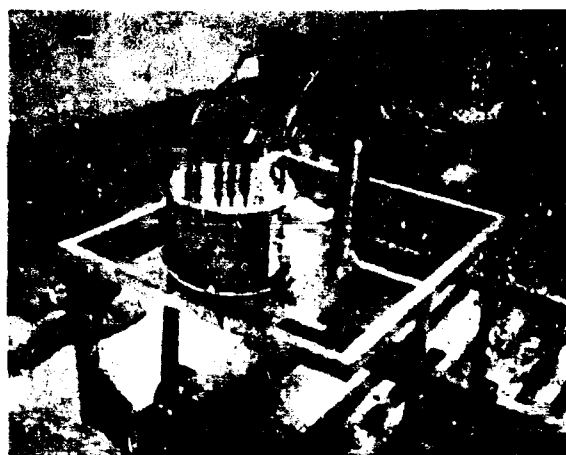
Figure 52. Installation of High Temperature P_4S_3 Irradiation
Test Configuration on NETF West Test Cell Dolly

these compositions only; and the three remaining vials contained a presulfided Zircaloy-2 coupon in addition. The excess sulfur compositions were studied since analytic predictions show greatly reduced dissociation for such material. The reasons for presulfiding of the Zircaloy-2 are given in Section VI of this report.

Figure 49 shows the quartz vial and double titanium containment sleeves prior to assembly. Each quartz vial was approximately four inches long and contained approximately 10 grams P_4S_3.

Because of uncertainties in the West Test Cell gamma flux, the actual operating reactor power level during the test, and the heat transfer calculations, a duplicate furnace with mockup test specimens was installed and operated until equilibrium temperatures were achieved. After verification that the configuration could maintain internal capsule temperatures at about 950° F, the mockup was discarded and the actual P_4S_3 test assembly installed. Subsequent operation of the assembly proceeded smoothly for the desired total of 300 hours with approximately 250 watts supplemental electrical heating required to maintain the capsule walls at 900° F. The corresponding internal P_4S_3 temperature was about 950° F.

4. Post-Irradiation Examination

a. Low Temperature Specimens

The post-irradiation examination of the low temperature P_4S_3 included melting point, viscosity and visual examination as well as inspection of the Zircaloy-2 specimens contained in two of the capsules. Gold foil flux monitors (some cadmium covered) enabled evaluation of the thermal and epicadmium neutron fluxes for each capsule tested. Table XIX presents the flux data.

Table XIX

NEUTRON FLUX EXPOSURE OF THE LOW
TEMPERATURE P_4S_3 CAPSULES

Capsule number	Neutron flux (n/cm^2-sec)		Time integrated flux (300-hr nvt)(n/cm^2)	
	Thermal	Epicadmium	Thermal	Epicadmium
2	0.35×10^{12}	$\sim0.15 \times 10^{11}$	0.4×10^{18}	$\sim0.2 \times 10^{17}$
3	0.94×10^{12}	$\sim0.5 \times 10^{11}$	1.0×10^{18}	$\sim0.5 \times 10^{17}$
6	1.2×10^{12}	$\sim0.6 \times 10^{11}$	1.3×10^{18}	$\sim0.6 \times 10^{17}$
9	2.6×10^{12}	$\sim1.2 \times 10^{11}$	2.8×10^{18}	$\sim1.3 \times 10^{17}$

(1) Melting point evaluation

Measurement of the normal melting point of the irradiated P_4S_3 both as irradiated and after thermal cycling showed essentially insignificant changes

108

from unirradiated P_4S_3. Table XX lists the values for each specimen, the experimental accuracy being $\pm 2.0°$ C. It is seen that all measurements are quite close to the accepted melting point of 172° C.

Table XX

MELTING POINTS OF IRRADIATED P_4S_3

Capsule number	Melting point as-irradiated (°C)	After thermal cycling
2	174	172.5
3	173	170.5
6	172.5	171.5
9	172.5	172.5

(2) Viscosity determination

The evaluation of liquid viscosity dependence on temperature for the irradiated P_4S_3 was made in a similar manner to that described for the unirradiated determinations presented previously. Table XXI contains the measurements for the temperature range of 600° to 950° F.

Table XXI

VISCOSITY MEASUREMENTS OF IRRADIATED P_4S_3

Temperature (°F)	Specimen number viscosity (centipoise)			
	2	3	6	9
600	--	--	1.177	--
620	--	1.072	0.879	--
640	--	--	1.131	--
680	--	0.796	--	--
720	--	--	--	0.612
840	--	0.525	--	--
800	0.378	--	--	--
920	--	--	--	0.513
950	0.324	--	--	0.412

Similarity between the viscosities of irradiated and unirradiated P_4S_3 is shown in figure 53 which contains the values of table XXI plotted over the best fit line from the unirradiated data (from figure 39). It is apparent that no significant viscosity property change has occurred.
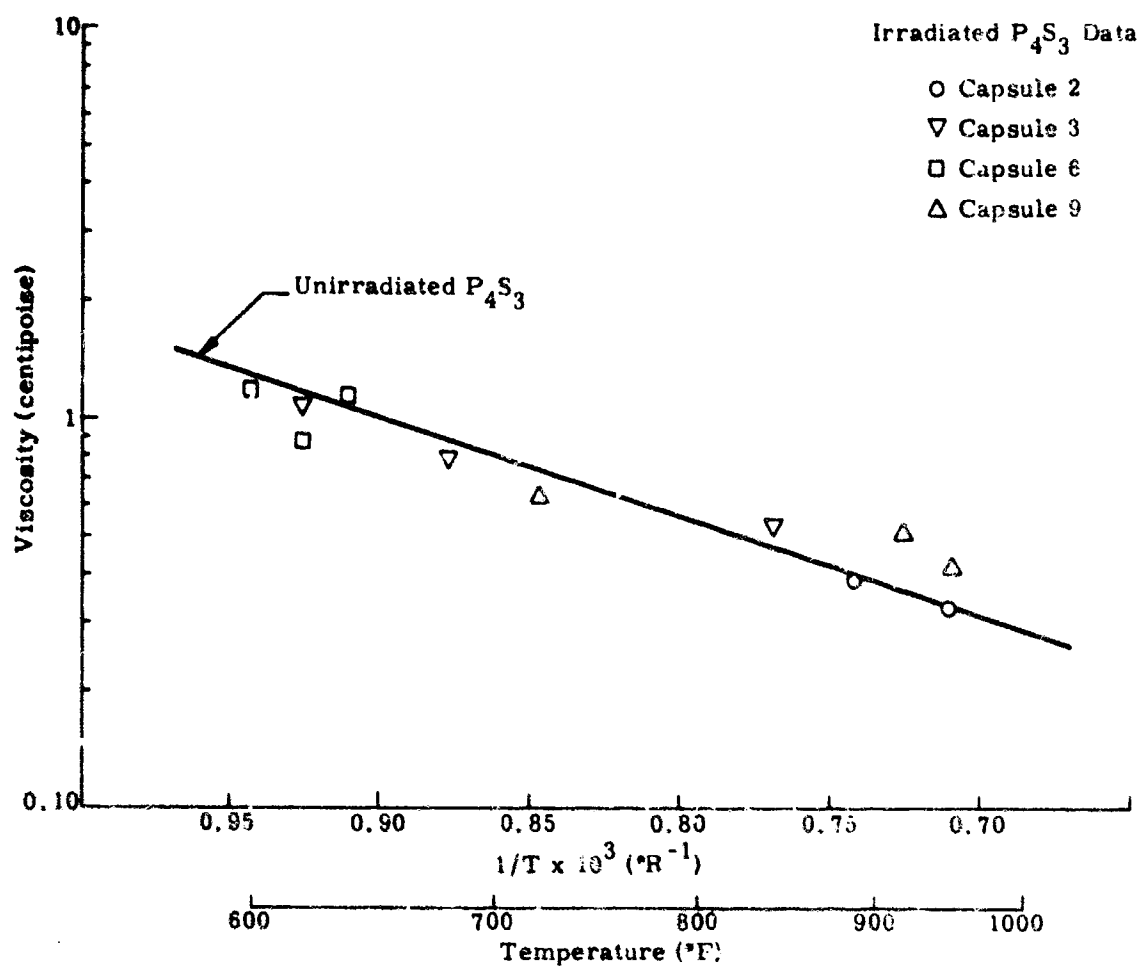
Figure 53. Viscosity of Irradiated P_4S_3

(3) Visual inspection of P_4S_3 and Zircaloy-2 coupons

Visual examination of the P_4S_3 subsequent to irradiation and upon melting during the melting point and viscosity tests revealed normal P_4S_3. The initial coloring and darkening upon temperature raising was identical to that of unirradiated material.

Capsules 2 and 3 contained coupons of Zircaloy-2 about 0.5 by 0.25 by 0.030 inch. As expected, these specimens exhibited no change in appearance since the surrounding P_4S_3 was at low temperature and not molten. Also, the P_4S_3 in these capsules exhibited the same properties as the material in capsules 6 and 9, which contained P_4S_3 alone.

(4) Analysis and summary

The fast neutron flux exposure of the irradiation specimens was about 0.003 of the TURPS fast flux. This yields an analytical prediction of the equilibrium $\left[P_4\right]$ concentration of about 0.001 percent of the Theon molecules at 950° F. Such a small composition change is in agreement with the observed absence of discernible radiation effects.

As previously shown, the analytic model indicates only 0.02 percent $\left[P_4\right]$ concentration at TURPS operating conditions. Such a small dissociation should yield essentially no coolant property changes.

b. High Temperature Specimens

Post-irradiation examination of each of the six Theon specimens irradiated at approximately 950° F included melting point, viscosity and visual studies as well as inspection of the Zircaloy-2 specimens contained in three of the capsules. Gold foil flux monitors enabled determination of the average thermal neutron flux exposure, while the titanium capsule material activation from the Ti^{46} (η, p) Sc^{46} reaction provided a measure of the fast neutron flux above 2 Mev. Since the test was conducted in the nonmoderating medium of the test cell (air and heavy element structure), the fast and thermal neutron flux distributions were quite uniform in the experimental configuration. Average values of 2.2×10^{12} η/cm^2-sec for the fast flux (>2 Mev) and 1.0×10^{13} η/cm^2-sec for the thermal flux were obtained with only about 10 percent deviation across the test assembly.

Table XXII contains the capsule identification and contents data.

Table XXII

HIGH TEMPERATURE THEON IRRADIATION SPECIMENS

Capsule No.	Theon Composition	Zr-2 Coupon
1	Stoichiometric P_4S_3	No
2	Stoichiometric P_4S_3	Yes
3	P_4S_3 + 0.5 wt % S	No
4	P_4S_3 + 0.5 wt % S	Yes
5	P_4S_3 + 1.0 wt % S	No
6	P_4S_3 + 1.0 wt % S	Yes

(1) Visual inspection of Theon and Zircaloy-2 coupons

Visual examination of the Theon subsequent to irradiation showed the presence of dark deposits on the walls of the quartz containers. Most of this material remained attached to the walls upon transfer of the Theon to the viscosity test apparatus. However, specimens 3 and 4 contained sufficient insoluble material within the Theon matrix that viscosity measurements were prevented because of clogging of the small venturi tube in the test apparatus. This material is believed to be a reaction product with the glass container surface. Despite this, however, all of the Theon specimens exhibited the normal color change from bright yellow to dark brownish red upon melting and increasing of the temperature to 950° F.

The Zr-2 coupons exhibited a uniform dark coating that was well adhered to the surface. The presence of zirconium sulfide was verified by the X-ray diffraction study.

(2) Viscosity determination

The evaluation of liquid Theon viscosity dependence on temperature for the high temperature irradiated specimens was made in a similar manner to that described for the unirradiated measurements presented previously. Table XXIII contains the results of these measurements. An unirradiated specimen (7) was included to provide a check of the method and to obtain values for Theon containing P_4S_3 with one weight percent excess sulfur.

Table XXIII

VISCOSITY MEASUREMENTS OF THEON
IRRADIATED AT 950° F

Temperature (°F)	Specimen Number Viscosity (centipoise)				
	1	2	5	6	7
610	1.149				
625				1.255	
630		1.034			
660					1.283
680			0.987		
750		0.656			
765			0.605		
785					0.514
790				0.572	
905	0.448	0.396			
925			0.450		
930					0.451
935				0.420	

Similarity between the viscosities of irradiated and unirradiated P_4S_3 is apparent in figure 54 which contains the values of table XXIII plotted over the best fit line from the unirradiated data. No significant viscosity change is observed. In addition, the unirradiated P_4S_3 with one weight percent excess sulfur exhibits the same viscosity as stoichiometric P_4S_3.

(3) Melting point evaluation

Measurements of the normal melting point of Theon irradiated without the presence of Zircaloy-2 showed essentially insignificant changes from unirradiated Theon. However, the melting points obtained from samples irradiated with Zircaloy-2 coupons were 2° to 3° F lower. This lowering of the melting point may be attributed to the presence of dissolved metal sulfide in the Theon. This observation agrees with indications of limited solubility of the metal surface sulfide layer obtained during surface treatment investigations presented in Section VI of this report.
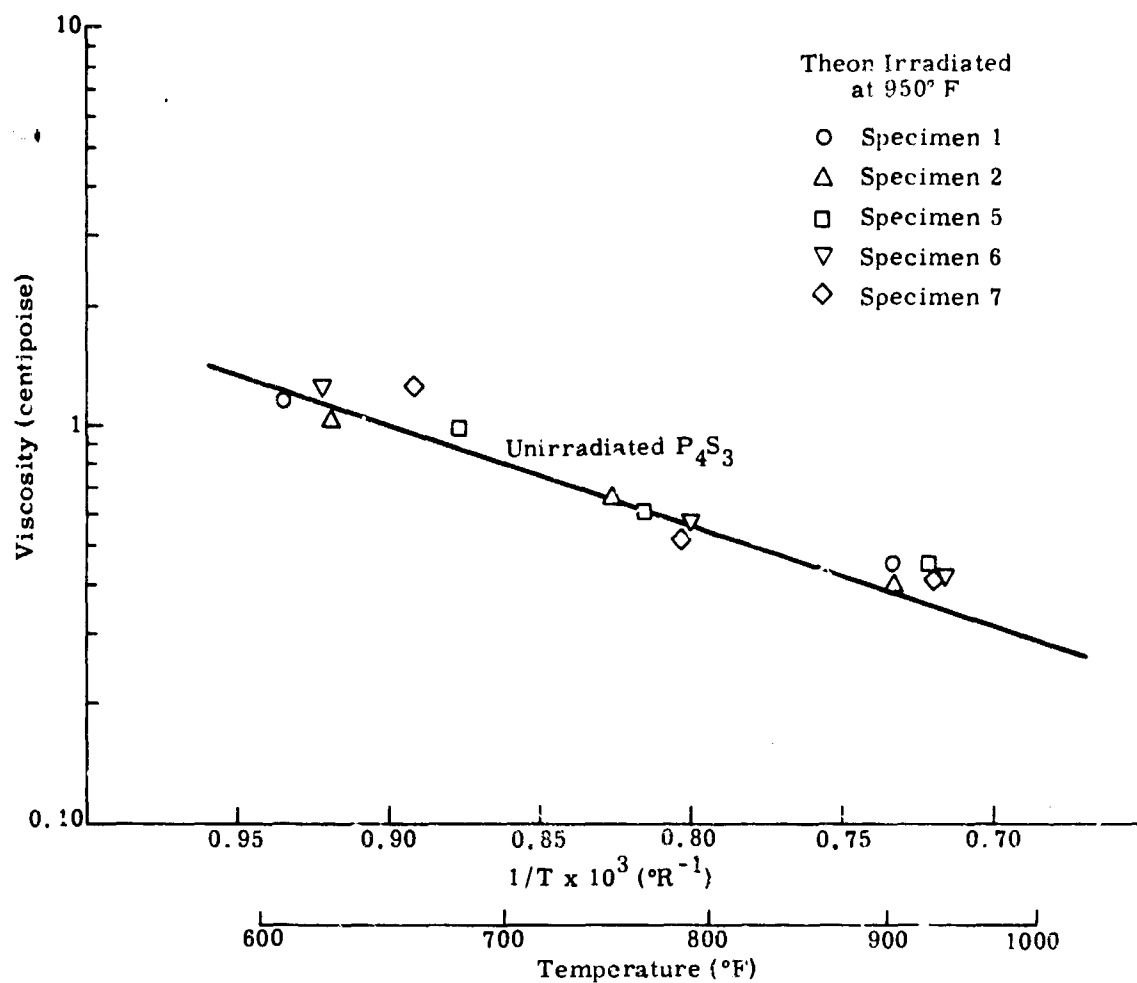
Figure 54. Viscosity of Theon Irradiated at 950° F

(4) Analysis and summary

The fast neutron flux (>2 Mev) exposure of the high temperature irradiation test was about 0.1 of the TURPS fast flux (about 30 times the fast flux received by the low temperature test). This yields an analytical prediction of the equilibrium $[P_4]$ concentration for stoichiometric P_4S_3 of about 0.002 percent of the number of molecules at 950° F. Such a small composition change is in agreement with the observed absence of coolant property changes. Furthermore, as shown in the analytic study, the addition of excess sulfur greatly reduces the equilibrium $[P_4]$ concentration, but since all coolant property changes were negligible, distinction of the sample behavior with excess sulfur present was not possible.

The excess sulfur specimens did, however, contribute an interesting observation for the capsules containing a Zircaloy-2 coupon. Small amounts of free phosphorus were detected in the specimens containing stoichiometric P_4S_3 and 0.5 weight percent excess sulfur in P_4S_3, but no phosphorus was observed in the one weight percent excess sulfur specimen. Thus, it appears that reaction of the Theon with the Zircaloy-2 surfaces yielded some free phosphorus when less than 0.5 weight percent excess sulfur was present, but the one weight percent excess sulfur condition prevented the freeing of phosphorus. Quantitative evaluation of the rate and extent of Theon reactions with Zircaloy as a function of Theon composition (percent excess sulfur) will be the subject of future investigations.

Both the low and high temperature irradiation tests have supported the analytic prediction of a very high recombination of P_4S_3 dissociation products in a radiation field. Insignificant property changes were noted with and without the presence of Zircaloy-2, a promising Theon containment material for TURPS.

This page intentionally left blank.

SECTION VI

CHEMICAL COMPATIBILITY OF THEON WITH METALS

1. Purpose

Previous investigation of purified P_4S_3 compatibility with Zircaloy indicated no evidence of corrosive attack. However, earlier studies of metals with commercial grade P_4S_3 showed small rates of corrosion on Zircaloy and a much larger attack of austenitic stainless steels such as SS 304. The purpose of the present task was to evaluate the performance of structural materials through static corrosion tests of SS 304, SS 310, Hastelloy-N, Zircaloy-4 and Zircaloy-2 with purified P_4S_3. In addition, the effects of excess sulfur, excess phosphorus and a small amount of chlorine added to the P_4S_3 were to be investigated.

A second major objective of the compatibility studies was the performance of a dynamic corrosion loop test of 4500-hour duration at simulated TURPS conditions incorporating the material selected from the static screening tests.

2. Static Corrosion Tests

a. Experiment Description

Five materials were evaluated during this investigation based on anticipated corrosion resistance in the P_4S_3 environments. Specimens of Zircaloy-4, Zircaloy-2, Hastelloy-N and Types 310 and 304 stainless steels were selected for exposure to Theon environments consisting of P_4S_3 (stoichiometric), P_4S_3 + 5%S, P_4S_3 + 1%S and P_4S_3 + 5%P. In addition, specimens were tested in stoichiometric P_4S_3 and P_4S_3 + 5%S with a small amount of chlorine gas (5 ppm) to duplicate conditions expected after five years of reactor operation. Each metal was tested in a capsule constructed of the same material to eliminate foreign corrosion products. Samples were suspended from brackets and immersed in liquid P_4S_3, in the vapor phase and approximately at the liquid-vapor interface.

All capsule loading and final welding was completed in an inert (argon) atmosphere. Each capsule was evacuated to 0.025 mm Hg vacuum and sealed. The chlorine gas-containing capsules were evacuated and backfilled from a manifold with measured quantities of gas (figure 55). All tests were run at 1000° F for 500 hours. The test apparatus is shown in figure 56. The specimens after exposure are shown in figures 57 through 63.
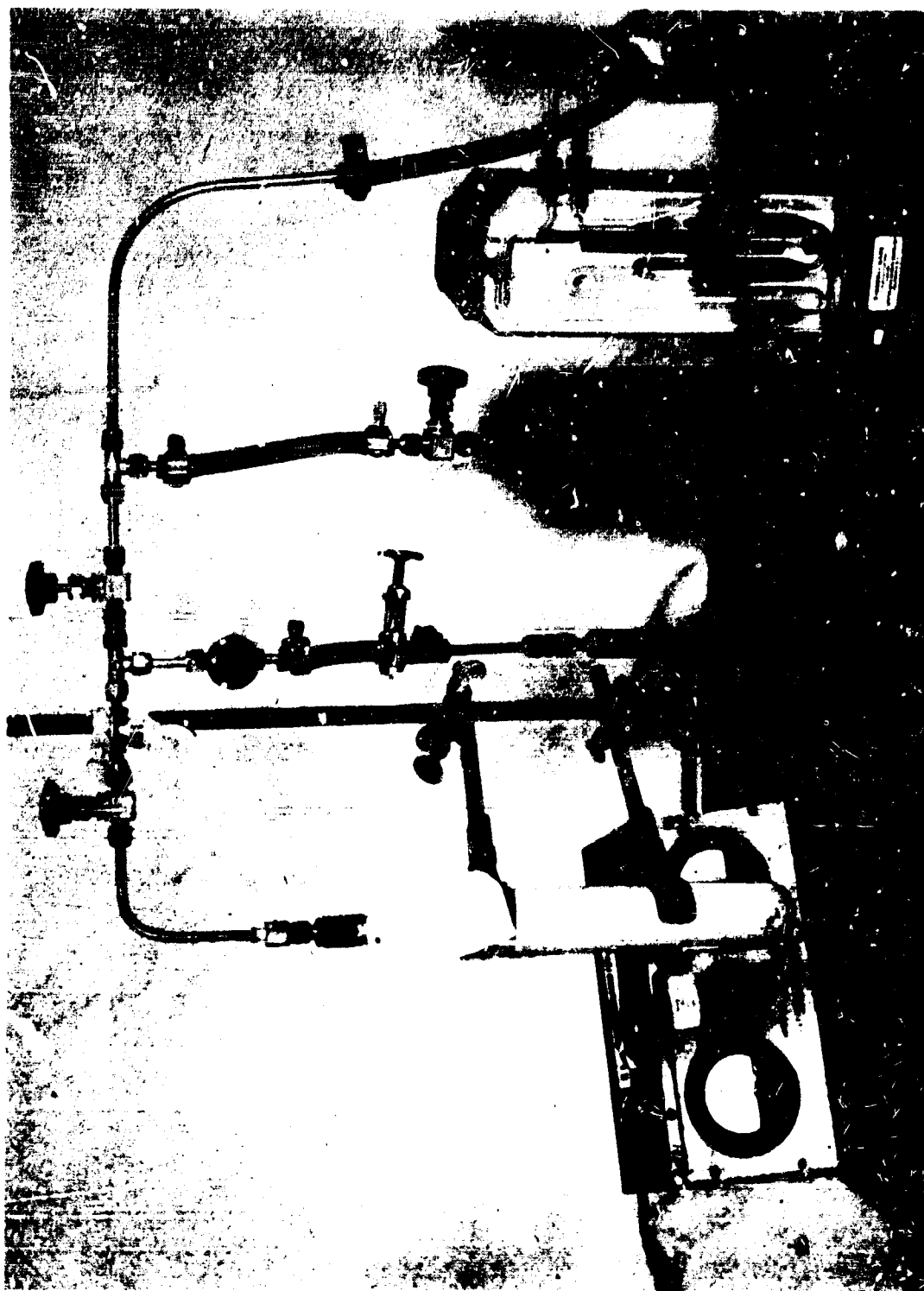
Figure 55. Chlorine Addition Apparatus
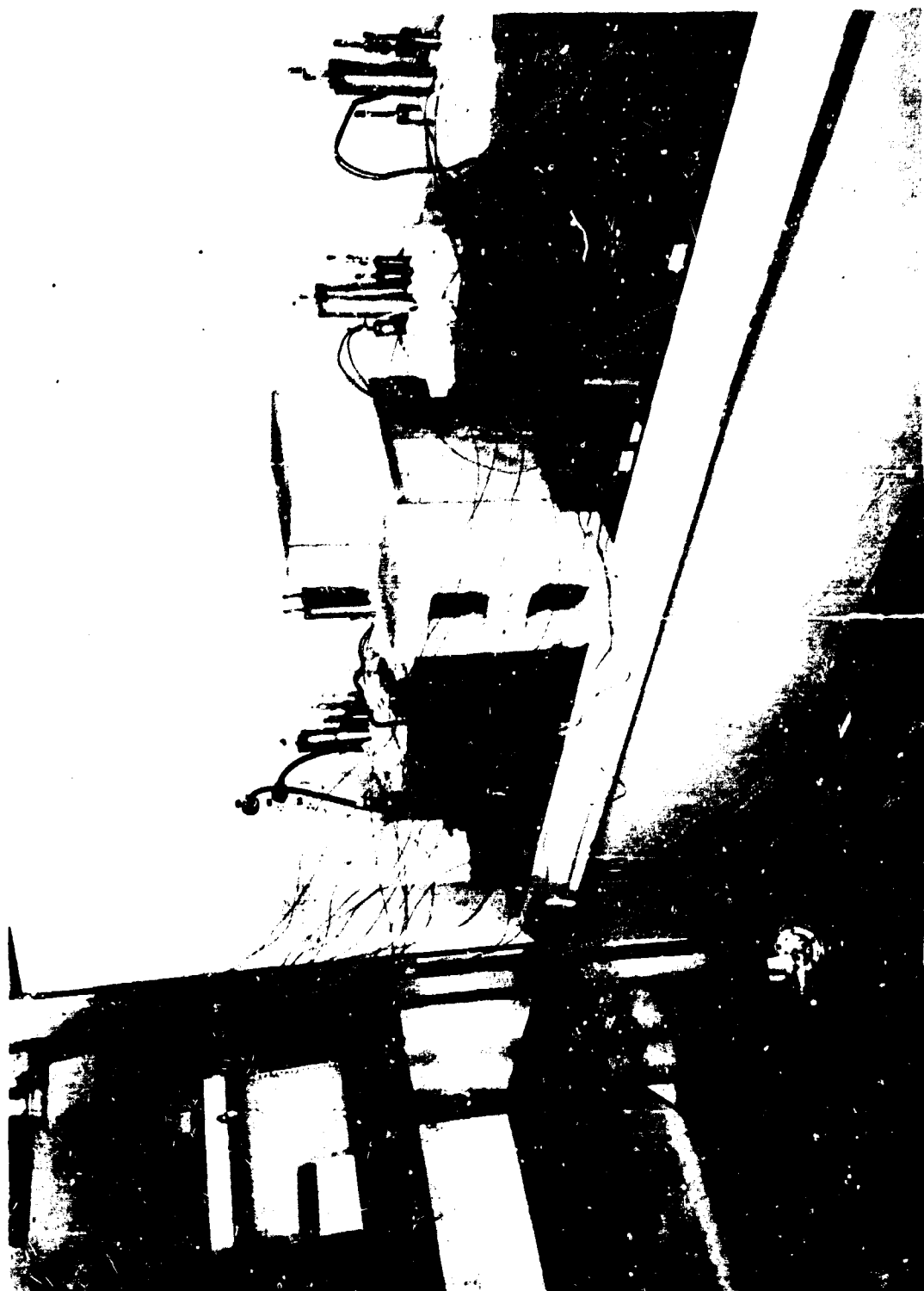
Figure 56. Test Capsule Operation Configuration
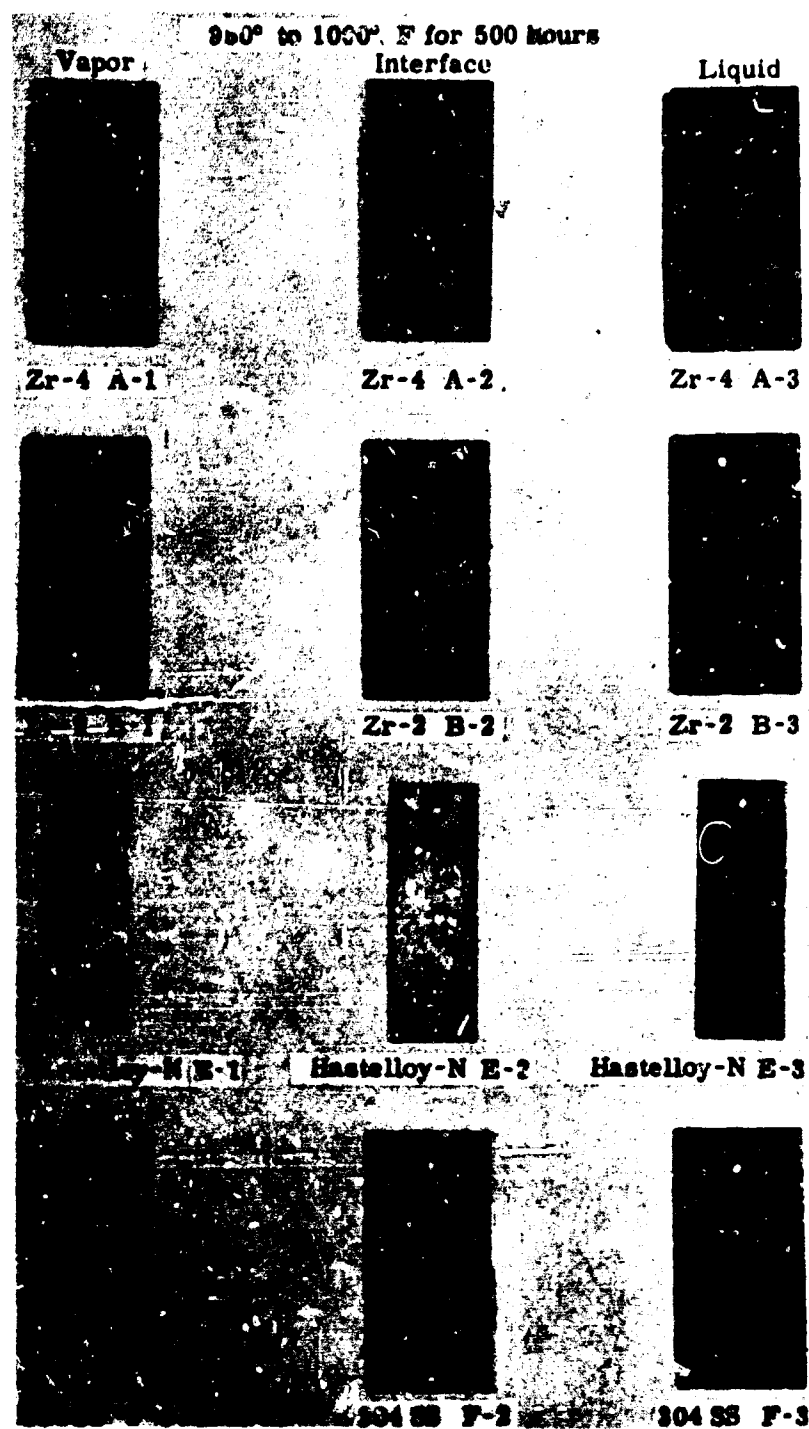
Figure 57. Corrosion Specimens (P_4S_3 + 5 Percent P Environment)
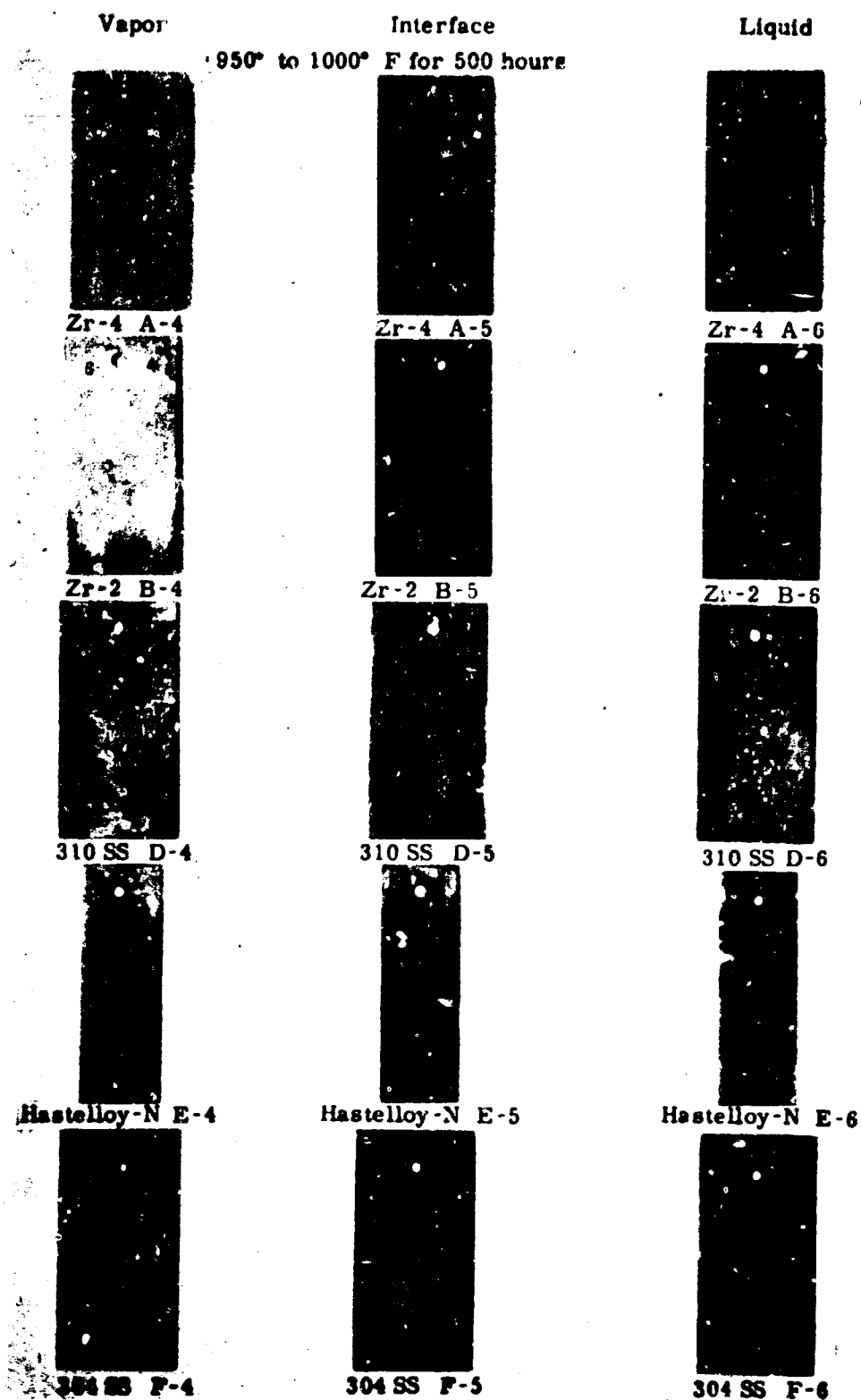
Figure 58. Corrosion Specimens (N_4S_3 + 5 Percent S Environment)

Figure 59. Corrosion Specimens (P_4S_3 Environment)
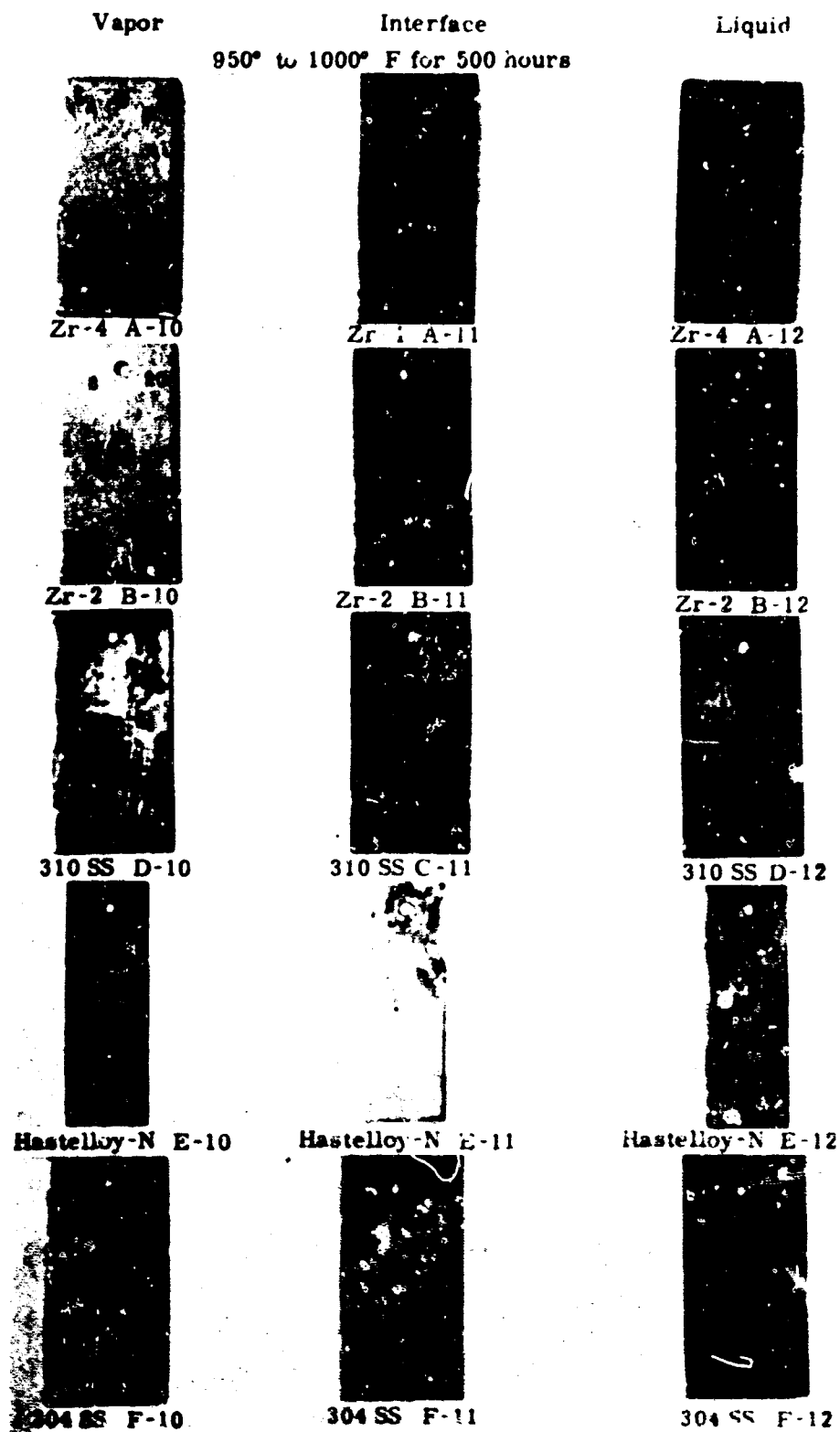
Figure 60. Corrosion Specimens (P_4S_3 + 1 Percent S Environment)
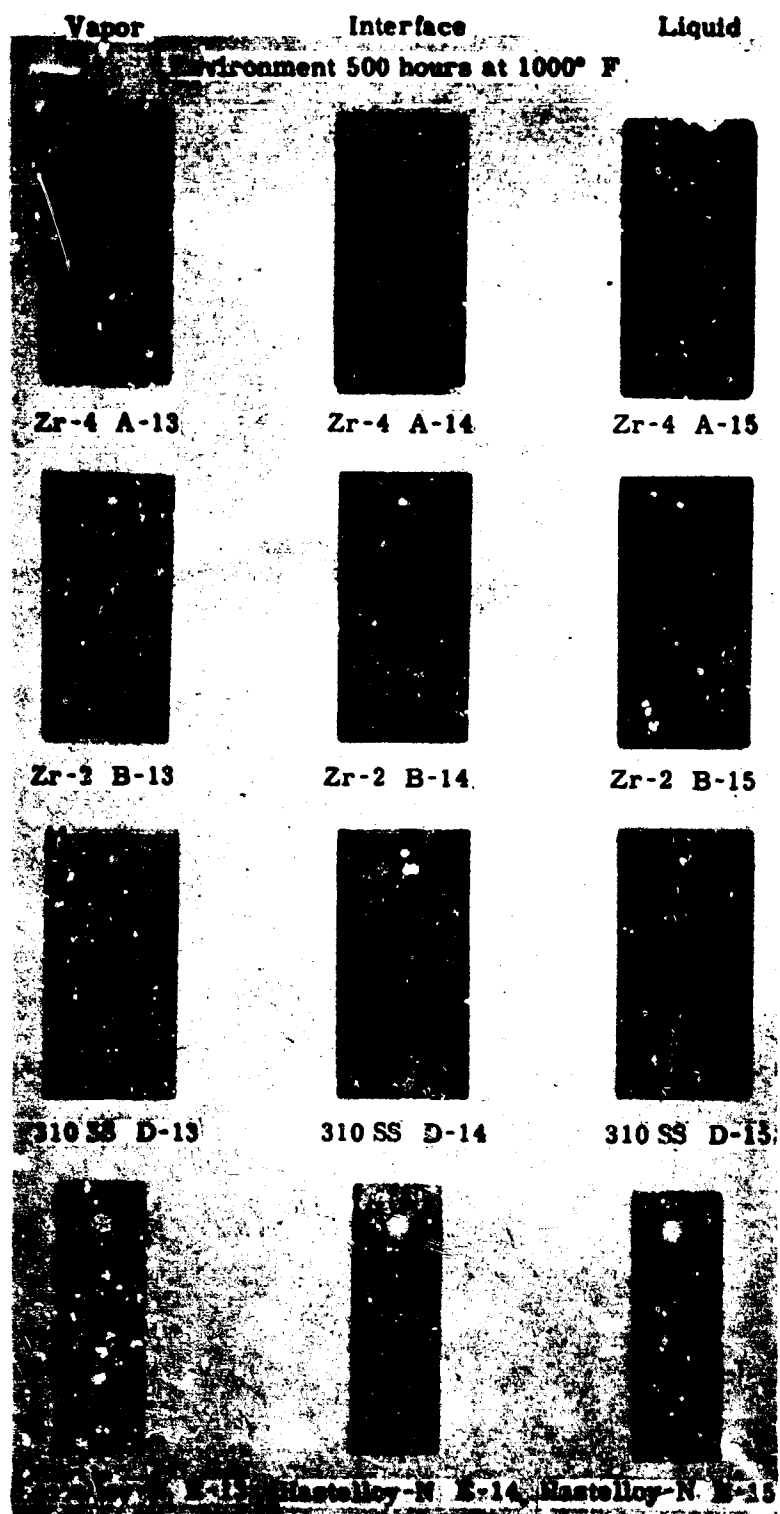
Figure 61. Corrosion Specimens (P_4S_2 + Chlorine Gas Environment)
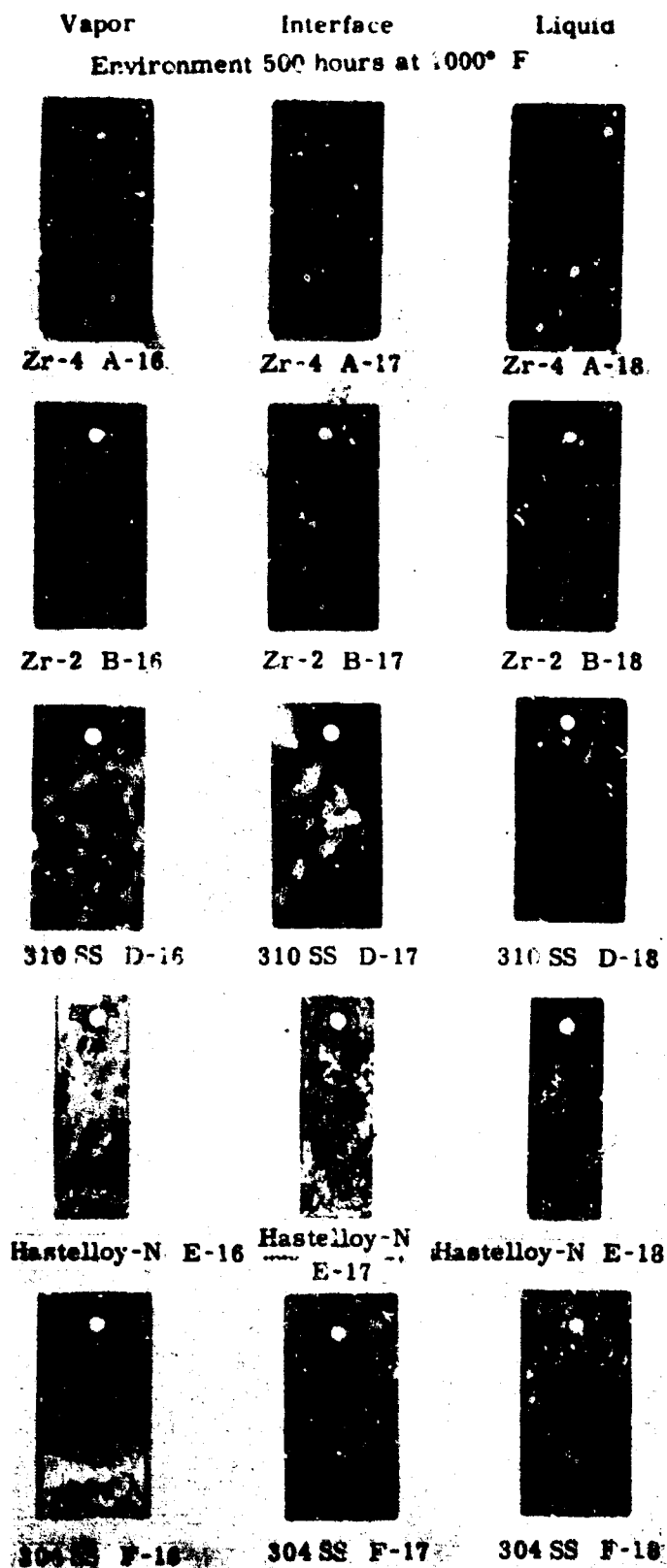
Figure 62. Corrosion Specimens (P_4S_3 + 5 Percent S + Chlorine Gas Environment)

Figure 63. Corrosion Specimens (P_4S_9 + Chlorine Gas and P_4S_7, 5 Percent P Environment)

b. Visual Inspection of Test Samples

(1) Zircaloy-4

This material showed excellent performance in all environments tested. X-ray diffraction of the surface after test indicated the presence of an adherent zirconium sulfide layer. The samples immersed in the liquid and at the interface showed the greatest tendency to form this barrier.

In no case was spalling, pitting or cracking of the material noted. Further, the presence of 5 ppm chlorine had no adverse effects on the material.

(2) Zircaloy-2

When tested in unchlorinated P_4S_3, this material displayed the same corrosion resistant characteristics as Zircaloy-4. Visual examination indicated that the material was susceptible to some uniform corrosion prior to the formation of the zirconium sulfide barrier which was present on all samples. However, the samples exposed to P_4S_3 and chlorine developed a nonadherent zirconium sulfide layer, the cause of which is unknown at present.

(3) Hastelloy-N

Although the gross corrosion rates in the nonchlorine bearing environments are not large, a spalling type of attack was noted on several samples (figure 57--Hastelloy-N E-6; figure 60--Hastelloy-N E-11). The material showed good resistance in the P_4S_3 + 1%S media and in both P_4S_3-chlorine environments. Selective pitting and cracking or intergranular attack were not noted either visually or by metallographic examination.

(4) Type 310 stainless steel

The specimens tested exhibited significant corrosion in all environments with the greatest attack occurring in the liquid phase samples. The mode of attack was one of erosion with possibly some exfoliation occurring during test. The rate of attack was lowest in stoichiometric P_4S_3. The introduction of five percent excess sulfur or phosphorus yielded accelerated attack in the liquid phase.

(5) Type 304 stainless steel

This material displayed similar corrosion properties to those mentioned for Type 310 material, although somewhat greater susceptibility was noted. Again, the samples tested in stoichiometric P_4S_3 exhibited the least corrosion. When

tested in stoichiometric P_4S_3 + Cl and P_4S_3 + 5%S + Cl. the samples in the liquid phase formed a thin, nonadherent scale. Samples of this scale submitted for analysis by X-ray diffraction indicate the presence of nickel and iron oxide. Chlorides were not detected.

c. Quantitative Evaluation of Test Results

The weight changes incurred by all corrosion specimens are presented in tables XXIV to XXIX. Normalization to the sample area, however, is not directly applicable for the Zircaloy pieces since considerable surface roughness existed prior to testing. (It is estimated that about a 30 to 40 percent effective area increase was present.) For comparison purposes, the liquid and vapor phase data are plotted in figure 64. The interface sample data are omitted because of uncertainties in liquid level position for the various capsules.

(1) Zircaloy

The values for liquid phase sulfide film buildup on Zircaloy agree well with predictions made from previous data (reference 12). The empirical formula in the referenced document, $\dot{w} = ae^{bT-ct}$, yields about 40 mg/dm^2 for a 500-hour test at 1000° F. The average observed value of nearly 60 mg/dm^2 is actually about 45 mg/dm^2 when corrections for surface roughness are made.

In accordance with previous tests, the vapor phase specimens experienced extremely small weight change.

(2) Stainless steel

The steel samples experienced relatively large weight losses when exposed to the liquid Theon environment. The absence of an adherent protective sulfide layer caused changes of 200 to 300 mg/dm^2 for stoichiometric or excess sulfur conditions. The presence of chlorine appeared to accelerate the corrosion. However, uncertainty in the amount of chlorine added to the steel capsules prevents quantitative estimation of the effect.

It is interesting to note that the vapor phase specimens showed very little change. Further tests are necessary to assure reproducibility of this behavior, but indications of applicability to the vapor region of the TURPS system arise from this result.

Table XXIV

Static Corrosion Test Results--
P_4S_3 + 5%P (500 hours at 1000° F)

Material	Weights (gm)		Change	Area of sample (in.²)	Corrosion (mg/dm²)	Position
	Original	After test				
Zircaloy-4 A-1	15.3637	15.3638	+0.0001	2.862	0.54	V
Zircaloy-4 A-2	15.3475	15.3477	+0.0002	2.848	1.1	I
Zircaloy-4 A-3	15.3211	15.3410	+0.0199	2.837	110.	L
Zircaloy-2 B-1	7.4803	7.4812	+0.0009	2.560	5.4	V
Zircaloy-2 B-2	7.4538	7.4552	+0.0014	2.550	8.5	I
Zircaloy-2 B-3	7.5026	7.5148	+0.0122	2.546	74.	L
Type 310 SS D-1	5.8410	5.8423	+0.0013	2.476	6.1	V
Type 310 SS D-2	5.8720	5.8505	-0.0115	2.492	-76.	I
Type 310 SS D-3	5.8170	5.6823	-0.1347	2.574	-810.	L
Hastelloy-N E-1	4.4474	4.4467	-0.0007	1.732	-6.3	V
Hastelloy-N E-2	4.4841	4.4835	-0.0006	1.746	-5.3	I
Hastelloy-N E-3	4.3283	4.3296	+0.0013	1.690	12.	L
Type 304 SS F-1	5.2430	5.2398	-0.0032	2.438	-20.	V
Type 304 SS F-2	5.3857	5.3852	-0.0005	2.498	-3.1	I
Type 304 SS F-3	5.2736	5.2369	-0.0367	2.448	-230.	L

V = Vapor   I = Interface   L = Liquid

Table XXV

Static Corrosion Test Results--
100% P_4S_3 (500 hours at 100° F)

Material	Weights (gm) Original	After test	Change	Area of sample (in.²)	Corrosion (mg/dm²)	Position
Zircaloy-4 A-7	15.3669	15.3684	+0.0015	2.858	8.1	V
Zircaloy-4 A-8	15.4472	15.4529	+0.0057	2.836	31.	I
Zircaloy-4 A-9	15.4301	15.4121	-0.0180	2.832	-98.	L
Zircaloy-2 B-7	7.3178	7.3089	-0.0089	2.546	-54.	V
Zircaloy-2 B-8	7.2931	7.2936	+0.0005	2.554	3.0	I
Zircaloy-2 B-9	7.4814	7.4934	+0.0120	2.560	73.	L
Type 310 SS D-7	6.0155	6.0135	-0.0020	2.502	-12.	V
Type 310 SS D-8	6.0048	6.0040	-0.0008	2.508	-4.9	I
Type 310 SS D-9	6.0662	6.0541	-0.0121	2.532	-74.	L
Hastelloy-N E-7	4.3267	4.3263	-0.0004	1.690	-3.7	V
Hastelloy-N E-8	4.3144	4.3144	--	1.692	--	I
Hastelloy-N E-9	4.4703	4.4701	-0.0002	1.744	-1.8	L
Type 304 SS F-7	5.2910	5.2892	-0.0018	2.454	-11.	V
Type 304 SS F-8	5.2441	5.2434	-0.0007	2.440	-4.4	I
Type 304 SS F-9	5.3096	5.2968	-0.0128	2.460	-81.	L

V = Vapor   I = Interface   L = Liquid

Table XXVI

Static Corrosion Test Results--
P_4S_3 + 1% S (500 hours at 1000° F)

Material	Weights (gm) Original	After test	Change	Area of sample (in.²)	Corrosion (mg/dm²)	Position
Zircaloy-4 A-10	15.8994	15.9004	+0.0010	2.860	5.4	V
Zircaloy-4 A-11	16.4158	16.4210	+0.0052	2.836	28.	I
Zircaloy-4 A-12	15.4333	15.4440	+0.0107	2.826	59.	L
Zircaloy-2 B-10	7.4673	7.4703	+0.0030	2.552	18.	V
Zircaloy-2 B-11	7.5705	7.5755	+0.0050	2.558	30.	I
Zircaloy-2 B-12	7.4945	7.5114	+0.0169	2.562	102.	L
Type 310 SS D-10	5.9591	5.9603	+0.0012	2.476	7.5	V
Type 310 SS D-11	5.9505	5.9339	-0.0166	2.476	-104.	I
Type 310 SS D-12	5.8547	5.8149	-0.0398	2.468	-250.	L
Hastelloy-N E-10	4.3039	4.3159	+0.0120	1.662	112.	V
Hastelloy-N E-11	4.4052	4.3997	-0.0055	1.716	-49.	I
Hastelloy-N E-12	4.4763	4.4813	+0.0050	1.736	44.	L
Type 304 SS F-10	5.2572	5.2507	-0.0065	2.440	-41.	V
Type 304 SS F-11	5.3855	5.3680	-0.0175	2.498	-110.	I
Type 304 SS F-12	5.3217	5.2732	-0.0485	2.476	-300.	L

V = Vapor   I = Interface   L = Liquid

Table XXVII

Static Corrosion Test Results--
P_4S_3 + 5%S (500 hours at 1000° F)

Material	Weights (gm)			Area of sample	Corrosion	Position
	Original	After test	Change	(in.^{2})	(mg/dm^2)	
Zircaloy-4 A-4	15.3349	15.3239	-0.0110	2.824	-60.	V
Zircaloy-4 A-5	15.1862	15.1992	+0.0130	2.831	71.	I
Zircaloy-4 A-6	15.4663	15.4785	+0.0122	2.816	67.	L
Zircaloy-2 B-4	7.5115	7.5087	-0.0028	2.560	-17.	V
Zircaloy-2 B-5	7.4641	7.4508	-0.0133	2.562	-80.	I
Zircaloy-2 B-6	7.3220	7.3280	+0.0060	2.550	36.	L
Type 310 SS D-4	6.0340	6.0315	-0.0025	2.514	-15.	V
Type 310 SS D-5	5.9322	5.9020	-0.0302	2.476	-190.	I
Type 310 SS D-6	5.9313	5.9367	+0.0054	2.484	34.	L
Hastelloy-N E-4	4.3711	4.3708	-0.0003	1.704	-2.7	V
Hastelloy-N E-5	4.3269	4.3305	+0.0036	1.694	33.	I
Hastelloy-N E-6	4.3433	4.3228	-0.0205	1.698	-190.	L
Type 304 SS F-4	5.3171	5.3300	+0.0129	2.466	81.	V
Type 304 SS F-5	5.3880	5.3349	-0.0531	2.496	-330.	I
Type 304 SS F-6	5.2810	5.2493	-0.0317	2.454	-200.	L

V = Vapor   I = Interface   L = Liquid

Table XXVIII

Static Corrosion Test Results--
100% P_4S_3 + Cl_2 (500 hours at 1000° F)

Material	Weights (gm)		Change	Area of sample (in.^{2})	Corrosion (mg/dm^2)	Position
	Original	After test				
Zircaloy-4 A-13	15.5874	15.5881	+0.0007	2.860	3.8	V
Zircaloy-4 A-14	15.5912	15.5923	+0.0011	2.838	6.0	I
Zircaloy-4 A-15	15.4187	15.4215	+0.0028	2.834	15.	L
Zircaloy-2 B-13	6.8950	6.8960	+0.0010	2.546	6.1	V
Zircaloy-2 B-14	7.4424	7.4421	-0.0003	2.568	-1.8	I
Zircaloy-2 B-15	7.5834	7.6086	+0.0252	2.566	150.	L
Type 310 SS D-13	5.8440	5.8406	-0.0034	2.468	-21.	V
Type 310 SS D-14	5.9437	5.9442	+0.0005	2.490	3.1	I
Type 310 SS D-15	6.0362	5.0214	-0.0148	2.5.8	-91.	L
Hastelloy-N E-13	4.2720	4.2739	+0.0019	1.690	17.	V
Hastelloy-N E-14	4.2670	4.2685	+0.0015	1.686	14.	I
Hastelloy-N E-15	4.2770	4.2794	+0.0024	1.698	22.	L
Type 304 SS F-13	5.3720	5.3621	-0.0099	2.496	-61.	V
Type 304 SS F-14	5.2483	5.2260	-0.0223	2.440	-140.	I
Type 304 SS F-15	5.2827	5.2037	-0.0760	2.454	-480.	L

V = Vapor   I = Interface   L = Liquid

Table XXIX

Static Corrosion Test Results--

$F_4S_3 + 5\%S + Cl_2$ (500 hours at 1000° F)

Material	Weights (gm)			Area of sample	Corrosion	Position
	Original	After test	Change	(in.^{2})	(mg/dm^2)	
Zircaloy-4 A-16	15.6973	15.7037	+0.0064	2.896	34.	V
Zircaloy-4 A-17	15.4875	15.4925	+0.0050	2.874	27.	I
Zircaloy-4 A-18	16.2970	16.3046	+0.0076	2.940	40.	L
Zircaloy-2 B-16	7.2722	7.2761	+0.0039	2.564	23.	V
Zircaloy-2 B-17	7.3896	7.3933	+0.0037	2.558	22.	I
Zircaloy-2 B-18	7.4937	7.5629	+0.0692	2.568	420.	L
Type 310 SS D-16	5.8783	5.8819	+0.0036	2.470	22.	V
Type 310 SS D-17	5.8602	5.8626	+0.0024	2.470	15.	I
Type 310 SS D-18	5.9173	5.8292	-0.0881	2.490	-550.	L
Hastelloy-N E-16	4.2947	-4.3024	+0.0077	1.686	71.	V
Hastelloy-N E-17	4.2851	4.2940	+0.0089	1.684	82.	I
Hastelloy-N E-18	4.2494	4.2795	+0.0301	1.680	280.	L
Type 304 SS F-16	5.3390	5.3394	+0.0004	2.498	2.5	V
Type 304 SS F-17	5.3463	5.3346	-0.0117	2.504	-72.	I
Type 304 SS F-18	5.2414	5.0105	-0.2309	2.450	-1460.	L

V = Vapor   I = Interface   L = Liquid
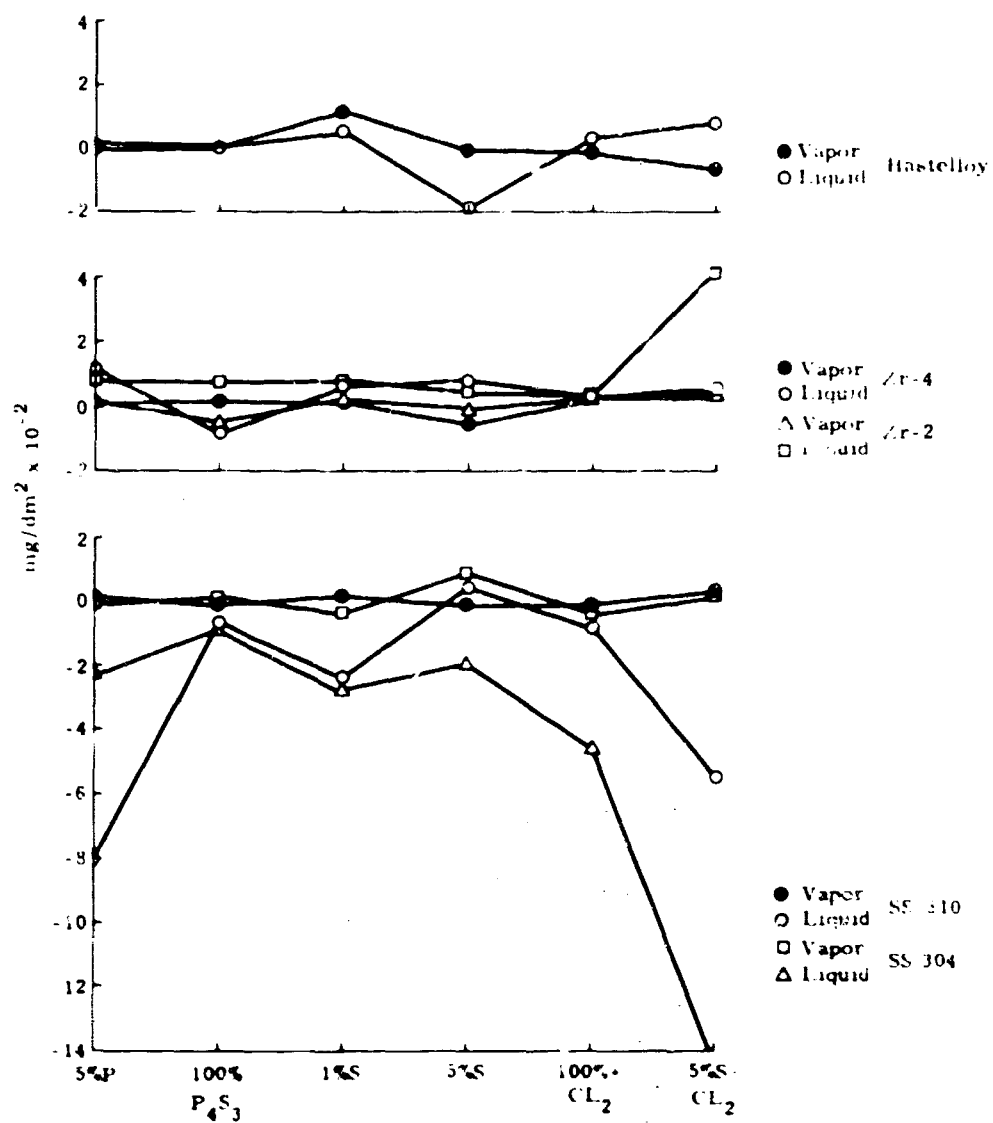
Figure 64. Static Corrosion Test Liquid and Vapor Phase Data

(3) Hastelloy

The Hastelloy specimens showed lower average corrosion rates than the steel specimens, but, as indicated previously, irregular spalling was observed. Hence, despite lower observed total weight change, local attack may be most significant.

3. Dynamic Corrosion Test

The static corrosion test established Zircaloy as the most promising structural material for P_4S_3 containment. The primary aim of the present effort was to evaluate the performance of Zircaloy in a long-term test with P_4S_3 conditions approximating TURPS operation. To this end, the design and manufacture of a dynamic corrosion test apparatus capable of 4500 hours operation was completed. To aid the study of Zircaloy performance, an additional short-term investigation was conducted to explore differences of behavior between Zircaloys-2 and -4 and effects of pretreatment of the Zircaloy surfaces.

a. Surface Treatment Investigation of Zircaloy-2 and Zircaloy-4

The effects of surface preparation on Zircaloys-2 and -4 were studied by exposing variously treated test coupons to P_4S_3 at 1000° F for periods of 170 and 540 hours. All specimens were degreased in Oakite and chemically cleaned in a 10 percent HNO_3-10 percent HF solution. In addition, air and vacuum firing operations were performed on selected samples. Subsequent to the initial preparation, coupons of each Zircaloy and treatment type were presulfided for 24 hours at 1000° F in pure sulfur and in pure P_4S_3. Following the presulfiding, immersion of the specimens in P_4S_3 at 1000° F was conducted. In order to minimize container reaction effects, the exposure was conducted in thoroughly cleaned Vycor capsules.

Study of the test coupons and P_4S_3, after the desired exposure, was made by weight change determination, metallographic observation, X-ray diffraction and emission spectroscopy. The following significant conclusions were drawn from this investigation:

(1) No difference was noted between the behavior of Zircaloy 2 and Zircaloy-4.

(2) Pretreatment of the Zircaloy by air firing, vacuum firing or chemically cleaning alone did not affect the subsequent compatibility with P_4S_3.

(3) Presulfiding of Zircaloy with either P_4S_3 or sulfur decreased the subsequent contamination of P_4S_3. The degree of discoloration of P_4S_3 for the 170- and 540-hour tests was much less than that observed in the initial presulfiding in P_4S_3.

(4) There was no difference in the behavior between samples pre-sulfided with sulfur or P_4S_3.

(5) Indications of limited solubility of the presulfided layer during sub-sequent P_4S_3 exposure were observed. This conclusion results from the obser-vation that the 170-hour specimers showed small weight reductions whereas the 540-hour specimens incurred weight increases.

b. Dynamic Corrosion Test Apparatus Design

A detailed design of a dynamic corrosion test loop was prepared. Photo-graphs of the completed loop are shown in figures 65 through 67. Figure 65 presents the bare Zircaloy structure while figure 66 illustrates the installation of the main heaters, guard heaters and thermocouples. Figure 67 contains the complete assembly with insulation attached prior to insertion into the inert atmosphere outer container.

To assure proper fabrication of the Zircaloy loop, extensive radiographs of welds and leak check tests were performed. Figure 68 shows the radio-graph of the high velocity test section and two thermocouple wells. It should be noted that the one-half of the high velocity section length was constructed of Zircaloy-2 and the other half of Zircaloy-4. This enabled further evalua-tion of the relative performance of the Zircaloys.

c. Dynamic Corrosion Test Operation

Because the surface treatment test results indicated that presulfiding of Zircaloy minimizes the reaction with P_4S_3, the test apparatus was operated for approximately two days with an initial loading of P_4S_3, plus one weight percent of excess sulfur. The initial heatup proceeded smoothly with all heaters and thermocouples functioning satisfactorily. Small valve leaks in the pressure gage and fill lines were remedied by replacement with steel bellows-type valves capable of withstanding higher temperatures for longer periods of time. The test apparatus, during this presulfiding period, vented with ease and drained in a clean and straightforward manner. No attempts were made to obtain accurate heat balance or flow determinations, the objec-tive being short-term operation at 950° to 1000° F with all Zircaloy surfaces in contact with P_4S_3 liquid or vapor. Following the draining of the apparatus,

Figure 65. Zircaloy Corrosion Test Apparatus Prior to installation of Electrical Components

Figure 66. Zircaloy Corrosion Test Apparatus with Heaters and Thermocouples Installed
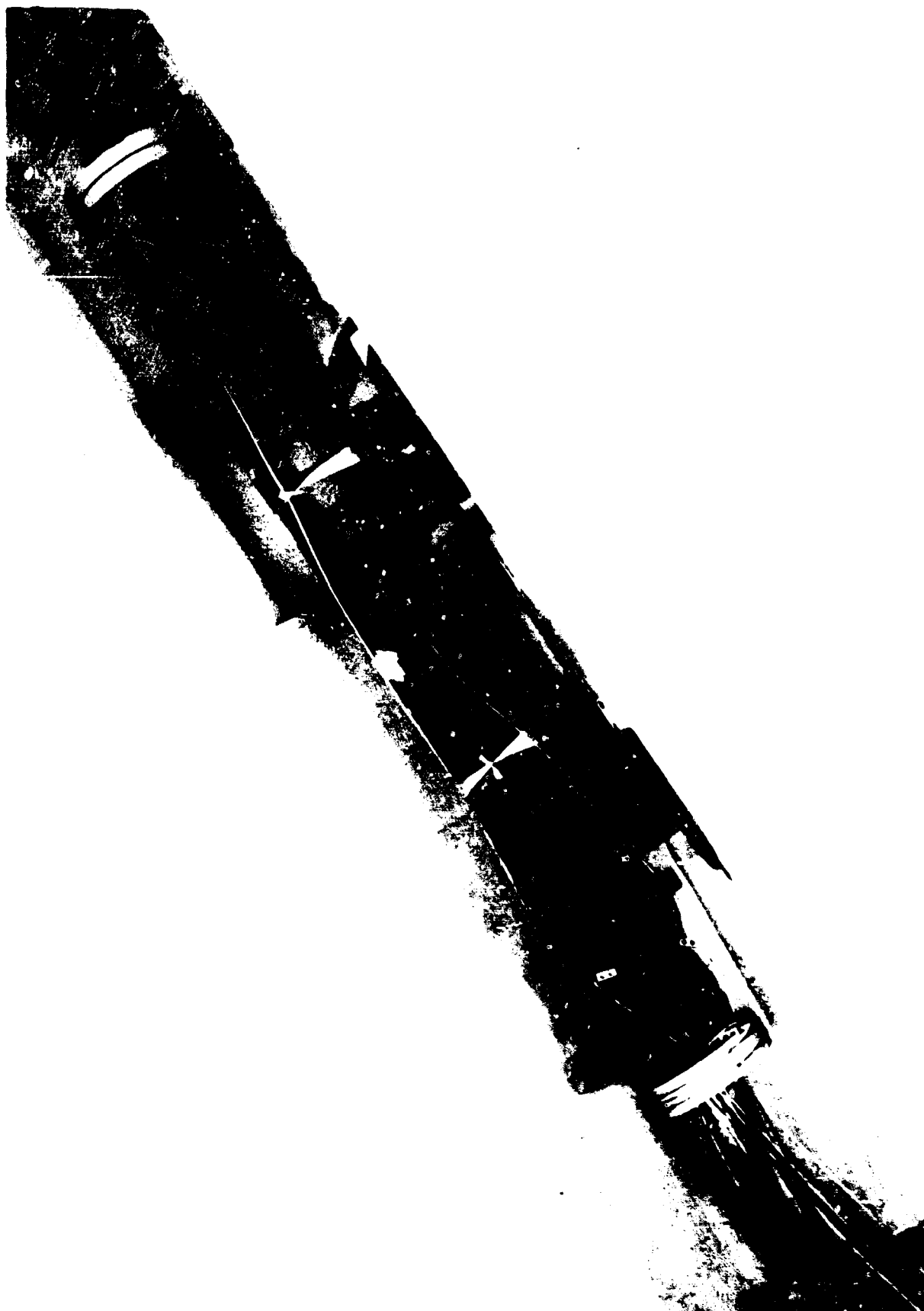
Figure 57. Zircaloy Corrosion Test Apparatus Ready for Installation in Outer Container

it was recharged with fresh stoichiometric P_4S_3. When venting was attempted,
it was immediately evident that the vent lines were clogged with condensed
material. Internal pressure measurements indicated the presence of non-
condensibles, as pressure readings were higher than anticipated from the known
P_4S_3 vapor pressure-temperature relationship. Inspection of the vent line
disclosed the presence of red phosphorus.

Because red phosphorus (melting point 500° C) could not be melted in the
vent line, physical removal by coring with a drill was attempted. Although
most of the line was cleared in this manner, a weld penetration caused breakage
of the drill bit. The drill bit was firmly lodged in the line, and attempts at
removal were unsuccessful. It was concluded that removal of the bit necessi-
tated removing the outer container top flange and cutting and re-welding the
vent line. In addition, disassembly and rewiring of thermocouple and heater
circuits was required. At this point, operations were suspended because of
funding limitations.

Failure of the apparatus operation is attributed to the presence of free
phosphorus in the P_4S_3. Initially, the free phosphorus appears in the gaseous
or white phosphorus form, but at the conditions of this test, transformation to
red phosphorus occurs rapidly. The red phosphorus is liquid at the operating
test temperature (~550° C) and would not clog the passages in the apparatus.
However, the vent line heating was designed only for melting P_4S_3 (plus some
margin, i.e., 500° F) and the vent line could not be freed. Hence, removal
of noncondensibles and test operation could not proceed.

d. Conclusions and Recommendations

The decision to operate the test apparatus with stoichiometric P_4S_3 appears
to have been most unfortunate, since the indications are that the presence of
one percent excess sulfur would have suppressed the free phosphorus. There
has been no indication from prior experimental work that P_4S_3 plus one percent
excess sulfur differs in corrosive properties from the stoichiometric
material. Moreover, computations indicate that the presence of a small
quantity of excess sulfur substantially increases the radiation resistance
of P_4S_3.

1 High velocity
  test section

2 Thermocouple well

3 Thermocouple well
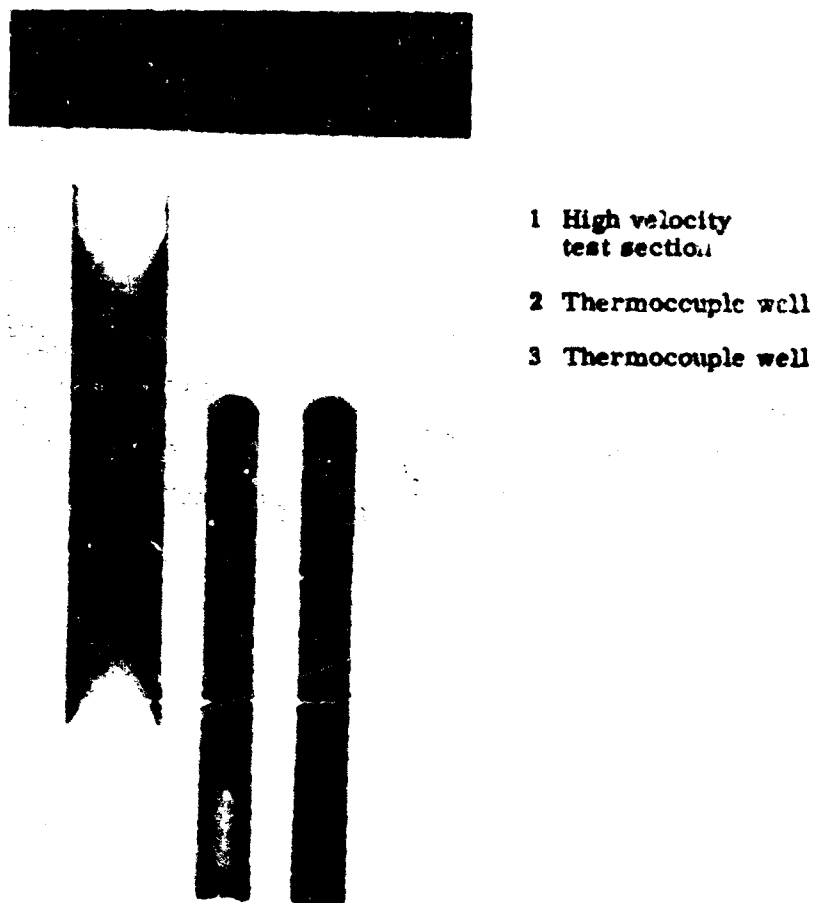
Figure 68. Radiographs of High Velocity Venturi Test Section and Two Thermocouple Wells

Resumption of the test can be accomplished without major changes to the apparatus. Some changes in the fill system and vent line configuration should be made to minimize susceptibility to clogging during normal venting; venting, of course, being required to blow off the argon blanket used during the fill process. The significant finding is that the test should have used P_4S_3 with some small fraction of excess sulfur. Use has been made here of the terms "corrosion" and "radiation effects" but, in fact, the P_4S_3 work to date indicates that P_4S_3 has negligible corrosive effect on presulfided Zircaloy and that the radiation effect on P_4S_3 plus excess sulfur is also negligible.

APPENDIX I

APPROXIMATION OF AN INFINITE SERIES

Evaluation of $\displaystyle\sum_{n=1}^{\infty} \frac{e^{-n^2\alpha^2}}{n^2}$ for $\alpha^2 > 0$. In general, an infinite series of the

form $\displaystyle\sum_{n=1}^{\infty} f_n(n)$ can be approximated by a finite sum plus an error term.

Letting $f(x)$ be the continuous function which agrees with $f_n(n)$ at the integer,
then a good approximation is given by

$$\sum_{n=1}^{\infty} f_n(n) = \sum_{n=1}^{\ell-1} f_n(n) + \frac{1}{2} f_n(\ell) + \int_{\ell}^{\infty} f(x)\,dx$$

Derivation of this formula is straightforward from figure 69. Clearly, the sum

of the series is bounded between $\displaystyle\int_{1}^{\infty} f(x)\,dx$ and $\displaystyle\int_{1}^{\infty} f(x-1)\,dx$ and as $A_1 \approx A_1'$,
$A_2 \approx A_2'$, etc., then

$$\sum_{n=1}^{\infty} f_n(n) - \int_{1}^{\infty} f(x)\,dx \approx \int_{2}^{\infty} f(x-1)\,dx - \sum_{2}^{\infty} f_n(n)$$

$$\sum_{n=1}^{\infty} f_n(n) + \sum_{2}^{\infty} f_n(n) \approx \int_{1}^{\infty} f(x)\,dx + \int_{2}^{\infty} f(x-1)\,dx$$

$$2\sum_{n=1}^{\infty} f_n(n) - f_n(1) \approx 2\int_{1}^{\infty} f(x)\,dx$$

$$\sum_{n=1}^{\infty} f_n(n) \approx \frac{f_n(1)}{2} + \int_{1}^{\infty} f(x)\,dx$$

from equating A_1 to A_1' and, as the approximation of $A_{\ell-1}' \approx A_{\ell-1}$ becomes much
better as $\ell \to \infty$ then the approximation
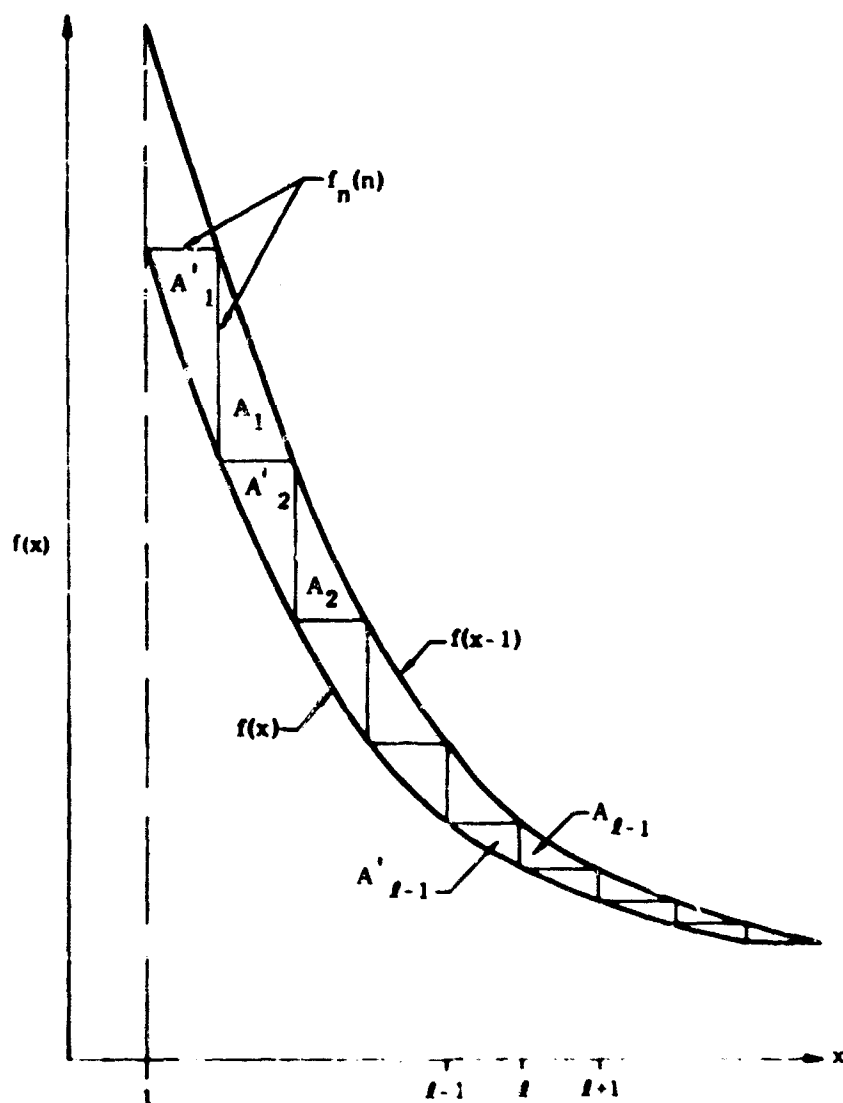
Figure 69. Approximate Evaluation of Series $\displaystyle\sum_{n=1}^{\infty} f_n(n)$

$$\sum_{n=1}^{\infty} f_n(n) = \sum_{n=1}^{l-1} f_n(n) + \frac{1}{2} f(l) + \int_{l}^{\infty} f(x)\,dx$$

is quite good for l large.

In the particular case of interest, the function $f_n(n)$ goes to zero so rapidly that $l = 5$ is quite adequate. It is still necessary, however, to evaluate $\int_{l}^{\infty} f(x)\,dx$ which in this case is $\int_{l}^{\infty} \dfrac{e^{-\alpha^2 x^2}}{x^2}\,dx$. The transformation $y = \alpha^2 (x^2 - l^2)$ gives

$$\int_{l}^{\infty} \frac{e^{-\alpha^2 x^2}}{x^2}\,dx = \alpha \frac{e^{-\alpha^2 l^2}}{2} \int_{0}^{\infty} \frac{e^{-y}\,dy}{(y + \alpha^2 l^2)^{3/2}}$$

The integral term is calculated by Gaussian quadrature with weight function e^{-y} on the interval $(0, \infty)$. The seven-point quadrature formula is used as the function $(y + \alpha^2 l^2)^{-3/2}$ goes to zero quite rapidly.

This approximation was used in calculating $d\bar{c}/dt$ for the given analytic surface concentrations used in checking the earlier HYDRA code and excellent agreement was obtained.

This page intentionally left blank.

APPENDIX II

FORTRAN LISTING OF HYDRA II

```
$       FORTRAN STAB.DECK.LSTIN
$       INCODE  IBMF
CHYDRA
C    THE NEW HYDRA//THE TWO HEADED MONSTER//
        COMMON SIG.EPSK.XM.DEN1.DEN2.C2.CON.SRAT .EPS
        DIMENSION SIG(2).XM(2).EPSK(2).CON(2)
        DIMENSION XMATA(30.30).BX(30).XMAT(30.30).YMUE(11)
        DIMENSION XLAM(101.11).PSI(2  .11).V(    11).T(2  .11).C(2  .11)
     1      .Q(30))          .P(2  .12).DCBAR(11).FH( 2 .12).PI(2  .12).
     2             TP(101).ESSN(11).DOFT(11).SEE(101.11).CAY1(11).
     3             CAY2(11).DAFT(101.11).CEE(4.11).SA(4).SB(4)
        EQUIVALENCE (SEE(1).XMATA(1))
C    MAX ZONES IS 10
        DATA PIE.SA.SB.XMH.R/3.1415927.-3.8415.38.6433.-34.2639.
     1  9.2821.-31298.2.23574.1.-6028..0..2.016.8.314E7/
        HCON=1.15*1.987*4.186E10
        SIG=8.4972
        EPSK=38.
        XM=2.016
        ROMH=R/XMH
        DCBAR=0.
C    GET INPUT
23      READ            ( 5.101)NZONES.NTAB.INPT
        READ            (5.100)XA.XB.DP.FD.DEPTH.EPS.FF.TMAX.DELTAT.
     1  TAMB.TZERO.FI.RHOS.CESS.AREA.XKL.(ESSN(J).J=1.NZONES)
        READ            (5.100)SIGI.EPSKI.XMI
        READ            (5.100) (TP(J).Q(J  ) .J=1.NTAB)
C DEMAX LE ZERO KEEPS DELTAT FIXED
C    WHEN ROMANV LESS THAN ZERO KEEP PERCENTAGE OF INLET INERTS CONSTANT
        READ(5.100) PIV1.PIV2.QEX.ROMANV.DMAX.DMIN
        WRITE           (6.105)
105     FORMAT(12H.HYDRA INPUT)
        WRITE           (6.106)
106     FORMAT(24H0PRESSURE TABLE (P.VS.T))
        WRITE           (6.107)(Q(J  ) .TP(J).J=1.NTAB)
107     FORMAT(1H 2E15.6)
        WRITE           (6.108)
108     FORMAT(15H0INERT GAS DATA)
        BI=100.*PIV1/Q(1)
        IF(ROMANV.LT.0.) BI=100.*FI
        WRITE           (6.109)BI.SIGI.EPSKI.XMI
109     FORMAT(23H FRACTION OF INERT GAS=F10.6.7HPERCENT.
     1  2X.7H.SIGMA=F5.3.2X.
     1   7H.EPS/K=F4.1.2X.14H.MOLECULAR WT=F6.2)
        WRITE(6.127) PIV1.PIV2.QEX.ROMANV
127     FORMAT(6H0PIV1=E15.6.2X.6H.PIV2= E15.6.2X.3H.Q= F7.5.2X.
     1  8H.VOLUMN= E15.6)
        PIV2=PIV2*6.8947E4
        WRITE           (6.110)
110     FORMAT(16H0TIME PARAMETERS)
        WRITE           (6.111)TMAX.DELTAT.DMAX
111     FORMAT(10H MAX TIME=F5.2. 4H.DT=F6.3.6H.DMAX= E15.6)
        WRITE           (6.112)
112     FORMAT(32H0DIFFUSION COEFFICIENT CONSTANTS)
        WRITE           (6.113)XA.XB
113     FORMAT(3H A=E15.7.2X.3H.B=E15.7)
        WRITE           (6.114)
114     FORMAT(27H0REMAINING INPUT QUANTITIES)
        WRITE           (6.115)NZONES.DEPTH.EPS.TZERO.AREA
115     FORMAT(17H0NUMBER OF ZONES=I2.2X.14HLENGTH OF BED=F5.2.2X.
     1  14HVOID FRACTION=F4.2.2X.13HINITIAL TEMP=F9.4.2X.17HX-SECTIONAL
     2 AREA=F6.3)
```

148

```
C
          WRITE               (6,130)XKL,RHOS,CESS,DP,FD,FF
 130      FORMAT(17HOHEAT LOSS COEFF= E15.7,2X,5HRHOS= E15.7/
     1    6HOCESS= E15.7,2X,3HDP= E15.7,2X,3HFD= E15.7,2X,3HFF= E15.7)
          WRITE               (6,116)(J,ESSN(J),J=1,NZONES)
 116      FORMAT(3H S(I2,2H)=E15.7)
C INITIALIZATION
          SIG(2)=SIGI**2
          EPSK(2)=EPSKI
          XM(2)=XMI
          RAT=XM(2)/XM(1)
          SRAT=SQRT (RAT)
          DEN1=SQRT (8.*(1.+RAT))
          DEN2=SQRT (8.*(1.+1./RAT))
          DO40 I=1,2
 40       CON(I)=2.665E-5*SQRT (XM(I))/SIG(I)
          C2=15.*1.987/(4.*XM(2))*4.184E7
          CESS=CESS*4.186E7
          XKL=XKL*1.8E7
          TZERO=(TZERO+460.)/1.8
          TAMB =(TAMB +460.)/1.8
          XZ=NZONES
          NZONES=NZONES+1
          YMUE(NZONES)=0.
          DELX=DEPTH/XZ
          A=.5*DP*FD
          PIA=PIE**2/A**2
          NZM1=NZONES-1
          NZM2=2*NZM1
          NHZM1=3*NZM1
          NL=NZM2+1
          NZT1=NZONES+1
          DO 200 J=1,NHZM1
          DO 200 K=1,NHZM1
 200      XMAT(J,K)=0.
 401      EPSM1=EPS-1.
          EPDT=EPS/DELTAT
          D=(DP*FF*EPS/EPSM1)**2*EPS/(150.*DELX)
          DD=D/DELX
          P(1,1)=Q(1)
          PI(1,1)=Q(1)*(PIV1/Q(1))**QEX
          IF(ROMANV.LT.0.) PI(1,1)=FI*P(1,1)
          P(1,1)=P(1,1)*6.8947E4
          PI(1,1)=PI(1,1)*6.8947E4
          PH(1,1)=P(1,1)-PI(1,1)
          VIN=0.
          ROCAN=-AREA/ROMANV
          JS=2
          CALL FAZEDA(PH(1,1),TZERO,CZERO)
          WRITE(6,132) TZERO,CZERO
 132      FORMAT(14HO INITIAL TEMP= E15.7,2X,22HINITIAL CONCENTRATION=
     1    E15.7)
          EPDX=EPS*DELX
          AREX=AREA*DELX
          AREY=AREA/DELX
          ADTM=RHOS/(1.008*CZERO+91.22)*1.008
          EPSRM=EPSM1*ROMH *ADTM*6./PIE**2
          DCCON=-EPSRM*PIE**2/6.
          ASCON=-DELX*EPSM1*ADTM*AREA
          CLASS=ADTM/(RHOS*CESS)
          CLESS=-1./(RHOS*CESS*EPSM1)
          DHPCON=1./ ALOG(10.)
```
149

```
          DO 1 M=1,NZONES
          DAFT(2,M)=0.
          ESSN(M)=ESSN(M)*1.E7
          XLAM(1,M)=0.
          PSI(1,M)=CZERO
          P(1,M)=P(1,1)
          PH(1,M)=PH(1,1)
          PI(1,M)=PI(1,1)
          T(1,M)=TZERO
          C(1,M)=CZERO
1         CONTINUE
          PH(1,NZT1      )=PH(1,NZONES)
          PI(1,NZT1      )=PI(1,NZONES)
           P(1,NZT1      )= P(1,NZONES)
          TIME=DELTAT
C START TIME COUNTER
          I=2
          CSTAR=0.
          INOW=2
23        JCAP=INOW-1
          DO 28 J=JS,NTAB
          IS=J
          IF((TP(J)-TIME)*(TP(J-1)-TIME)) 30,30,28
28        CONTINUE
C    IF EXIT HERE WILL EXTRAPOLATE
30        P(I,1)=Q(IS-1)+(Q(IS)-Q(IS-1))*(TIME-TP(IS-1))/ (TP(IS)-TP(IS-1))
          JS=IS
          P(I,1)=P(I,1)*6.8947E4
          PIV2=PIV2+ROCAN*VIN*PI(I-1,1)*DELTAT
          IF(PIV2.LT.0.) PIV2=0.
          PI(I,1)=P(I,1)*(PIV2/P(I,1))**QEX
          IF(ROMANV.LT.0.) PI(I,1)=FI*P(I,1)
          PH(I,1)=P(I,1)-PI(I,1)
          LITER=0
          DO 3 J=2,NZONES
          PH(I,J)=PH(I-1,J)
          PI(I,J)=PI(I-1,J)
          PSI(I,J)=PSI(I-1,J)
          P(I,J)=PH(I,J)+PI(I,J)
3         T(I,J)=T(I-1,J)
          T(I,1)=T(I-1,1)
          PH(I,NZT1      )=PH(I-1,NZT1      )
          PI(I,NZT1      )=PI(I-1,NZT1      )
           P(I,NZT1      )= P(I-1,NZT1      )
20        DO 6 M=2,NZONES
          DOFT(M)=XA/EXP (XB/(1.987*T(I,M)))
          XLAM(INOW,M)=TIME*DOFT(M)
          DO 50 II=1,INOW
          ALPS=PIA*(XLAM(INOW,M)-XLAM(II,M))
          CALL SERVAL      (ALPS,SEE(II,M))
50        CONTINUE
6         CONTINUE
          DO 51 M=2,NZONES
          DO 57 J=1,4
57        CEE(J,M)=SA(J)+SB(J)/T(I,M)
          CSM=(SEE(INOW,M)-SEE(JCAP,M))/(XLAM(INOW,M)-XLAM(JCAP,M))
          CAY2(M)=-DOFT(M)*CSM*EPSRM
          CAY1(M)=-PSI(I-1,M)*CSM
52        DO 53 J=2,JCAP
53        CAY1(M)=CAY1(M)+(SEE(J,M)-SEE(J-1,M))*DAFT(J,M)
51        CAY1(M)=-DOFT(M)*CAY1(M)*EPSRM
          NCUT=0                        150
```

```
              ISUR=0
              IF(FI) 400,400,402
C ONLY DO WHEN CHANGE T
  400         DO 202 J=1,NZM1
  201         XMAT(J,J)=1.
              JJ=J+NZM1
  202         XMAT(JJ,JJ)=CAY2(J+1)
              GO TO 8
  402         DO 300 J=NL,NHZM1
              JJ=J-NZM2+1
  300         XMAT(J,J)=CAY2(JJ)
  8           ABSORD=0.
              DO177 M=1,NZM1
              IF(M.GE.2) GO TO 214
              TEMP=T(I,1)
              PRESH=PH(I,1)
              PRESI=PI(I,1)
              GO TO 215
  214         TEMP=.5*(T(I,M)+T(I,M+1))
              PRESH=.5*(PH(I,M)+PH(I,M+1))
              PRESI=.5*(PI(I,M)+PI(I,M+1))
  215         CALL PROP(TEMP,PRESH,PRESI,XMUM,XKBED,ISUR,IVIS)
              V(M)    =DD/XMUM
              IF(M-1) 210,210,211
  210         YMUE(1)=XMUM*DELX*T(I,1)
              V=2.*V
              GO TO 177
  211         YMUE(M)=XMUM*DELX*(T(I,M)+T(I,M+1))
  177         YMUE(M)=2.*D/YMUE(M)
              V(NZONES)=0.
              IF(FI)59,59,60
  59          CONTINUE
              DO 213 J=1,NZM1
              JJ=J+NZM1
              BX(J)=6.
              DO 212 K=1,4
  212         BX(J)=BX(J)+CEE(K,J+1)*PSI(I,J+1)**(K-1)
              BX(J)=-1.01325*10.**BX(J)
              XMAT(J,JJ)=0.
              DO 204 K=2,4
              XK=K-1
  204         XMAT(J,JJ)=XMAT(J,JJ)+XK*CEE(K,J+1)*PSI(I,J+1)**(K-2)
              XMAT(J,JJ)=BX(J)*XMAT(J,JJ)/DHPCON
              BX(J)=-BX(J)-PH(I,J+1)
  213         CONTINUE
              XMAT(NZONES,1)=(PH(I,2)*YMUE(2)+PH(I,1)*YMUE(1)+EPDT/T(I,2))
              DO 205 K=2,NZM1
              JD=NZM1+K
C   JD IS ROW NUMBER
          XMAT(JD,K)=(PH(I,K+1)*(YMUE(K+1)+YMUE(K))+EPDT/T(I,K+1))
              XMAT(JD-1,K)=-YMUE(K)*PH(I,K+1)
  205         XMAT(JD,K-1)=-YMUE(K)*PH(I,K)
              DO 206 J=1,NZM2
              DO 206 K=1,NZM2
  206         XMATA(J,K)=XMAT(J,K)
              DO 209 J=1,NZM1
              JJ=NZM1+J
              BX(JJ)=PSI(I,J+1)*CAY2(J+1)
      1                          -(.5*(YMUE(J+1)*(PH(I,J+2)**2-PH(I,J+1)**2)-
      1       YMUE(J)*(PH(I,J+1)**2-PH(I,J)**2))-CAY1(J+1)-EPDY*(PH(I,J+1)/
      2       T(I,J+1)-PH(I-1,J+1)/T(I-1,J+1)))
              BX(JJ)=-BX(JJ)
```

                                    151

```
209       CONTINUE
          BX(NZONES)=PSI(I,2)+CAY2(2)
     1                          -(.5*YMUE(2)*(PH(I,3)**2-PH(I,2)**2)-
     1    YMUE(1)*PH(I,1)*(PH(I,2)-PH(I,1))-CAY1(2)-EPDT*(PH(I,2)/T(I,2)
     2    -PH(I-1,2)/T(I-1,2)))
          BX(NZM1+1)=-BX(NZM1+1)
          CALL MATINV(XMATA,NZM2,BX)
          CONE=0.
          DO 207 J=1,NZM1
          PH(I,J+1)=PH(I,J+1)+BX(J)
          CONE=CONE+ABS (BX(J)/PH(I,J+1))
          JJ=J+NZM1
          PSI(I,J+1)=PSI(I,J+1)+BX(JJ)
          CONE=CONE+ABS (BX(JJ)/PSI(I,J+1))
207       CONTINUE
          PH(I,NZT1      )=PH(I,NZONES)
          P(I,NZT1)=PH(I,NZT1)
          NCUT=NCUT+1
          IF(NCUT-10) 66,66,62
66        IF(CONE-1.E-5) 62,62,59
60        CONTINUE
C    INERTS
          DO 305 J=1,NZM1
          JJ=J+NZM1
          JJJ=JJ+NZM1
          XMAT(J,JJ)=DHPCON/PH(I,J+1)
          XMAT(J,JJJ)=0.
          DO 302 K=2,4
          XK=K-1
302       XMAT(J,JJJ)=-XK*CEE(K,J+1)*PSI(I,J+1)**(K-2)+XMAT(J,JJJ)
          BX(J)=-DHPCON*ALOG(PH(I,J+1)/1.01325E6)
          K=J+1
          BX(KK)=-EPDT*(PH(I,K)/T(I,K)-PH(I-1,K)/T(I-1,K))-CAY1(K)-
     1    CAY2(K)*PSI(I,K)+.5*(YMUE(K)*(PH(I,K+1)+PH(I,K))*(P(I,K+1)-
     2    P(I,K))-YMUE(J)*(PH(I,K)+PH(I,J))*(P(I,K)-P(I,J)))
          DO 306 K=1,4
306       BX(J)=BX(J)+CEE(K,J+1)*PSI(I,J+1)**(K-1)
          BX(JJ)=-EPDT*(PI(I,J+1)/T(I,J+1)-PI(I-1,J+1)/T(I-1,J+1))+.5*(
     1    YMUE(J+1)*(PI(I,J+2)+PI(I,J+1))*(P(I,J+2)-P(I,J+1))-YMUE(J)*(
     2    PI(I,J+1)+PI(I,J))*(P(I,J+1)-P(I,J)))
305       CONTINUE
          DO 303 J=2,NZM1
          JJ=J-1+NZM1
          K=J+1
          KK=JJ+NZM1
          XMAT(JJ,J)=-.5*YMUE(J)*(P(I,K)+PI(I,K)-PH(I,J))
          XMAT(JJ+1,J)=EPDT/T(I,K)-.5*(YMUE(K)*(PH(I,K+1)-PI(I,K)-P(I,K))
     1    -YMUE(J)*(PI(I,K)+P(I,K)-PH(I,J)))
          XMAT(JJ+1,J-1)=-.5*YMUE(J)*(P(I,J)+PI(I,J)-PH(I,K))
          XMAT(JJ,JJ+1)=-.5*YMUE(J)*(PI(I,K)+PI(I,J))
          XMAT(JJ+1,JJ+1)=.5*(YMUE(K)*(PI(I,K+1)+PI(I,K))+YMUE(J)*(
     1    PI(I,K)+PI(I,J)))
          XMAT(JJ+1,JJ)=XMAT(JJ,JJ+1)
          XMAT(KK,J)=-.5*YMUE(J)*(PH(I,K)+PH(I,J))
          XMAT(KK+1,J)=.5*(YMUE(K)*(PH(I,K+1)+PH(I,K))+YMUE(J)*(PH(I,K)+
     1    PH(I,J)))
          XMAT(KK+1,J-1)=XMAT(KK,J)
          XMAT(KK,JJ+1)=-.5*YMUE(J)*(PH(I,K)+P(I,K)-PI(I,J))
          XMAT(KK+1,JJ+1)=EPDT/T(I,K)-.5*(YMUE(K)*(PI(I,K+1)-P(I,K)-PH(I,
     1    K))-YMUE(J)*(PH(I,K)+P(I,K)-PI(I,J)))
          XMAT(KK+1,JJ)=.5*YMUE(J)*(PI(I,K)-P(I,J)-PH(I,J))
303       CONTINUE
```

152

```
      XMAT(NZONES,1)=EPDT/T(I,2)+.5*YMUE(2)*(P(I,2)+PI(I,2)-PH(I,3))+
    1 YMUE(1)*PI(I,1)
      XMAT(NZONES,NZONES)=.5*YMUE(2)*(PI(I,3)+PI(I,2))-YMUE(1)*
    1 PI(I,1)
      XMAT(NZM2+1,1)=.5*YMUE(2)*(PH(I,3)+PH(I,2))+YMUE(1)*PH(I,1)
      XMAT(NZM2+1,NZONES)=EPDT/T(I,2)-.5*YMUE(2)*(PI(I,3)-P(I,2)-
    1 PH(I,2))-YMUE(1)*PH(I,1))
      BX(NZONES)=-EPDT*(PI(I,2)/T(I,2)-PI(I-1,2)/T(I-1,2))+.5*
    1 YMUE(2)*(PI(I,3)+PI(I,2))*(P(I,3)-P(I,2))-YMUE(1)*PI(I,1)*(
    2 P(I,2)-P(I,1))
      BX(NZM2+1)=-EPDT*(PH(I,2)/T(I,2)-PH(I-1,2)/T(I-1,2))-CAY1(2)-
    1 CAY2(2)*PSI(I,2)+.5*YMUE(2)*(PH(I,3)+PH(I,2))*(P(I,3)-P(I,2))-
    2 YMUE(1)*PH(I,1)*(P(I,2)-P(I,1)))
      DO 304 J=1,NHZM1
      DO 304 K=1,NHZM1
  304 XMATA(J,K)=XMAT(J,K)
      CALL MATINV(XMATA,NHZM1,BX)
      CONE=0.
      DO 307 J=1,NZM1
      JJ=J+NZM1
      PI(I,J+1)=PI(I,J+1)+BX(J)
      PH(I,J+1)=PH(I,J+1)+BX(JJ)
      KK=JJ+NZM1
      PSI(I,J+1)=PSI(I,J+1)+BX(KK)
      CONE=CONE+ABS (BX(J)/PI(I,J+1))+ABS (BX(JJ)/PH(I,J+1))+ABS (
    1 BX(KK)/PSI(I,J+1))
      IF(PI(I,J+1).LT.0.) PI(I,J+1)=PI(I,1)
      P(I,J+1)=PH(I,J+1)+PI(I,J+1)
  307 CONTINUE
      PH(I,NZT1)=PH(I,NZONES)
      PI(I,NZT1)=PI(I,NZONES)
      P(I,NZT1)= P(I,NZONES)
      NCUT=NCUT+1
      IF(NCUT-10)308,308,62
  308 IF(CONE-1.E-5)62,62,60
   62 CONTINUE
      PSI(I,1)=0.
      DO 65 M=2,NZONES
      P(I,M)=PH(I,M)+PI(I,M)
      DCBAR(M)= (CAY1(M)+CAY2(M)*PSI(I,M))/DCCON
      ABSORD=ABSORD+DCBAR(M)
   65 CONTINUE
      VABS=0.
      DO 39 J=1,NZONES
      V(J)=- (P(I,J+1) -P(I,J))*V(J)*DELX
      VABS=AMAX1(VABS,V(J))
   39 CONTINUE
      VIN=V(1)
      LITER=LITER+1
   26 FLIN=PH(I,1)*V(1  )/(ROMH*T(I,1))
      ABSORD=ABSORD*ASCON
    9 CNVR=0.
      ISUR=1
      IF(INPT) 125,125,126
  126 CONTINUE
      WRITE           (6,123)
  123 FORMAT(1H0,8X,1HV,13X,3HPSI,13X,5HDCBAR)
      WRITE           (6,124)(V(J),PSI(I,J),DCBAR(J),J=1,NZONES)
  124 FORMAT(1H 3E15.7)
  125 CONTINUE
      DO 10 M=2,NZONES
      C(I,M)=C(I-1,M)+DCBAR( M)*DELTAT
```

153

```
           DHN=HCON*(-31.2982+C(I,M)*(23.5742-C(I,M)*6.028))
           CALL PROP(T(I,M),PH(I,M),PI(I,M),XMUM,XKBED,ISUR,IVIS)
           IF(XKBED.LE.0.) GO TO 22
           IF(M.EQ.NZONES) GO TO 15
  11       XLN=(XKL*(T(I,M)-TAMB)-XKBED*AREY*(T(I,M+1)+T(I,M-1)-2.*T(I,M)))
           XLN=XLN/AREX
           GO TO 13
  15       MI=M-1
  16       XLN=(XKL*(T(I,M)-TAMB)-XKBED*AREY*(T(I,MI)-T(I,M)))/AREX
  13       DTHETA=-DHN*DCBAR(  M)*CLASS+(ESSN(M)-XLN)*CLESS
           V(M)  =T(I-1,M)+DELTAT*DTHETA
           XSV=ABS (1.-ABS (T(I,M) /V(  M)))
           IF(INPT.EQ.0) GO TO 18
           WRITE(6,131) DHN,XLN,DTHETA,XKBED
 131       FORMAT(5H DHN=E15.7,2X,4HXLN=E15.7,2X,7HDTHETA=E15.7,
      1    2X,6HXKBED=E15.7)
  18       CNVR=XSV+CNVR
  10       CONTINUE
           IF(INPT) 120,120,121
 121       WRITE             (6,122)FLIN,ABSORD,LITER,NCUT,CONE,CNVR
 122       FORMAT(6HORHOV=E15.7,2X,9HDCBARSUM=E15.7,2X,6HLITER=I2,2X,
      1    5HNCUT=I2,2X,5HCONE=E15.7,2X,5HCNVR=E15.7)
 120       CONTINUE
           DO 2 M=2,NZONES
   2       T(I,M)=V(M)
           T(I,1)=T(I,2)
           C(I,1)=C(I,2)
           IF(LITER-30) 33,33,19
  33       IF(CNVR-1.E-5) 19,19,20
  19       CONTINUE
           DO 55 M=2,NZONES
  55       DAFT(INOW,M)=(PSI(I,M)-PSI(I-1,M))/(XLAM(INOW,M)-XLAM(JCAP,M))
           CSTAR=CSTAR+ABSORD*DELTAT
           WRITE             (6,117)TIME,CSTAR
 117       FORMAT(6HOTIME=F7.3,2X,6HCSTAR=E15.7)
           WRITE             (6,118)
 118       FORMAT(1H07X,2HPH,14X,2HPI,15X,1HP,12X,5HTHETA,12X,4HCBAR)
           WRITE             (6,119)(PH(I,J),PI(I,J),P(I,J),T(I,J),C(I,J),
      1    J=1,NZONES)
 119       FORMAT(1H 5E16.8)
           IF((VABS.EQ.0.).OR.(EPDX.EQ.0.)) GO TO 31
           DINT=EPDX/VABS
  34       IF(DINT.GT.DELTAT) GO TO 32
          IF ((.5*DELTAT).LT.DMIN) GO TO 3.
           DELTAT=.5*DELTAT
           GO TO 34
  32       IF(DELTAT.GE.DMAX) GO TO 31
           IF(2.*DELTAT.GT.DMAX) GO TO 31
           IF(2.*DELTAT.GE.DINT) GO TO 31
           DELTAT=2.*DELTAT
  31       CONTINUE
           TIME=TIME+DELTAT
           INOW=INOW+1
C    SET EVERYTHING BACK
           DO1305 M=1,NZONES
           C(1,M)=C(2,M)
           T(1,M)=T(2,M)
           P(1,M)=P(2,M)
           PH(1,M)=PH(2,M)
           PI(1,M)=PI(2,M)
           PSI(1,M)=PSI(2,M)
 1305      CONTINUE
```

154

```
          IF(INOW.LE.101) GO TO 25
          INOW=52
          DO 27 J=1,51
          JJ=J+50
          DO 27 K=1,NZONES
          XLAM(J,K)=XLAM(JJ,K)
   27     DAFT(J,K)=DAFT(JJ,K)
   25     IF(TIME-TMAX) 23,23,22
  100     FORMAT(6E12.5)
  101     FORMAT(1415)
          END
$      FORTRAN STAB,DECK,LSTIN
$       INCODE   IBMF
CCOMAT
C     MATRIX INVERSION WITH ACCOMPANYING SOLUTION OF LINEAR EQUATIONS
C
          SUBROUTINE MATINV(A,N,B)
C
       DIMENSION IPIVOT(30),A(30,30),B(30)
          EQUIVALENCE (AMAX,PIVOT)
C
C       INITIALIZATION
C
   15 DO 20 J=1,N
   20 IPIVOT(J)=0
   30 DO 550 I=1,N
C
C       SEARCH FOR PIVOT ELEMENT
C
   40 AMAX=0.0
   45 DO 105 J=1,N
   50 IF (IPIVOT(J)-1) 60, 105, 60
   60 DO 100 K=1,N
   70 IF (IPIVOT(K)-1) 80, 100, 740
   80 IF (ABS (AMAX)-ABS (A(J,K))) 85, 100, 100
   85 IROW=J
   90 ICOLUM=K
   95 AMAX=A(J,K)
  100 CONTINUE
  105 CONTINUE
          IPIVOT(ICOLUM)=1
C
C       INTERCHANGE ROWS TO PUT PIVOT ELEMENT ON DIAGONAL
C
  130 IF (IROW-ICOLUM) 140, 310, 140
  140    DO 200 L=1,N
  160 SWAP=A(IROW,L)
  170 A(IROW,L)=A(ICOLUM,L)
  200 A(ICOLUM,L)=SWAP
          SWAP=B(IROW)
           B(IROW)=B(ICOLUM)
          B(ICOLUM )=SWAP
C
C       DIVIDE PIVOT ROW BY PIVOT ELEMENT
C
  310 DO 350 L=1,N
  350    A(ICOLUM,L)=A(ICOLUM,L)/PIVOT

          B(ICOLUM )=B(ICOLUM )/PIVOT

C
C       REDUCE NON-PIVOT ROWS
C
```

155

```
      380 DO 550 LI=1.N
      390 IF(L1-ICOLUM) 400. 550. 400
      400 T=A(L1.ICOLUM)
          IF(T.EQ.0.) GO TO 550
      430 DO 450 L=1.N
      450 A(L1.L)=A(L1.L)-A(ICOLUM.L)*T
          B(L1)=B(L1)-B(ICOLUM )*T
      550 CONTINUE
      740 RETURN
          END
   $      FORTRAN STAB.DECK.LSTIN
   $      INCODE  IBMF
CPROP
          SUBROUTINE PROP(TEMP.PPH.PPI.XMUM.XKBED.ISW.IVIS)
C SUBROUTINE PROPCA CALCULATES VISCOSITY AND THERMAL CONDUCTIVITY
C   THE INITIALIZATION VALUES NEEDED ARE (1) MOLECULAR WEIGHTS
C  (2) COLLISION DIAMETERS AND (3) K/EPSILON TO CALCULATE OMEGA
          COMMON SIG.EPSK.XM.DEN1.DEN2.C2.CON.SRAT .EPS
          DIMENSION SIG(2).EPSK(2).XM(2).PHI(4).CON(2).ZZ(16).     VAR(2)
          DIMENSION OMEG(2).XMU(2).XX(2).XK(2)
          DATA EXPN.C1.PHI(1).PHI(4).(ZZ(I).I=1.16)/.33333333.2.48375.
      1   1..1..473..2.38E6.573..2.3E6.673..2.15E6.773..2.01E6.873..
      2   1.8E6.973..1.51E6.1073..1.13E6.1173..6.59E5/
      3   P=PPH+PPI
          SQT=SQRT (TEMP)
          DO 4 I=1.2
      4   VAR(I)=TEMP/EPSK(I)
          OMEG(1)=5.015/(ALOG(VAR(1))+3.772)
          IF(VAR(2)-3.4)5.5.6
      5   OMEG(2)=3.36/(ALOG(VAR(2))+2.125)
          GO TO 7
      6   OMEG(2)=5.015/(ALOG(VAR(2))+3.772)
      7   DO 8 I=1.2
      8   XMU(I)=CON(I)*SQT/OMEG(I)
          XMXM=XMU(1)/XMU(2)
          SQT=SQRT (XMXM*SRAT)
          PHI(2)=(1.+SQT)**2/DEN2
          PHI(3)=(1.+1./SQT)**2/DEN1
          XK(1)=((6.62+.00081*TEMP+C1)*XMU(1)/XM(1))*4.184E7
          XK(2)= C2*XMU(2)
      14  CONTINUE
          XKM=0.
          XMUM=0.
          XX(1)=PPH/P
          XX(2)=PPI/P
          DO 9 I=1.2
          YN=XX(I)/(XX(I)*PHI(2*I-1)+XX(2)*PHI(2*I))
          XMUM=XMUM+YN*XMU(I)
      9   XKM=XKM+YN*XK(I)
          IF(ISW.EQ.0) RETURN
          K=(TEMP-473.)*1.E-2+1.
          IF(K.GE.8) K=7
          IF(K.LT.1) K=1
C     BETWEEN KK AND KK+2
          KK=2*K-1
          XKSOL=ZZ(KK+1)+(TEMP-ZZ(KK))*(ZZ(KK+3)-ZZ(KK+1))*1.E-2
          RT=EPS*(XKSOL-XKM)/XKM**EXPN
          XKBED=EPS*(XKM-XKSOL)+XKSOL
      10  XM3=XKBED**EXPN
          F=(XKSOL-XKBED)/XM3-RT
          FP=-(XKSOL+2.*XKBED)/(3.*XM3*XKBED)
          DEL=-F/FP
                              156
```

```fortran
          XKBED=XKBED+DEL
          IF(XKBED)11,11,12
   11     WRITE              (6,100)
  100     FORMAT(50H       BED CONDUCTIVITY CALCULATED ZERO OR NEGATIVE )
          WRITE              (6,101)XKBED,RT,XKSOL,XKM,F,FP,DEL
  101     FORMAT(1P7E12.4)
          RETURN
   12     IF(ABS (DEL/XKBED)-1.E-5)13,13,10
   13     RETURN
          END
$     FORTRAN STAB,DECK,LSTIN
$         INCODE  IBMF
CSERV
          SUBROUTINE SERVAL     (ALPS,ANS)
C THIS SUBROUTINE EVALUATES THE SUM FROM 1 TO INFINITY OF THE SERIES
C   EXP(-ALPS*N**2)/N**2
          DIMENSION XJ(4)
          DATA PIE/3.1415927/
          DATA XLS,XJ/25.,1.,4.,9.,16./
          IF(ALPS.GT.0.) GO TO 1
          ANS=PIE**2/6.
          RETURN
    1     ALLS=ALPS*XLS
          EXS=.5*EXP(-ALLS)
          ANS=   EXS/XLS
          DO 3 J=1,4
    3     ANS=ANS+EXP (-ALPS *XJ(J))/XJ(J)
C    GAUSS CALCULATES THE INTEGRAL PART OF THE SUM APROXIMATION
    4     CALL GAUSS(PSUM,ALLS)
          ANS=ANS+   SQRT (ALPS)*EXS*PSUM
          RETURN
          END
$     FORTRAN STAB,DECK,LSTIN
$         INCODE  IBMF
CGAUSS
          SUBROUTINE GAUSS(PSUM,ALLS)
          DIMENSION A(7),X(7)
          DATA A,X/.40931895,.42183128,.14712635,.20633514E-1,
     1    .10740101E-2,.15865464E-4,.31703155E-7,.19304368,1.0266649,
     2    2.5678767,4.9003531,8.1821534,12.73418,19.395728/
          PSUM=0.
          DO 1 J=1,7
          Y=X(J)+ALLS
          F=Y*SQRT (Y)
    1     PSUM=PSUM+A(J)/F
          RETURN
          END
$     FORTRAN STAB,DECK,LSTIN
$         INCODE  IBMF
CFAZEDA
          SUBROUTINE FAZEDA(DYNES,THETA,C)
          DIMENSION A(3),B(3),D(4)
          DATA A,B,D(4),THC3/-3.8415,38.6433,-34.2639,-31298.2,23574.1,
     1    -6028.,9.2821,27.8463/
          PRESH=DYNES
          C=1.75
          XLEFT   = ALOG(PRESH) /2.302585
          DO 1 J=1,3
    1     D(J)=A(J)+B(J)/THETA
          TC2=2.*D(3)
    3     F=XLEFT-(D(1)+C*(D(2)+C*(D(3)+C*D(4))))
          FP=-(D(2)+C9(TC2+C*THC3))
```

157

```
      DELC=-F/FP
      C=C+DELC
      IF(ABS (DELC/C)-1.E-6)998,998,3
998   EQUIL  =9.9656 -  11494.3 / THETA
      IF (XLEFT - EQUIL) 997,997,996
997   WRITE            (6,1011)PRESH,THETA
1011  FORMAT(29H0   OUTSIDE DELTA REGION, P=  0PF10.4,14H ATM.     T =
     1           0PF10.3, 8H KELVIN  )
996   RETURN
      END
```

REFERENCES

1. Parker, W. J. and Jenkins, R. J., "Thermal Conductivity Measurements of Bismuth Telluride in the Presence of a 2 Mev Electron Beam." Advanced Energy Conversion, Volume 2, pp 87-103, January/June 1962.

2. Iacobelli, R. and Moretti, S., "Thermal Diffusivity and Conductivity Measurements on Metals and Oxides at High Temperatures." Rev. Hautes Temper. et Refract., t 3, pp 215-228, 1966.

3. Lustman, B. and Kerze, F., Jr., The Metallurgy of Zirconium, McGraw-Hill Book Company, Inc., 1955.

4. Rohsenow, W. M. and Choi, H., Heat, Mass and Momentum Transfer, Prentice-Hall, Inc., 1961.

5. McAdams, W., Heat Transmission, McGraw-Hill Book Company, Inc., 1964.

6. Goldsmith, A., Waterman, T. and Hirschhorn, H., "Thermophysical Properties of Solid Materials." Volume I, WADC-TR-58-476, Armour Research Foundation, August 1960.

7. Ambrose, C., et al., "Thermophysical Properties of Zirconium-Uranium Hydride." Fourth Conference on Thermal Conductivity, U. S. Naval Radiological Defense Laboratory, San Francisco, California, 1964.

8. Ofte and Wittenberg, "Transactions of Metallurgical Society." AIME 227, 706-11, 1963.

9. Buddle, J., Fischer, K., Wenz, W. and Sauerwald, F., Z. Physik Chem. 218, 100-107, 1961.

10. Rothwell, E. J. Inst. Metals 90, 389-94, 1961-62.

.1. Kaaschow, Ind. Eng. Chem., Anal. Ed. 10, 35, 1938.

12. "Feasibility Study of Terrestrial Thermoelectric Nuclear Power Plant," AFWL-TR-66-16, Martin Marietta, June 1966.

13. Evans, Robley, D., Ph.D. The Atomic Nucleus, McGraw-Hill Book Co., Inc., 1955.

14. Frost, A. and Pearson, R., Kinetics and Mechanism, John Wiley & Son, 1961.

DOCUMENT CONTROL DATA · R & D

(Security classification of title, body of abstract and indexing annotation must be entered when the overall report is classified)

1. ORIGINATING ACTIVITY (Corporate author)	2a. REPORT SECURITY CLASSIFICATION
Martin Marietta Corporation, Nuclear Division Middle River, Maryland 21220	UNCLASSIFIED
	2b. GROUP

3. REPORT TITLE

FEASIBILITY STUDY OF CONTROL MECHANISM AND COOLANT PROPERTIES OF A TERRESTRIAL UNATTENDED REACTOR POWER SYSTEM

4. DESCRIPTIVE NOTES *(Type of report and inclusive dates)*

9 March 1966-30 September 1967

5. AUTHOR(S) *(First name, middle initial, last name)*

R. Magladry; G. F. Zindler

6. REPORT DATE	7a. TOTAL NO. OF PAGES	7b. NO. OF REFS
July 1968	174	14

8a. CONTRACT OR GRANT NO. AF 29(601)-7180	9a. ORIGINATOR'S REPORT NUMBER(S)
b. PROJECT NO. 2800 and 3145	AFWL-TR-67-114, Vol I
c. Task No. 02 and 024	9b. OTHER REPORT NO(S) (Any other numbers that may be assigned this report)
d.	

10. DISTRIBUTION STATEMENT This document is subject to special export controls and each transmittal to foreign governments or foreign nationals may be made only with prior approval of AFWL (WLDC), Kirtland AFB, NM 87117. Distribution is limited because of the technoloby discussed in the report.

11. SUPPLEMENTARY NOTES	12. SPONSORING MILITARY ACTIVITY
	AFWL (WLDC) Kirtland AFB, NM 87117

13. ABSTRACT

(Distribution Limitation Statement No. 2)

A detailed program of analytical and experimental investigation into the technical feasibility of the H-Rho nuclear reactor control system and tetraphosphorous trisulfide (P_4S_3) as a reactor coolant are presented in this study. The H-Rho control system investigation includes determinations of hydrogen transport (permeability) through porous bodies of zirconium hydride and uranium zirconium hydride as well as the absorption-desorption of hydrogen within the hydride bodies. The effects of temperature, pressure, particle size, inert gas and irradiation are evaluated. The investigation of the coolant includes determinations of viscosity, surface tension, thermal conductivity, vapor pressure, liquid density and heat of fusion. The effects of irradiation on the P_4S_3 are evaluated. The results of the investigation demonstrate that both the H-Rho control system and the P_4S_3 coolant are particularly suited for application to the Terrestrial Unattended Reactor Power System (TURPS).

14 KEY WORDS	LINK A		LINK B		LINK C	
	ROLE	WT	ROLE	WT	ROLE	WT
Terrestrial Unattended Reactor Power System (TURPS)						
Hydrogen-transport reactivity control system						
Tetraphosphorous trisulfide, P_4S_3 (Theon)						
Zirconium hydride						
Uranium zirconium hydride						